Volume 2
September 2019

ISSN: 2617-4944

Timorese Academic Journal of Science and Technology (TAJST)

Published by:
Faculty of Engineering, Science and Technology
Universidade Nacional Timor Lorosa'e
(FEST-UNTL)

Timorese Academic Journal of Science and Technology (TAJST)
Volume 2
September 2019

Redaction Address
Cooperation Unit – FEST-UNTL, Avenida Hera, Cristo-Rei, Dili, Timor-Leste

Edition
Cooperation Unit – FEST-UNTL

Supporter
JICA-CADEFEST Project Phase-II

Printing: Typography Duta Xerox

ISSN: 2617-4944

Timorese Academic Journal of Science and Technology (TAJST)

Volume 2

September 2019

Editorial Board

Technical Assistant

Message from the Chief Editor

Dear Readers,

It is my pleasure to publish the Volume 2 of the TAJST. All manuscripts published in this volume are presented in English, which should be a positive shifting of our policy.

This volume composes of 17 papers which includes one invited paper and 16 regular papers from various fields in engineering and science, involving renewable energy and environmental science, energy conversion, material science, road infrastructure, computer science, and electrical circuit & system.

As the chief of editorial board, I would like to thank all authors for their great contribution to publish Volume 2. I would like to express my great appreciation to our reviewers for their professional comments that contribute to enhance technical quality. I would also like to thank the editorial board members and technical assistants for their fruitful discussion and assistance during preparation of the present volume. Finally, we should thank JICA-CADEFEST Project for the financial support.

On behalf of the editorial board, I would welcome any technical idea, suggestion and/or comments for improving the quality of TAJST in a future publication.

Cancio Monteiro, Dr.Eng.
Chief Editor

Timorese Academic Journal of Science and Technology (TAJST)
Volume 2
September 2019

Contents

What are Transparent Conducting Oxides? -Study on Electron Spin Resonance-

Mitsuo Yamaga

Department of Electrical, Electronic and Computer Engineering, Gifu University, Gifu 501-1193, Japan

E-Mail: yamaga@gifu-u.ac.jp

Abstract: Transparent conducting oxides (TCOs) have high transparency in the visible range and high electrical conductivity. Both properties are performed by free carrier densities of ~10^{19} cm^{-3} in TCOs, being three orders of magnitude smaller than those in metals. Insulator-to-metal transition in semiconductors has been discussed using the variable-range hopping model. Hopping process of free carriers in pure and Si-doped β-Ga_2O_3 single crystals is derived from the temperature dependence of the electron-spin resonance (ESR) line ascribed to the conduction electrons.

Keywords: transparent conducting oxides, gallium oxide, electron spin resonance

1. Introduction

Transparent conducing oxide (TCO) materials have been developed rapidly in variety of materials, physical/chemical properties and sample preparations (sputtering, spray pyrolysis, chemical vapor deposition, and pulsed laser deposition) since 1995 [1]. In the advanced information society, TCO devices have been applied to portable electronics, flat and flexible displays, electrochromic windows, thin-film photovoltaics, transparent transistors, and et al. [1]. The above devices include semiconductors, molecular and polymer organics, glass, metal and plastic.

Metal oxides are classified into three distinct groups as (i) MO, (ii) M_2O_3 and (iii) MO_2 (M: metal element). ZnO and MgO of the group (i) have hexagonal and rock salt structures, respectively. Al_2O_3, Ga_2O_3 and In_2O_3 of the group (ii) have corundum, monoclinic and bixbyite structures, respectively. SiO_2(α-quartz), TiO_2(rutile), and SnO_2 of the group (iii) have rhombohedral, tetragonal and tetragonal structures, respectively. The crystal structure provides a guideline for searching novel TCOs [1].

Ionic crystals of MgO, Al_2O_3 and SiO_2 are insulators. Oxygen vacancies as point defects are created in these crystals under particular crystal growth conditions (for instance the reduced atmosphere) or by radiation [2]. Electrons trapped at oxygen vacancies are called color centers. Electrons are confined in nano-sized square-well potential and cannot escape from the deep well. Namely, electrons cannot be freely moved in the crystal [2], [3].

ZnO, Ga_2O_3 and In_2O_3 materials are changed from insulators to semiconductors through impurity-doping or preprocessing/ postprocessing for their crystal preparations. A

typical commercial TCO is the Indium Tin oxide (ITO) in which Sn impurities are added in the form of SnO_2 (~10 weight %) [1]. The transparency is ~80% in the visible range from 400 to 700 nm. The short wavelength cut off below 300 nm is due to the bandgap excitation of In_2O_3. The gradual decrease of the transmission above ~1000 nm, namely, the corresponding increase of the reflection above 1500 nm are due to collective oscillations of conduction electrons called plasma oscillations [2]. There can be substantial absorption due to the plasma oscillations. The maximum absorption occurs at the plasma wavelength, λ_p, calculated using the free carrier density. A free carrier density of $\sim 10^{22}$ cm^{-3} in a metal corresponds to a plasma wavelength (λ_p~330 nm) in the ultraviolet (UV) region [2]. The plasma wavelength for the ITO with the carrier density of $\sim 10^{19}$ ($1/cm^3$) is calculated to be λ_p~10 μm.

We have studied β-Ga_2O_3 crystals as one of TCOs. As β-Ga_2O_3 crystals exhibit a band gap of E_g=4.8 eV, the transparency extends from the visible into the UV regions [4]. The electrical conductivity exhibits a semiconductor behavior even at low temperatures [5], [6]. The band-to-band excitation (E>4.8 eV) produces intrinsic UV/blue broadband fluorescence and blue/green broadband phosphorescence associated with point defects [7]. Electronic structure of the free carriers and its electrical transport process have been examined by the electron-spin resonance (ESR) technique [8].

In this paper, we report the ESR analyses involved with the electrical conductivity in the β-Ga_2O_3 crystals, and discuss how shallowly trapped electrons contribute to the electrical conductivity.

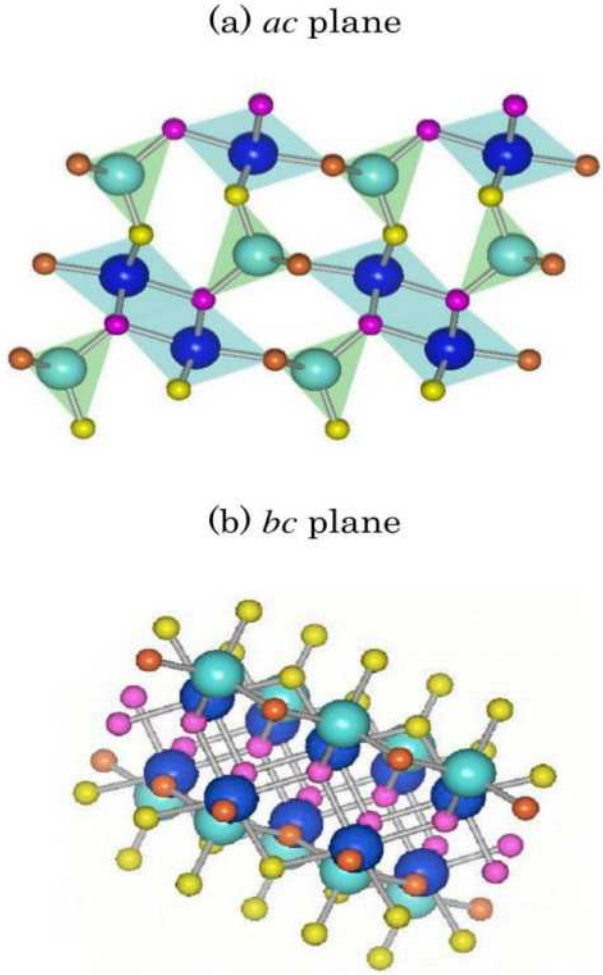

Fig. 1 Projection of a unit cell of $\beta - Ga_2O_3$ to (a) the *ac* plane and (b) the *bc* plane.

2. Crystal Structure and Experimental Procedure

β-Ga_2O_3 has a monoclinic structure with the space group $C2/m$ [9]. The lattice parameters at room temperature are a=1.223 nm, b=0.304 nm, and c=0.5807 nm and the unique axis β=103.7° [8]. Ga ions are surrounded by O ions in either a tetrahedral or an octahedral coordination. A separated chain structure of the two Ga sites is formed along the b-axis as shown in Fig. 1 [7], [8].

Single crystals of β-Ga_2O_3 were grown from starting powders of 4N and 6N Ga_2O_3 by the floating zone technique [4]-[8]. β-Ga_2O_3 single crystals doped with Si were also grown. Si doping concentrations were ~10^{19} cm^{-3} [6].

Samples were prepared by cleaving along the (100) and (001) planes, with approximate dimensions of $10\times10\times0.5$ mm^3 for optical and electrical measurements, and $2\times0.4\times0.2$ mm^3 for ESR measurements.

ESR measurements were carried out using a Bruker EMX10/12 X-band spectrometer with ~9.69 GHz in the temperature range of 5-300 K and a Bruker Biospin EMXmicro X-band spectrometer with ~9.55 GHz in a range of 110-500 K.

3. Experimental Results

3.1 Optical Spectra

Figure 2 shows the optical absorption spectra at 300 K in the wavelength range between 200 and 2500 nm for the β-Ga_2O_3 (4N), (6N) and β-Ga_2O_3:Si samples. The band edges are observed approximately at 275 nm for these samples [4], [7], [8]. The absorption coefficients for the 4N pure and Si-doped samples gradually increase in the infrared (IR) region from 1000 to 2500 nm. On the other hand, the optical absorption spectrum for the 6N pure sample is flat and negligibly small in the range between 300 and 2500 nm. The lack of plasma absorption in this range for the Ga_2O_3 (6N) sample may be due to a further shift of the plasma wavelength into the far IR, which is linked to the further decrease in the carrier density.

3.2 Electrical Conductivity

Electrical conductivity of the β-Ga_2O_3 single crystals is in the range from 0.02 to 50 (Ω^{-1}cm^{-1}) [5]. Carrier densities as donors are estimated to be ~ 10^{18} cm^{-3} from the Hall measurement with the Van der Pauw configuration [5]. On the other hand, the conductivity of the β-Ga_2O_3: Si sample can be intentionally controlled over three orders of magnitude by Si doping [6].

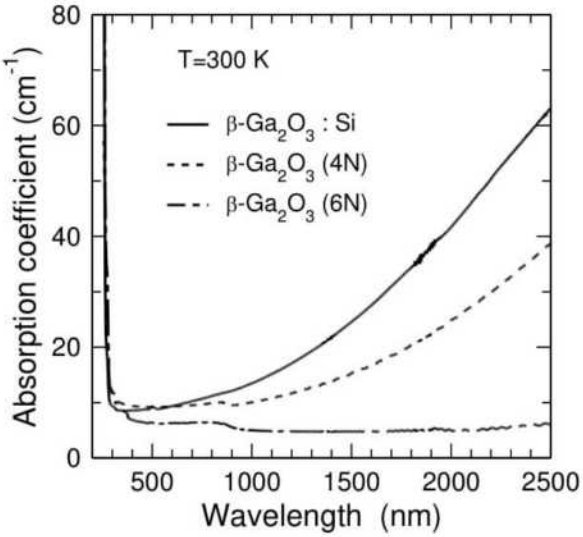

Fig. 2 Absorption spectra for various β-Ga_2O_3 crystals observed at 300 K.

The related free-carrier concentrations, varying between 10^{16} and 10^{18} cm^{-3}, correspond to a 25%–50% effective Si donors and the remains are trapped electrons [6].

3.3 ESR

ESR measurements can give information on free carriers in β-Ga_2O_3. Small anisotropic g values of an unpaired electron-spin of the free carriers observed for the β-Ga_2O_3 (4N) and β-Ga_2O_3:Si samples are g_x=1.958, g_y=1.960 and g_z=1.962, where the z axis is parallel to the b axis and the x and y axes are in the ac plane [8]. They are independent of temperature below 300 K [8]. The ESR results indicate that the free carriers in the β-Ga_2O_3 (4N) and β-Ga_2O_3:Si samples are not moved in any direction but moved along the chain parallel to the b axis [7, 8]. On the other hand, the ESR signal for the β-Ga_2O_3 (6N) sample is two orders of magnitude weaker than those for the β-Ga_2O_3 (4N) and β-Ga_2O_3:Si samples. The result is consistent with that for the β-Ga_2O_3 (4N) sample annealed in the oxygen atmosphere at 900℃ [4]. The decrease of the ESR signals corresponds to the decrease of free carrier densities related to oxygen

vacancies, namely, the disappearance of the absorption and reflection in the near-IR region in Fig. 2.

Figure 3 shows the temperature dependence of (a) the ESR spectra and (b) the ESR line widths, defined as peak-to-peak magnetic field separation, from 5 to 300 K for the β-Ga_2O_3 (4N) sample. As temperatures increase from 5 to 297 K, the magnetic resonance field is shifted to lower field because of lower cavity-resonant microwave frequency. The ESR spectrum at low temperatures ($T \leq 20$ K) has a broad Gaussian shape as shown in Fig. 3(a). However, the spectrum is changed to a Lorentzian shape above 40 K. The line width is gradually decrease in increasing from 5 to 200 K and has a minimum at ~250 K as shown in Fig. 3(b). The minimum value (~1.7×10^{-2} mT) is two orders of magnitude smaller than that (~2.3 mT) at 5 K.

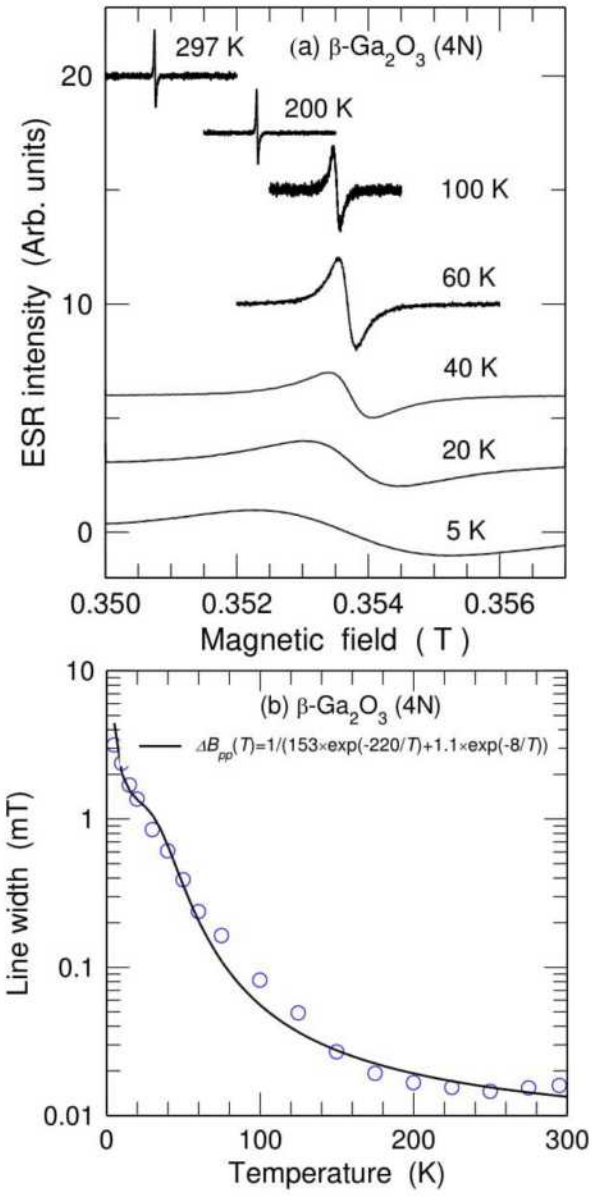

Fig. 3 Temperature dependence of (a) the ESR spectra and (b) the ESR line width for $\beta-Ga_2O_3$(4N).

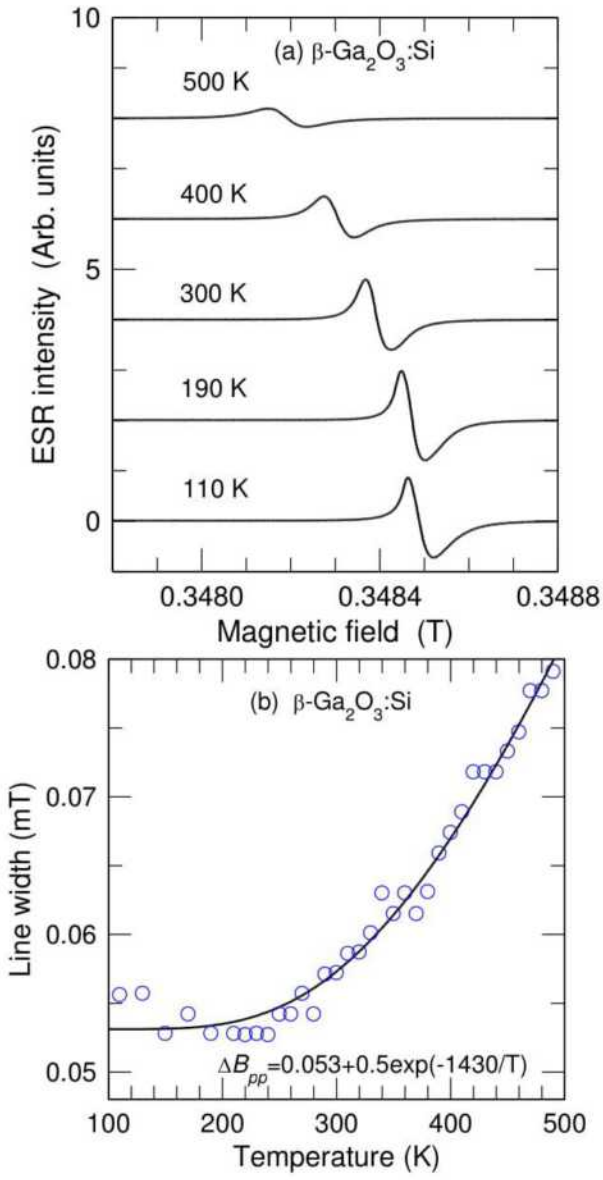

Fig. 4 Temperature dependence of (a) the ESR spectra and (b) the ESR line width for $\beta-Ga_2O_3$:Si.

This phenomenon, called '*motional narrowing*' of ESR spectra, expects that as temperatures increase from 5 to 200 K, electrons are moved through hopping between electron-trapped centers or as conduction electrons in a narrow impurity-like band of the crystals.

Figure 4 shows temperature dependence of (a) the ESR spectra and (b) the ESR line widths from 110 to 500 K for the β-Ga_2O_3:Si sample. The ESR spectrum in Fig. 4(a) is gradually decreased in intensity as the temperature increases up to 500 K. The line widths in Fig. 4(b) are increased beyond ~250 K. The behavior of the line width at high temperatures (T≥250 K) in Fig. 4(b) is reverse to that at low temperatures (T≤200 K) in Fig. 3(b).

4. Discussion

We discuss the anomalous behavior of the line width of the ESR spectrum ascribed to the free carriers in the β-Ga_2O_3 crystals at low temperatures (T≤ 200K) and high temperatures (T≥ 250 K) [10], [11].

An ESR line shape is, in general, represented by a differential curve of a Lorentzian, $I(B)$, as a function of magnetic field B, and given in the form of [11]

$$I(B) = \frac{1}{\pi}\frac{\Delta B}{(B-B_0)^2+\Delta B^2} \quad (1)$$

where B_o is a magnetic resonance field and $2\Delta B$ is a full width of half maximum. The observed peak-to-peak field separation (ΔB_{pp}) of the differential ESR curve satisfies the relation of $\Delta B_{pp}=2\Delta B/\sqrt{3}$.

4.1 Motional Narrowing in Low Temperature Region

The ESR lines for β-Ga_2O_3 (4N) below 40 K in Fig. 3(a) are represented by a Gaussian. Their line widths are ascribed to the superhyperfine (*shf*) interaction between the electron spin and the nuclear spins (I=3/2) of the surrounding Ga^{3+} ions. Motional narrowing of the ESR line is discussed in the same way as exchange narrowing proposed by Anderson [12]. The narrowing width is represented by

$$\Delta B=\frac{\omega_{shf}^2}{\omega_{mn}} \quad (2)$$

where ω_{shf} is associated with a width produced by the *shf* interaction, and ω_{mn} is related to spin flips of electron after $2\pi/\omega_{mn}$ through motional narrowing. The spin-flip frequency is assumed to be associated with a hopping frequency between donors in semiconductors, and simply represented by the Arrhenius equation. The spin flip frequency is given in the form of,

$$\omega_{mn} = \omega_0 \exp(-\frac{\Delta_{mn}}{kT}) \quad (3)$$

where Δ_{mn} is an activation energy for the spin flip motion.

The solid curve in Fig. 3(b) is calculated using $\Delta B_{pp}=2\Delta B/\sqrt{3}$ and Eqs. (2) and (3). In order to fit the data, two Arrhenius equations with different activation energies (0.7 meV, 19 meV) in the regions of T≤40 K and 40<T≤300 K are required.

4.2 Spin-Lattice Relaxation in High Temperature Region

The line-broadening in Fig. 4(b) can be explained by the spin-lattice relaxation process [10], [11]. There are three processes; (1) direct process, (2) Raman process, and (3) Orbach process [9]. The Orbach process is dominant at high temperatures. The line width is inversely proportional to the longitudinal spin-lattice relaxation time (T_1) and given in the form of [11]

$$\Delta B = \frac{\gamma}{T_1} = a + b \times \exp(-\frac{\Delta_{sl}}{kT}) \qquad (4)$$

where γ is the magnetogyric ratio and Δ_{sl} is an energy level above the ground spin-doublet. The solid curve in Fig. 4(b), calculated using $\Delta B_{pp}=2\Delta B/\sqrt{3}$, Eq. (4) and the parameter of Δ_{sl}=1430 K(=120 meV), fits the experimental data points very well. The activation energy of Δ_{sl}=120 meV may be equal to thermal excitation energy of shallowly trapped electrons into the bottom of the conduction band.

When temperature is below or above ~40 K, the line shape is represented by a Gaussian or a Lorentzian, respectively. Their line shapes correspond to the localized state or thermally delocalized state of the shallowly trapped electrons. The latter leads to the electrical conductivity. As a consequence, the β-Ga_2O_3 (4N) single crystal behaves like a semiconductor.

5. Conclusions

The present results have shown the important role of the intrinsic deficits associated with oxygen vacancies and Si-doping in the host crystal. The oxygen vacancies are formed through evaporation in GaO and O_2 from the molten zone. It is very difficult to control the concentration of the oxygen vacancies through the growth conditions. On the other hand, the electrical conductivity can be intentionally controlled through the Si-doping level. However, Si doping level is not coincident with the donor densities in the crystals. Si-doping creates both shallow and deep trapped electrons. The shallowly trapped electrons in β -Ga_2O_3 contribute to the high conductivity above 150 K.

At last, a good understanding of the formation of these defects centers leads to high electrical conductivity in wide-gap semiconductors for the desired optical and electrical response to special applications.

References

[1] D. Ginley, H. Hosono and D. C. Paine (eds.), "*Handbook of Transparent Conductors*", Springer, New York, 2010.

[2] C. Kittel, "*Introduction to Solid State Physics*", John Wily & Sons, New York, 2004, chaps. 14 and 20.

[3] B. Hederson and G. F. Imbush, "*Optical Spectroscopy of Inorganic Solids*", Clarendon Press, Oxford, 1989, chap.2.

[4] E. G. Villora, M. Yamaga, T. Inoue, S. Yabasi, Y. Masui, T. Sugawara and T. Fukuda, "Optical spectroscopy study on β-Ga_2O_3", Jpn. J. Appl. Phys., vol. **41**, Part 2 , no. 6A, pp. L622-L625, 2002.

[5] E. G. Villora, K. Shimamura, T. Ujiie and K. Aoki," Electrical conductivity and lattice expansion of β -Ga_2O_3 below room temperature", Appl. Phys. Lett., vol. **92**, no. 20, pp. 202118-1-3, 2008.

[6] E. G. Villora, K. Shimamura, Y. Yoshikawa, T. Ujiie and K. Aoki," Electrical conductivity and carrier concentration control in β-Ga_2O_3 by Si doping", Appl. Phys. Lett., vol. **92**, no. 20, pp. 2021120-1-3, 2008.

[7] M. Yamaga, T. Ishikawa, M. Yoshida, T. Hasegawa, E. G. Villora and K. Shimamura, "Polarization of optical spectra in transparent conductive oxide β-Ga_2O_3", Phys. Status Solidi C, vol. **8**, no. 9, pp. 2621-2624, 2011.

[8] M. Yamaga, E. G. Villora, K. Shimamura, N. Ichinose and M. Honda, "Donor structure and electric transport mechanism

in β-Ga_2O_3", Phys. Rev. **B**, vol. **68**, no. 15, pp. 155207-1-9, 2003.

[9] T. Hahn (ed.), "*International Tables for Crystallography*", Kluwer Academic Publishers, Dordrecht, 1996, vol. **A**, p. 158.

[10] G. E. Pake and T. L. Estle, "*The Physical Principles of Electron Paramagnetic Resonance*", W. A. Benjamin, London, 1973, chaps. 2, 5, 6 and 9.

[11] A. Abragam and B. Bleaney, "*Electron Paramagnetic Resonance of Transition Ions*", Clarendon Press, Oxford, 1970, chaps.1, 9 and 10.

[12] P. W. Anderson and P. R. Weiss, "Exchange narrowing in paramagnetic resonance", Rev. Mod. Phys., vol. **25**, no. 1, pp. 269-276, 1953.

Time Series Analysis of Environmental Changes in Dili City, Timor-Leste by using Satellite Images Remote Sensing

Nattha Okajima, Masahiko Sekine and Ariyo KANNO

Graduate School of Sciences and Technology for Innovation, Yamaguchi University, Ube 755-8611, Japan

E-Mail: ms@yamaguchi-u.ac.jp

Abstract: Many past environmental data had been lost or not recorded during the periods of confusion in Timor-Leste. We analyze the anthropogenic influence on coastal water pollution using satellite remote sensing data during the period of 1986 to 2015 in Dili. Population change could be estimated using building and residential area change detected by Landsat data. Although Chlorophyll concentration could not be determined by using satellite data, we found that seaweed cover in the coastal area could be a substitute of Chlorophyll. Our analysis showed that population increase had positive relationship with seaweed cover increase, which means coastal area of Dili had been suffering eutrophication problem caused by increasing population. Appropriate wastewater treatment is required to stop the pollution.

Keywords: Dili, coastal pollution, remote sensing, land use, chlorophyll, seaweed

1. Introduction

Timor-Leste became an independent country on 20 May 2002. In 16th century to 1975, Timor-Leste was occupied by Portugal. After that Timor-Leste was under Indonesia since 1975 to 1999. In 1999 to May 2002, United Nation (UN) was a sponsor for majority of Timorese and voted for independence from Indonesia [1]. Since Timor-Leste was under administration of many countries, there were many conflicts and fighting. The major infrastructures of the country including house, school, water supply, etc. were destroyed. Many environmental data were lost and/or not recorded during these periods of confusion.

Our group conducted water quality surveys in streams and wells in Dili, and found high organic, toxic, and bacterial pollution in their water mainly because of their untreated household wastewater. Although the government and people notice the pollution, there is almost no action for it since they have luckily not experienced epidemics. To motivate a quick action, it would be necessary to show the proof that the stream pollution is causing deterioration in the coastal area, since they are promoting tourism and beautiful sea is the major resource for the country. For this purpose, we have started to measure some water quality items like coliform group, and we have found that the coliform group concentration is not fit the water quality standard for bathing. However, there are many animals in the basin and existence of coliform group is not enough to

show the relationship between the anthropogenic stream pollution and coastal pollution. Although showing the historical change of population and water quality is one possible method to prove it, there is no historical environmental data as we already mentioned.

On the other hand, satellite remote sensing might be able to provide data in the past. We can utilize the data for understanding environmental change [2]. By using remote sensing in shallow water area, the spatial resolution, atmospheric and water column correction area are required [3]. We may be able to find out some proof that pollution in the land area is affecting the coastal water quality.

The purpose of this study is to describe the relationship between water quality and population change in Dili city, Timor-Leste by applying remote sensing and GIS techniques

2. Methods

Figure 1 is the study area. The study area (94.85 km^2) is in Dili capital city, Timor-Leste in Southeast Asia. Dili is a small flat area and is facing specific environmental problem [4]. The total area of Timor-Leste is 14,874 km^2. The country has a quite dramatic topography, dominated by the central mountain range of Ramelau. As much as 44% of East Timor's area may have a slope of more than 40%.

Firstly, population change is estimated based on the land use change. By using supervised classification method, land uses are classified into water, building, residential, farmland, grassland, bare, sediment, sparse forest, moderate forest, and dense forest in 1986, 1990, 1995, 2000, 2005, 2010, 2015. A total of 100 ground truth points is selected from aerial photo of Google Earth for each year based on field observation and interview to local people in 2017.

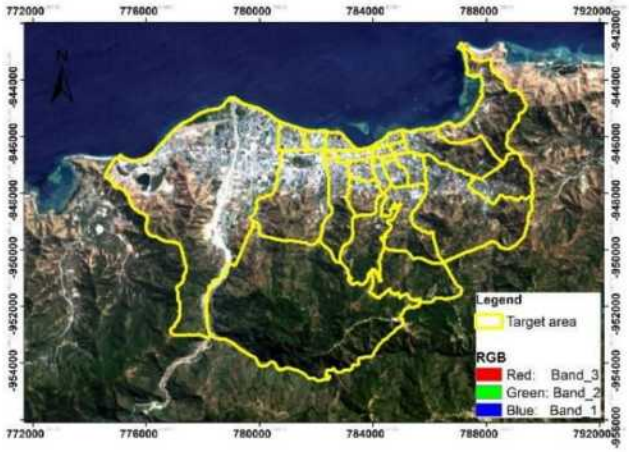

Fig. 1 Study area

Accuracy of the analysis is estimated using Kappa coefficient [5].

Secondly, as a popular water quality index using satellite, we estimate the Chlorophyll concentration (Chl) by applying CI algorithm [6] and OCx algorithm [7]. Chl is a component of phytoplankton and is thought to be an index of nutrient pollution such as nitrogen and/or phosphorus which are included in household wastewater. However, Chl is sometimes difficult to detect in the coastal area because of the disturbance by suspended solids and/or water bottom which are frequently visible in the shallow sea. We also measure coastal Chl concentration by using Chlorophyll - Turbidity recorder COMPACT - CLW (Allec electric).

Thirdly, we estimate seaweed cover in the coastal area as a new water quality index using satellite image. Seaweed is a group of macro plants which glows using nutrients and is easily be seen using aerial photo. It is also expected to be seen in satellite images. Supervised classification was applied for seaweed area and maximum likelihood method is used to draw distribution maps. Since coastal sea image will be affected by tide level, we perform the analysis for all available Landsat images during the target years and choose the maximum area of seaweed in the year by assuming that the

maximum seaweed bed can be observed in the image taken at the shallowest tide level.

Lastly, we discuss about the relationship between population change and water quality change in the Dili coast.

3. Result and Discussion

3.1 Land Use Classification

Figure 2 shows the land use classification results. Overall accuracy and Kappa were 78.0% and 0.7515 for 2015, 75.0% and 0.7515 for 2010, 75.0% and 0.7158 for 2000, 68.0% and 0.6203 for 1990 and 77% and 0.7277 for 1986, the values of which show the results are acceptable. Figure 3 shows the area change of each land use along the year. The area of bare, three types of forests, grassland, and/or farmland fluctuate along the years. This seems to be the drastic color change of vegetations on these land uses during the rainy and dry seasons, and the areas for these land uses are not reliable. On the other

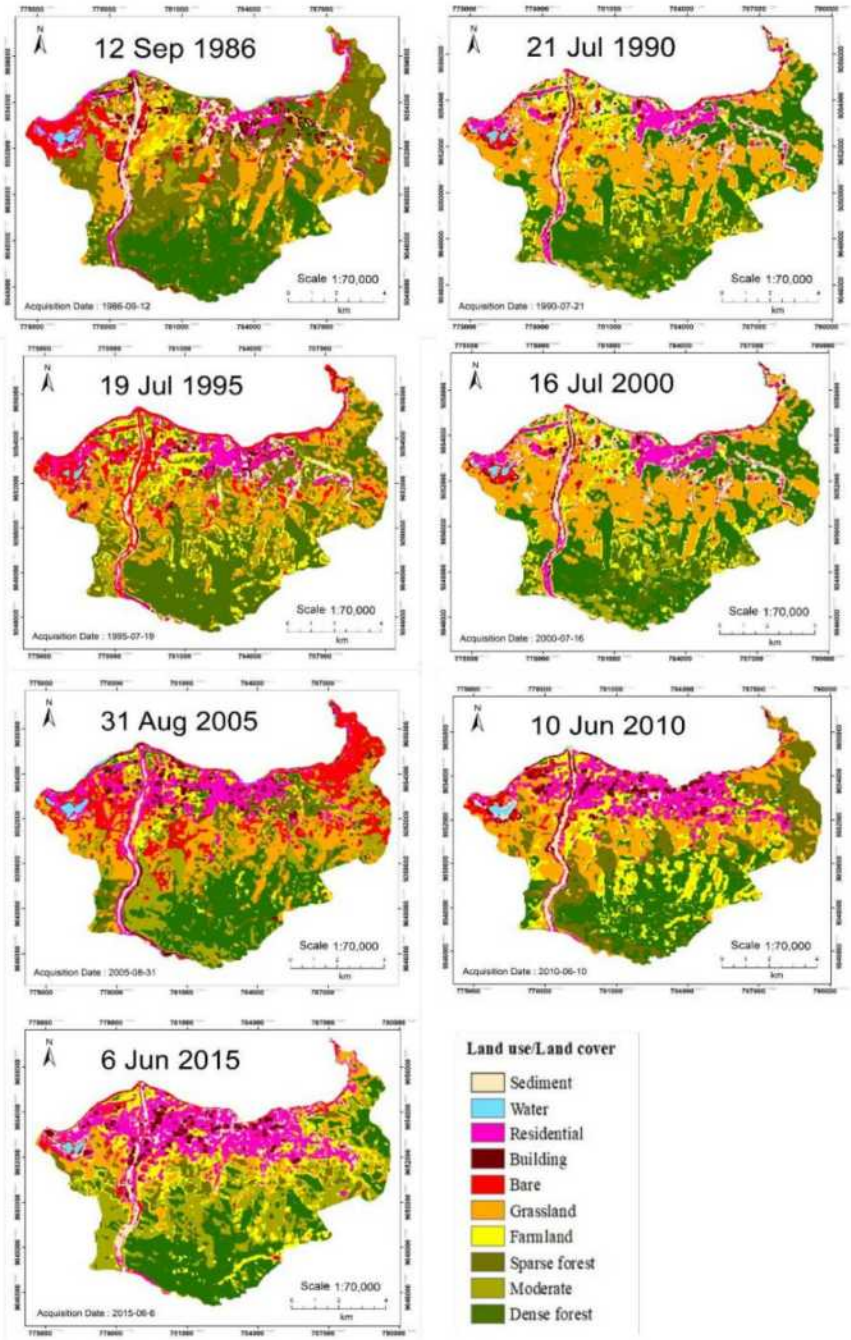

Fig. 2 Land use classification for 1986-2015

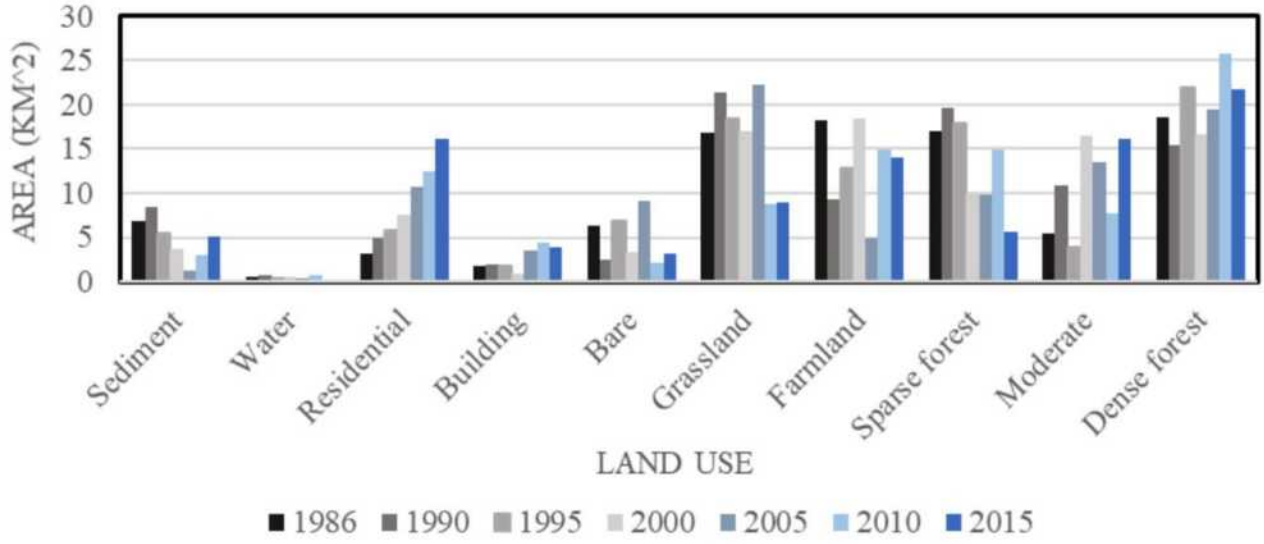

Fig. 3 Annual comparison of the total area for ten land use categories

hand, residential area monotonously increases throughout the period, and building area also shows increasing trend except stagnation or decrease during 1990 to 2000, which meet the period of crisis.

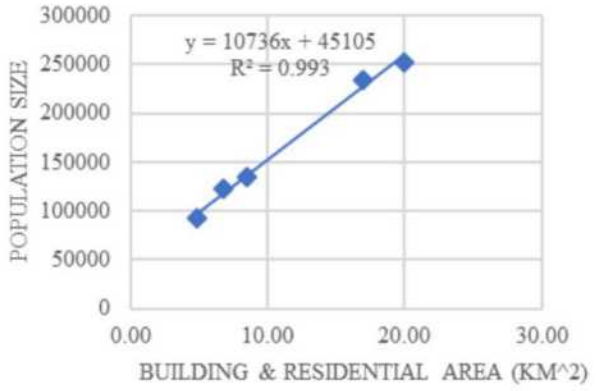

Fig. 4 Formula to estimate the population from building and residential area in Dili

3.2 Population Estimation Base on Land Use

Available Dili population data during the period are in 1990, 2000, 2010, 2015 based on the census and other sources. Figure 4 shows the relationship between population and the building and residential area in Dili. There is a good correlation between building and residential area and population. By using the regression formula in the figure, we can estimate the population of each year.

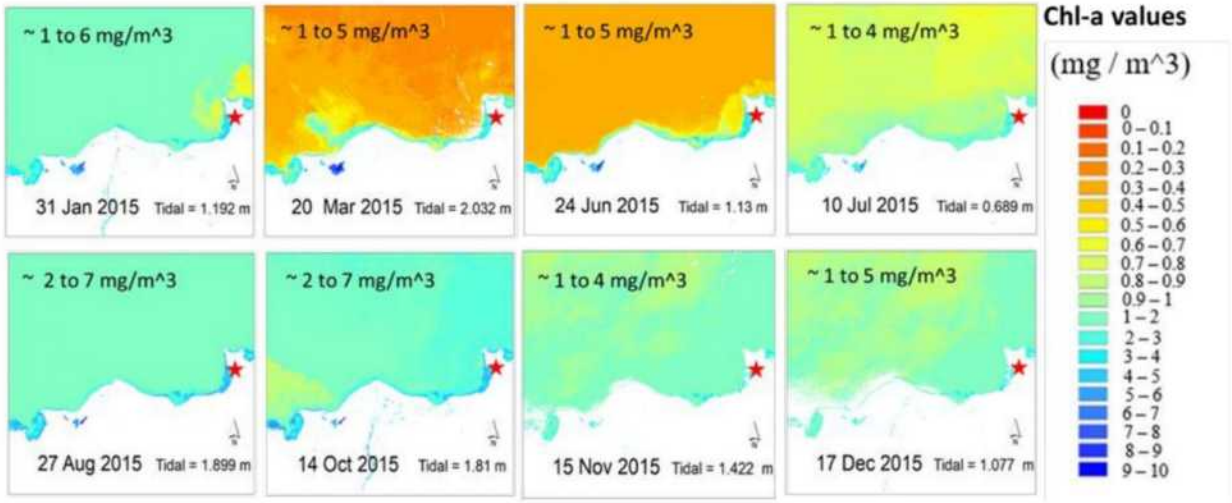

Fig. 5 The Chl-a concentration retrieval from Landsat 8 OLI of 2015

Fig. 6 Chlorophyll measurement on 20th August 2017 at Christ Rei

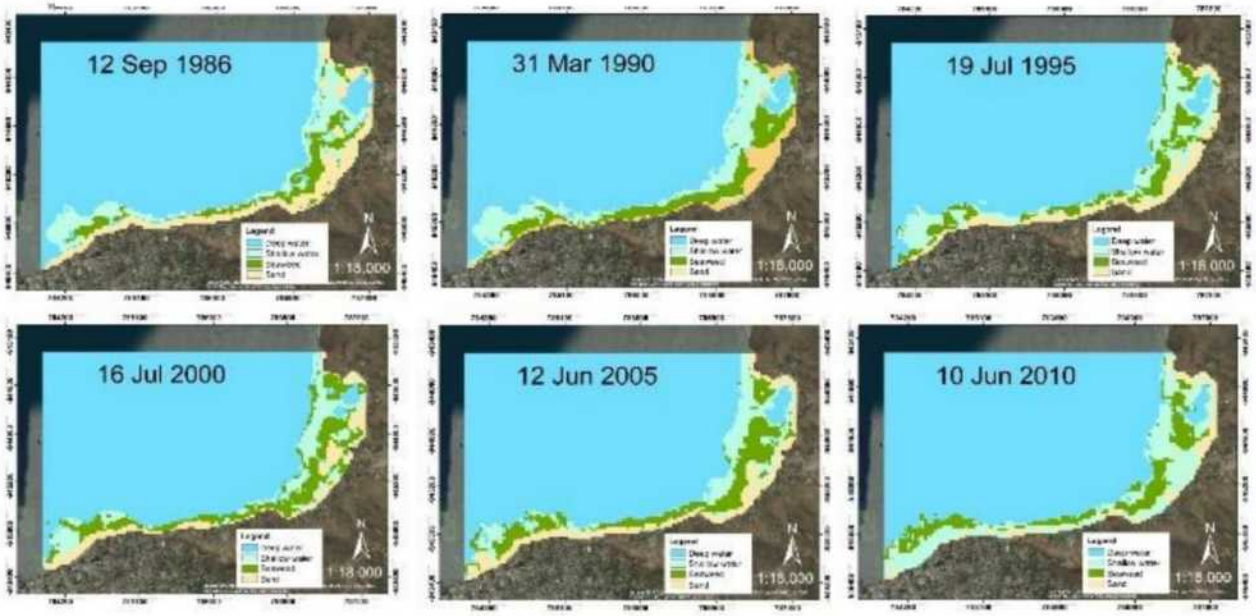

Fig. 7 Estimated maximum seaweed area of the target years

3.3 Estimation of Chl Concentration

By applying Global Chlorophyll Concentration estimation method using available Landsat 8 data throughout 2015 near Dili coast. Figure 5 shows the results. We also measured coastal Chl concentration on 20th August 2017 (Figure 6). The observed Chlorophyll were 1.1 mg/m^3 at the lighthouse, 3.8 at the port, 1.0 at the Cristo Rei beach. However, the satellite estimated Chl in the port tends to be lower than the observation and that at the Christ Rei beach tends to be higher than the observation. This might mean that the Chl by satellite is affected by the turbidity and/or water bottom color near the coastline in the

Fig. 8 Aerial photo of seaweed cover

image. Thus, Chl is not appropriate to represent the coastal water quality.

3.4 Seaweed Area Estimation

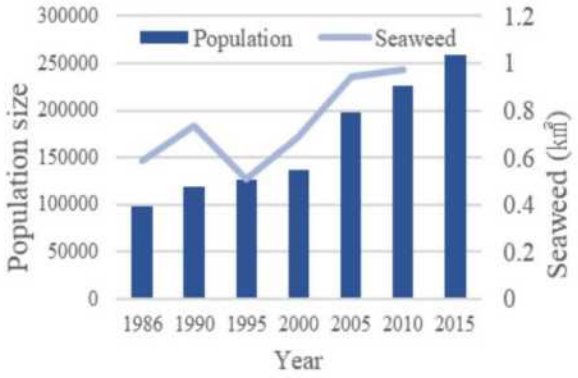

Fig. 9 Time series of population and seaweed area in Dili

The estimated maximum seaweed area during the target years are shown in Figure 7. Figure 8 shows an aerial photo of seaweeds. The overall accuracy and Kappa coefficient are 90% and 0.86 for 2010, 85% and 0.79 for 2005, 85% and 0.79 for 2000, 68% and 0.55 for 1995, 77% and 0.69 for 1990 and 75% and 0.66 for 1986, which are acceptable.

3.5 Population and Seaweed Relationship

Figure 9 shows the seaweed timeseries together with population change. Although population seems continuously increasing, seaweed area once decreased in 1995. This might because some people left their houses and evacuated from Dili during the period of crisis. Generally speaking, seaweed increase when population increase. This result implies that coastal area of Dili had been suffering eutrophication problem caused by increasing population. Appropriate wastewater treatment is required to stop the pollution.

4. Conclusions

We found a strong relationship between population and residential and building area. We also found a relationship between population and seaweed in the coastal area of Dili. Seaweed can be an indicator for coastal water quality in the past. The histrical change of these parameters showed that the population increase in Dili has been causing a possible eutrophication problem in the coastal area. Appropriate wastewater treatment is required to stop the pollution.

Acknowledgement

We are deeply grateful to Mr. Benjamin de O. Martins, Mr. Leandro Madeira Branco, and Mr. Hugo da Costa Ximenes who helped us to improve our understanding of histrical landuse in Dili. We also received generous support from Mr. Justino da Costa Soares, Mr. Alfredo Ferreira, and Mr. Sergio Miguel Freitas during our field work.

References

[1] FAO, "Global forest resources", Assessment 2010 country report in Timor-Leste, Forest Department, FAO, 2010.

[2] G.A. Bouma and H.T. Kokryn, "Change in vegetation cover in East-Timor", 1986-1999. Natural Resource Forum, 28, 1-12, 2004.

[3] M.D.M. Manessa, "Bottom type identification in shallow coral reef ecosystems using imagery satellite data", Graduate Study of Environmental Science, Udayana University, 2012.

[4] O.T. Sandlund, I. Bryceson, D. de Carvalho, N. Rio, J. da Silva, and M.I. Silva, "Assessing Environmental Needs and Priorities in East Timor: Issues and Priorities", UNOPS Report, 2001.

[5] R. G. Congalton, "A review of assessing the accuracy of classifications of remotely sensed data", Remote Sensing of Environment 37:35-46, 1991.

[6] C. Hu, Z. Lee, and B. Franz, "Chlorophyll-a algorithms for oligotrophic ocean: A novel approach based on three-band reflectance difference", Journal of geophysical research, 117 (C1),148-227, 2012.

[7] J.E. O' Reilly and 24 co-authors. "SeaWiFS Postlaunch Calibration and validation analyses", Part 3. Nasa technical memorandum, 11, 49 pp, 2000.

Characteristics of Customer Voltage in Complex Primary Feeder with PV System and Energy Storage System

Marito Ferreira[a] **and Dae-Seok Rho** [b]

[a] *Department of Electrical, Electronic & Communication Engineering, Korea University of Technology and Education, Chugjeol-ro Byeongcheon-myeon, Dongnam-gu, Cheonan-si Chungcheongnam-do, 31253 , Republic of Korea*

[b] *Faculty of Engineering, Science and Technology, Universidade Nacional Timor Lorosa'e, Avenida Hera, Cristo-Rei, Dili Timor Leste*

E-Mail: maritoferreira353@gmail.com, ferr12345@koreatech.ac.kr

Abstract: When PV system is installed and operated with distribution system, there are technical problems that customer voltage should be violated from the allowable limit due to sudden output fluctuation of PV system. In order to overcome this problem, a step voltage regulator (SVR) has been installed and operated in a long- distance primary feeder which is interconnected with PV system in order to maintain an appropriate voltage range in distribution system. This paper proposes to evaluate the voltage characteristics of low voltage customer in distribution system interconnected with the SVR and ESS (energy storage system), based on the control characteristics of the ESS during the delay time of the SVR, by using PSCAD/EMTDC software.

Keywords: step voltage regulator, distribution systems, energy storages system.

1. Introduction

Recently, the renewable energies such as PV system, wind power and fuel cell are being actively interconnected with distribution system [1,4]. However, when large scale PV system is installed and operated in distribution system, the customer voltage should be violated from the allowable limit (220 ± 13V) due to the output fluctuation and reverse power-flow of the PV system [5]. Therefore, it is required to develop the technology that can interconnect a large scale of the PV system with distribution systems in a stable manner while maintaining a voltage quality within a proper range. Under these circumstances, a step voltage regulator (SVR) has been installed and operated in a long-distance primary feeder which is interconnected with PV system, in order to maintain an appropriate voltage range in distribution system. However, the SVR has characteristics of tap operation with pre-set delay time, so that during the delay time the customer voltage may be violated from the allowable limit. Because the SVR cannot maintain a customer voltage within the allowable limit, a new approach is highly required [6,7].

This paper proposes to evaluate the voltage characteristics of low voltage customer in distribution system interconnected with the SVR

and ESS(energy storage system) based on the control characteristics of the ESS during the delay time of the SVR, by using PSCAD/EMTDC software and then analyzes the customer voltage according to the operation of the SVR and ESS. From the simulation results, it is clear that customer voltage can be maintained within the allowable limit and also the proposed method is a practical and effective approach to control the customer voltage in distribution system with the PV system.

2. Characteristics of Voltage Regulation in Distribution System

Unlike existing distribution system which consists of only a substation (power source) and customer voltage (load), a complex distribution system interconnected with PV system, ESS has complex and bi-directional flow due to small scaled PV system located at the customer side. As a result of the actual problem caused by the operation of PV system, an instability, i.e., under voltage and overvoltage phenomena for customer side is occurred due to the interconnection of the PV system, as shown in Fig. 1.

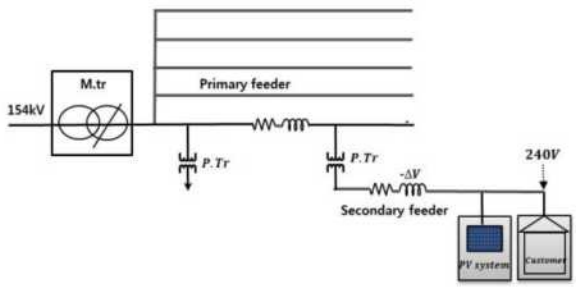

Fig. 1 Under and over-voltage cases

2.1 Operation Characteristics of SVR

When PV system is operated and interconnected with a primary feeder (22.9kV) as shown in Fig. 2, the load current of distribution feeder is changed and then customer voltage may be violated from the allowable limit. Therefore, the tap position of the pole transformer should be changed, but practically, it is difficult to change tap position depending on the operating condition of the PV system.

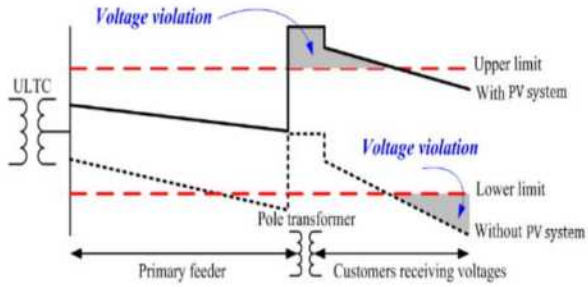

Fig. 2 Operation condition of SVR

2.2 Coordination Characteristics between SVR and ESS

Tap position of SVR is generally decided by compensation-rate of SVR based on the conventional LDC (line drop compensation) method and tap operation is carried out by considering a setting value of delay time. Therefore, the power instability such as under voltage and over-voltage could occur during the delay time. In order to overcome these problems, this paper proposes a coordination operation method between SVR and ESS. At first, during the delay time of SVR, ESS is operated as a discharging mode when customer voltage violates lower limit, in contrast, if it is charging mode when customer violate upper limit as shown in Fig. 3.

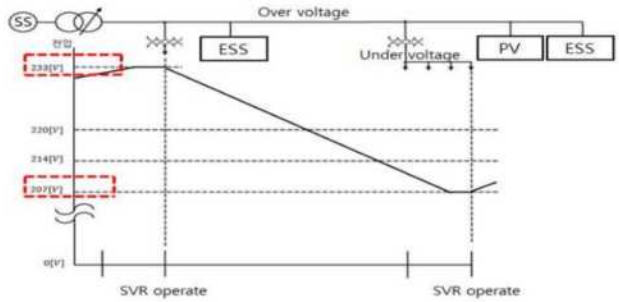

Fig. 3 Voltage regulation of distribution system using SVR and ES

And also, in order to obtain a proper introduction capacity of ESS, this paper presents a modified tap control mode of SVR as shown in Fig. 4. The idea of modified mode is to exclude ESS current from passing a current of SVR when customer voltage violates the allowable limit during the delay time of SVR. Mode ① of Fig. 4 shows a profile of passing current in SVR excluding ESS current and mode ② represents a concept of tap operation in SVR, which is performed after the delay time when variation amount of passing current in SVR reaches to tolerance level. Mode ③ is a mechanism to operate ESS by considering mode ① and ② of at which ESS is operated only during the delay time to keep customer voltages within the allowable limit.

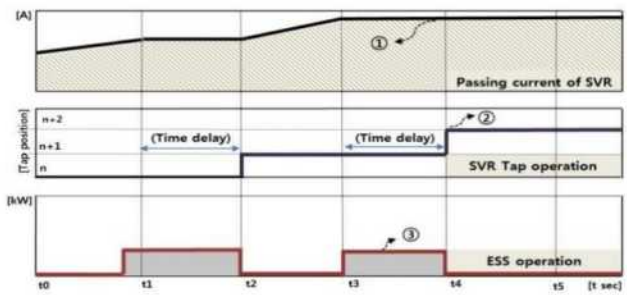

Fig. 4 Concept of tap operation by modifying SVR control mode

3. Modeling of Complex Distribution System using PSCAD/EMTDC

3.1 SVR Modeling

The LDC method of SVR can be illustrated as shown in Fig. 5. Where, the optimal sending voltage is decided by load center voltage (Vce) and equivalent impedance (Zeq) according to variation of passing current in SVR (Ipass(t)) at each time interval.

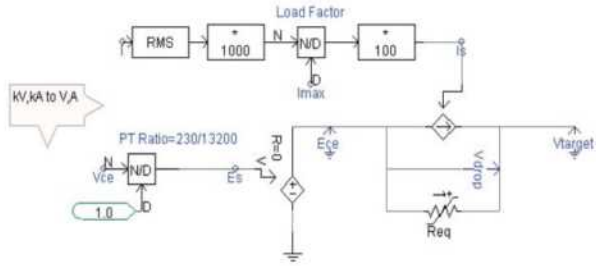

Fig. 5 Modeling of LDC method

By using the LDC method of SVR as mentioned earlier, the tap operation is expressed as shown in Fig. 6, considering with the bandwidth of 50 % and predesigned delay time of 30 seconds. It is composed of tap up (a) and tap down (b) operation, where, tap operation logic is decided by voltage variation (Er), integration element and comparator during the delay time (Td).

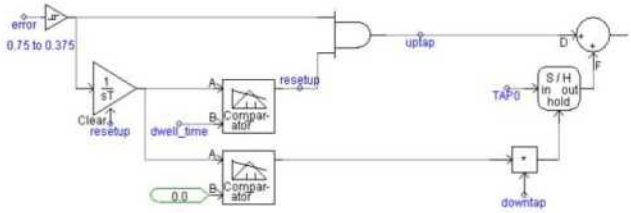

(a) Tap Up logic

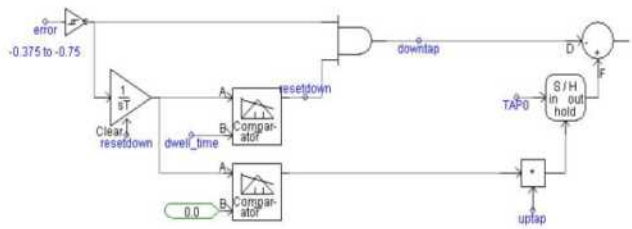

(b) Tap down logic

Fig. 6 Tap up and down logic of SVR

And also, Fig. 7 is an SVR modeling by tap value, calculating in the internal algorithm and applied to SVR with single phase Y-Y connection of three transformers to maintain the customer voltage within the allowable limit.

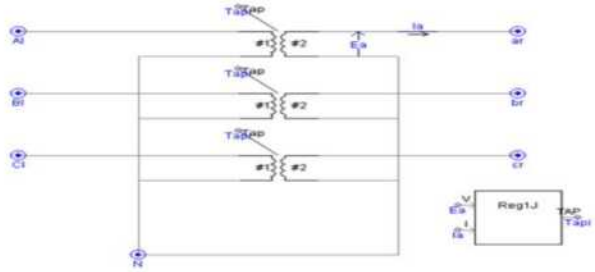

Fig. 7 Modeling of SVR

3.2 PV System Modeling

Figure 8 is a detailed current control algorithm using PI controller, in order to control the target active and reactive power for the artificial PV systems. Here, V_d, V_q are the d-q axis voltage for the output inverter, the references current I_{ref-d_q} of the output inverter I_d , I_q are output current inverter which is converted to q-axis, q-axis and V_{sq} is instantaneous voltage of distribution system. Also, since the current control unit is a decoupling, it is possible to independently control the active and reactive power. Then, the current control algorithm is a control method of the grid-connected inverter modeling of PV system, and V_d and V_q are output voltage of inverter converted into three-phase through d-q coordinate conversion and it converted into six PMW signals for driving the IGBT.

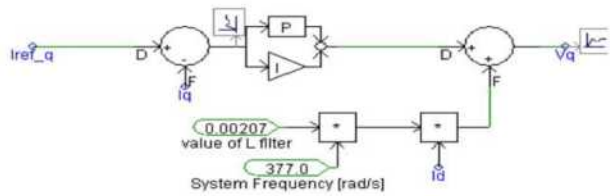

(a) Modeling of current control (q-axis)

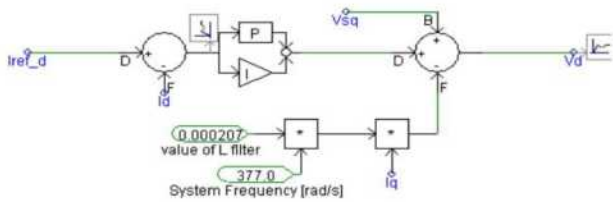

(b) Modeling of current load control (d axis)

Fig. 8 Modeling of current control in PV system.

On the other hand, as shown in Fig.9, Ref. [9] is a modeling grid connected to the grid, an IGBT driven by six switching signals from PWM converts to output DC generated the PV system into three-phase output AC with a different phase of 120° and sent to the system.

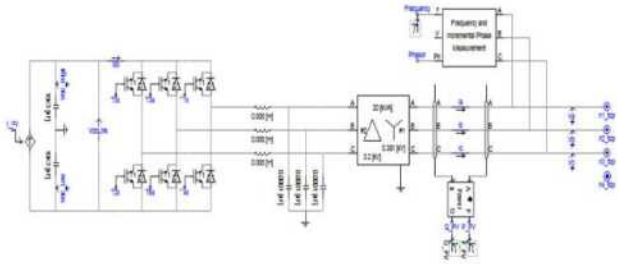

Fig. 9 Modeling of current control of PV system

3.3 ESS Modeling

In order to obtain the desired active and reactive powers of ESS, this paper adapts current control algorithm are shown in Eqs. (1) and (2). In this process, the decoupling control algorithm of active and reactive power of PV system is introduced. Here, to obtain the reference value for the desired current, the DC voltage is controlled by the PI (Proportional Integral) controller. The 3-phase voltage of distribution system is converted into 2-phase current of the d-q stationary coordinate by using the d-q transformation method. And then a 2-phase current is transformed into DC current of the d-q synchronizing coordinate to easily control the desired voltage and current.

$$V_d = (I_{dref} - I_d) \cdot \left(kp + \frac{ki}{s}\right) - I_q \cdot \omega + e_d) \quad (1)$$

$$V_d = \left(I_{qref} - I_q\right) \cdot \left(kp + \frac{ki}{s}\right) - I_q \cdot \omega Ls + \quad (2)$$

Where V_d is voltage of d-axis, V_q is voltage of q axis, $\left(kp + \frac{ki}{s}\right)$ is PI controller

I_{dref} and I_{qref} are the desired active and reactive current, ωL is internal reactance for feed-forward compensation e_d and e_q are instantaneous voltage d axis and q axis. In general, instantaneous active power (P) and reactive power (Q) in balanced 3-phase system can be expressed as shown in Eq. (3) with the concept of the d-q axis variables.

$$P = \frac{3}{2}\left(V_d I_d - V_q I_q\right), \quad Q = \frac{3}{2}\left(V_q I_d - V_d I_q\right) \tag{3}$$

where, $|V_0|$ is the magnitude of instantaneous voltage because, with the synchronous speed (ω) in the d-q coordinate method is equal to the magnitude of instantaneous voltage and is zero, reference current of d-q axis as shown in Eq. (4) can be obtained from Eq. (3).

$$P = \frac{3}{2}|V_0| I_{qref} = -\frac{3}{2}|V_0| I_{dref} \tag{4}$$

Based on the current control algorithm in Eqs. (3) and (4), modeling of ESS to enable control for changing and discharging is carried out by PSCAD/EMTDC as shown in Fig. 10.

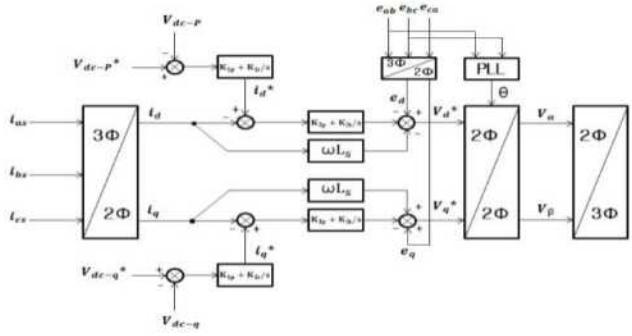

Fig. 10 Modeling of ESS

3.4 Entire System Modeling

Based on the modeling of each component mentioned earlier, this section performs the total modeling of complex distribution system interconnected with PV system, SVR and ESS as shown in Fig. 11.

4. Simulation and Test Results

(1) Simulation Conditions

In order to analyze the characteristics of customer voltage by ESS operation when customer voltage in distribution feeder interconnected with PV system violates the allowable limit, the simulation conditions are presented in Table 1.

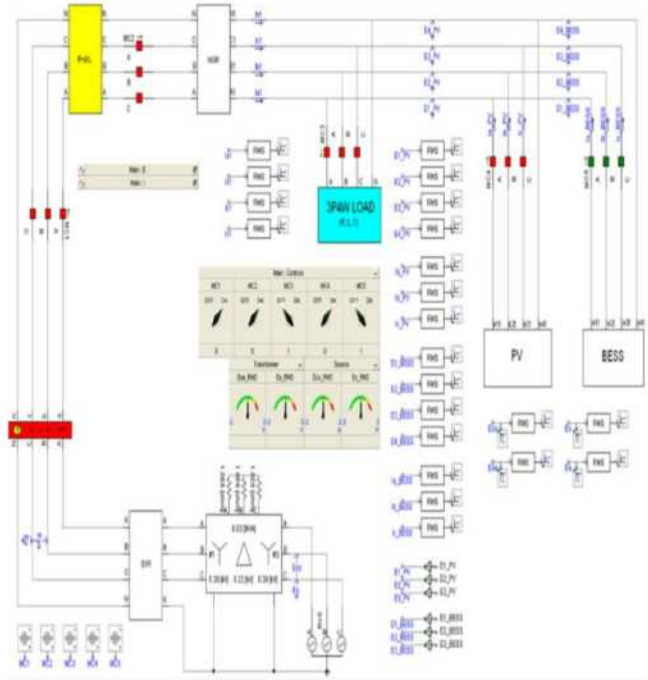

Fig. 11 Modeling of complex distribution system.

Table 1. Simulation conditions

Test conditions	Over voltage characteristics		Under voltage characteristics	
	Case 1	Case 2	Case 1	Case 2
Customer voltage	233[V]	234[V]	204[V]	204[V]
Load	0.8+j0.2 [KVA]	0.7+j0.3 [KVA]	2.4+j0.6 [KVA]	2.0+j0.9 [KVA]
Power factor	0.97	0.91	0.97	0.91
impedance	1.4+j0.8[Ω]		1.4+j0.8[Ω]	

Gris voltage	220[V]	220[V]
PV system	3[kW]	0[kW]

(2) Customer Voltage Characteristics using PSCAD/EMTD

When the ESS is operated during the delay time of SVR and operation of ESS is stopped after a fixed time interval while the SVR is operated, the operation characteristics of SVR and ESS are shown in Fig. 12. Here, the characteristics of customer voltage are classified into 3 sections, section ① is the initial condition when PV system is operated, section ② is the condition that ESS is operated and section ③ is the condition when ESS is stopped and SVR is operated. Therefore, when customer voltages are increased to 233V, as shown in section ① due to reverse power flow of PV system and the load conditions, ESS performs charging operation by 200W and then customer voltage is decreased to 232V, as shown in section ②. Therefore, it is confirmed that customer voltage is kept with allowable limit by the tap operation of SVR even though ESS is stopped, as shown in the section ③.

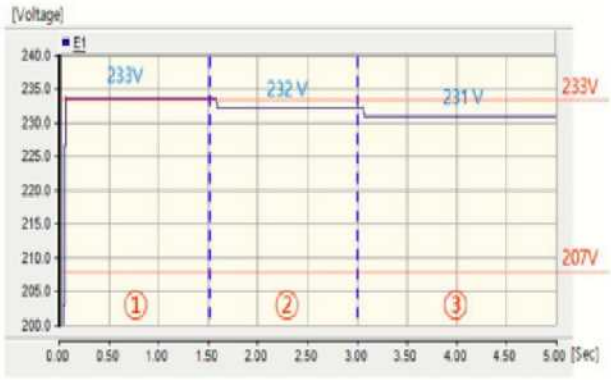

Fig. 12 Characteristics of customer voltages.

Also, when customer voltages are increased to 234V as shown in section ① of Fig. 13 due to reverse power flow of the PV system and the load conditions, ESS performs charging operation by 400W and then customer voltage is decreased to 233, as shown in section ② Therefore, it is confirmed that customer voltage is kept with allowable limit by the tap operation of SVR even though ESS is stopped, as shown in section ③.

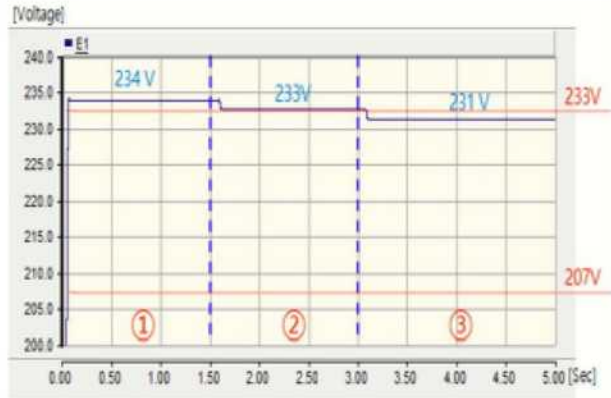

Fig. 13 Characteristics of customer voltages

When the ESS is operated during the delay time of SVR and operation of ESS is stopped after a fixed time interval while the SVR is operated, the operation characteristics of SVR and ESS can be expressed as shown in Fig. 14. Here, the characteristics of customer voltage are classified into 3 sections, section ① is the initial condition, section ② is the condition that ESS is operated and section ③is the condition when ESS is stopped and SVR is operated. Also, when the customer voltages are decreased to 202V, as shown in section ①. ESS performs discharging operation by 800W and then customer voltage is increased to 208V, as shown in section ②. Therefore, it is confirmed that customer voltage is kept with allowable limit by the tap operation of SVR even though ESS is stopped, as shown in section ③

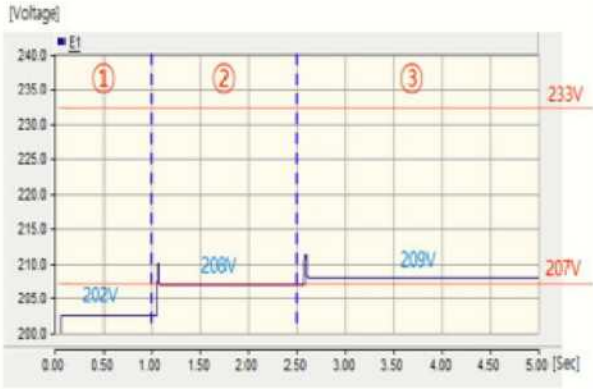

Fig. 14 Characteristics of customer voltages

When the customer voltages are decreased to 204V as shown in section ①of Fig. 15, ESS performs discharging operation by 500W and then customer voltage is increased to 208V, as shown in section ②Therefore, it is confirmed that customer voltage is kept with allowable limit by the tap operation of SVR even though ESS is stopped.

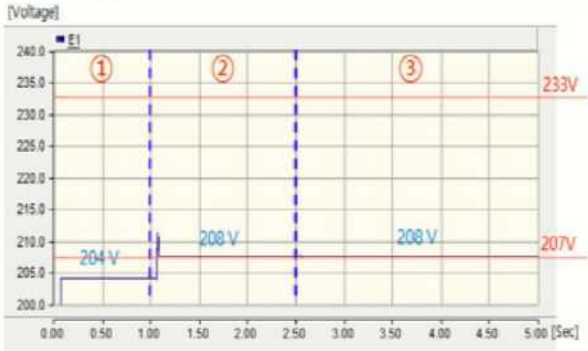

Fig. 15 Characteristics of customer voltages

5. Conclusions

This paper proposed how to evaluate the voltage characteristics of customer voltage in distribution system interconnected with SVR and ESS, based on the control characteristics of ESS during delay time of SVR, by using PSCAD/EMTDC software. When PV system is operated and interconnected with distribution system the customer voltage may violet the allowable limit. It was confirmed that under-voltage and over-voltage could be occurred at the customer side because of the reverse power flow of the PV system. And also, when customer voltage violet the allowable limit (207 to 233V) it can be maintained within the allowable limit by the operation of ESS during delay time of the SVR. In addition, when the customer voltage violates the allowable limit (207 to 233 V), customer voltage was kept with allowable limit by the tap operation of SVR even though ESS is stopped.

References

[1] James J. Burke, "Power Distribution Engineering ", Marcel Dekker, Inc. pp. 320-348, 1994.

[2] Shuhei Takahashi, Yasuhiro Hayashi, Masaki suji, Eiji Kamiya, "Method of Optimal Allocation of SVR in Distribution Feeders with Renewable Energy Sources", Journal of International Council on Electrical Engineering, Vol. 2, No. 2, pp. 159-165, 2012.

[3] Tomonobu Senjyu, Yoshitaka Miyazato, Atsushi Yona, Naomitsu Urasaki, Toshihisa Funabashi, "Optimal Distribution Voltage Control and Coordination with Distributed Generation", IEEE Transactions on Power Delivery, Vol. 23, No. 2, pp. 1236-1242, April 2008.

[4] B. Kim and D. Rho, "A Study on the Voltage Stabilization Method of Distribution System Using Battery Energy Storage System and Step Voltage Regulator", Journal of Electrical Engineering &Technology, Vol.12 No.1, pp11-18, 2017

[5] B. Kim and D. Rho, "Optimal Voltage Regulation Method for Distribution System with Distributed Generation Systems Using the Artificial Neural

Networks", Journal of Electrical Engineering &Technology, Vol.8, No. 4, pp. 712~718, 2013.

[6] D. Rho, K. Kook and Y. Wang, "Optimal Algorithms for Voltage Management in Distribution Systems Interconnected with New Dispersed Sources", Journal of Electrical Engineering &Technology, Vol.6, No. 2, pp. 192-201, 2011

[7] D. Rho and Y. Oh, "Economic Evaluations of Secondary Battery Energy Storage Systems in Power Distribution Systems", Trans KIEE.Vol.49A, No.4, April 2000.

Current–Voltage Characteristics of Si-Based Solar Cells: Effects of Potential Induced Degradation

R. J. Freitas [a,b] and K. Shimakawa [c]

[a] *Department of Electrical and Electronic Engineering, Faculty of Engineering, Science and Technology, UNTL, Timor Leste*

[b] *Renewable Energy and Environmental Research (REER) – Faculty of Engineering, Science and Technology, UNTL, Timor Leste*

[c] *Department of Electrical and Electronic Engineering, Gifu University, Gifu 501-1193, Japan*

E-Mail: ruben.freitas@untl.edu.tl

Abstract: It is known that high voltage with photo irradiation causes degradation of output performances in Si photovoltaic (PV) module. This is called the potential induced degradation (PID). PID is replicated well with the simulation of the current-voltage characteristics with changing the physical parameters. Some origins of PID in the Si solar cells will be discussed in terms of sodium diffusion into *n*-layer.

Keywords: Solar cell *I–V* curve, potential induced degradation, shunt resistance, sodium diffusion

1. Introduction

Potential induced degradation (PID) was first reported by the Jet Propulsion Laboratory in 1985 for both crystalline Silicon (c-Si) and amorphous silicon (a-Si). PID has then become an important issue, which causes degradation of output performances of PV module [1]. PID tends to occur even immediately after the installation of the system with higher power output reduction in comparison with other typical degradation, such as corrosion by acetic acid and delamination of electrodes [2].

Although the definition of PID is still not well established, PID is reported to be commonly observed in all level of PV parts i.e. cell, panel, and systems which are operated at high negative voltages, temperature, and humidity [2, 3]. PID itself can be suppressed by changing materials of module components such as front cover of PV being replaced with materials without alkali components or with coating the glass to inhibit the ion migration. All these will reduce the leakage current, and high resistance material should be used for encapsulant [1, 2].

Numerous researches have been carried out to find the root causes of PID. It was reported by SOLON in 2010 that PID effects have one common characteristic that the degradation is depending on polarity and level/extent of the potential between cell and ground which is determined by the actual configuration of the PV system [3]. The typical method commonly employed to measure the degradation mechanisms can be macroscopic analysis; e.g.,

current-voltage (*I–V*) measurements, electro-luminescence imaging, and secondary ion mass spectrometry [1-4].

In this paper, we simulate the effect of PID on the *I-V* characteristics of Si-based solar cells using an equivalent circuit. It is found that the *I-V* curve is significantly affected by carrier recombination (recombination current). The cause of this will be discussed in terms of sodium diffusion into Si.

2. Current–Voltage (*I–V*) Characteristics

2.1 Basic Approach of Simulation

Let us start by introducing an equivalent circuit of a solar cell as shown in Fig.1.

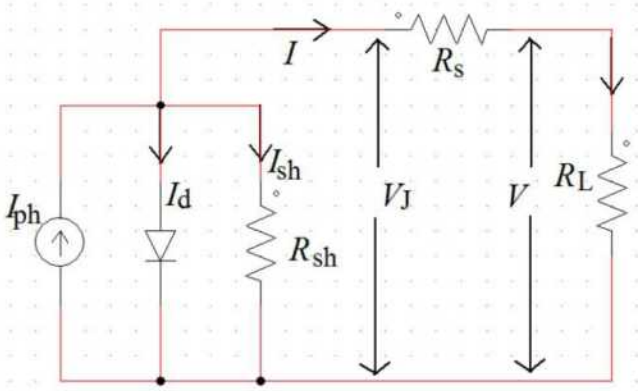

Fig. 1 Equivalent circuit of solar cell

When a solar cell (diode) is exposed to light, photocurrent I_{ph} is generated. The direction of current flow is shown in Fig. 1. The circuit should be composed of shunt resistance R_{sh} and series resistance R_s that will be useful for interpreting losses in the circuit. This is a type of leakage current. Here, R_L is the load resistance, V is the output voltage, V_J is junction voltage, I_{sh} and I are shunt current and output current respectively, and I_d is the diode current which is represented by well-known equation as

$$I_d = I_0\left(e^{\frac{qVj}{nkT}} - 1\right), \tag{1}$$

where, I_0 is a saturation current, n is ideality factor (1~2), k is the Boltzmann constant and T is the absolute temperature.

From Fig.1, I is given as

$$I = I_{Ph} - I_d - I_{Sh}$$

$$= I_{Ph} - I_0\left[\exp\left\{\frac{q(V+IR_S)}{nkT}\right\} - 1\right] - \frac{V+IR_S}{R_{Sh}}. \tag{2}$$

It should be noted from Eq. (2) and Fig.1 that V under illumination condition is given by

$$V = V_j - IR_S, \tag{3}$$

On the other hand, the *I-V* curve under the dark condition V is given as

$$V = V_j + IR_S. \tag{4}$$

The both sides of Eq. (2) involve I, and hence a special care should be taken into account to solve it.

2.2 Simulation Results

Before proceeding with discussion, we show the simulation results under illumination and under dark conditions.

Figures 2 and 3 show *I-V* curves under illumination and dark conditions, respectively, when R_{sh} is taken to be 10 Ω, 100 Ω, and 1 kΩ, while the fixed parameters are T = 300 K, I_0 = 1×10^{-6} A, R_s = 0.05 Ω, and n = 2 for Si. Note that I_{ph} = 0.1 A under illumination was used and I_{ph} = 0 under dark condition. We find that

the *I-V* curves are changed drastically below $R_{sh} \sim 100\ \Omega$.

Figures 4 and 5 show the simulated *I-V* curves under illumination and dark conditions when I_0 is varied 1×10^{-6} A, 1×10^{-7} A, and 1×10^{-8} A, while fixed parameters are set in T = 300 K, R_s = 0.05 Ω, R_{sh} = 10 kΩ, and n = 2. Note again that I_{ph} = 0.1 A under illumination and we take I_{ph} = 0 without illumination. Drastic change in *I-V* curves is found above $I_0 \sim 1 \times 10^{-6}$ A.

Figure 6 shows the output power P as a function of R_{sh} when it is set to be 10 Ω, 100 Ω, and 1 kΩ. Figure 7 shows the maximum power P_{max} when R_{sh} is varied from 1 Ω–1 kΩ. It looks that the value of R_{sh} is the most important parameter on the *I-V* curve. Note that P_{max} drops significantly in the condition of $R_{sh} < 100$ Ω.

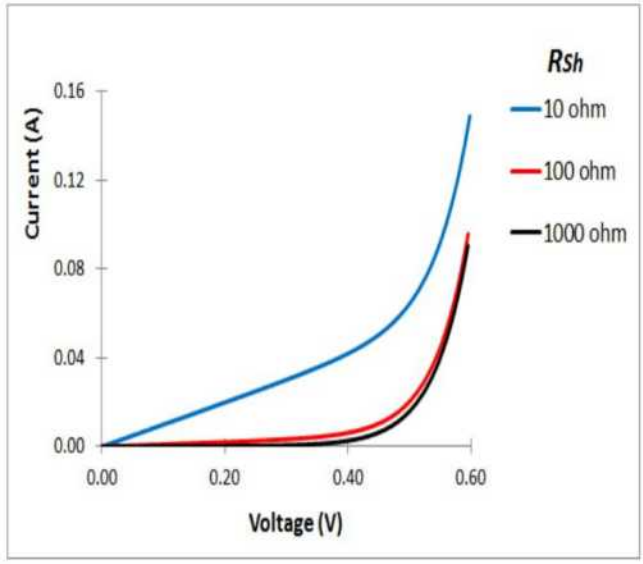

Fig. 3 *I–V* curves under dark condition as a function of R_{sh}

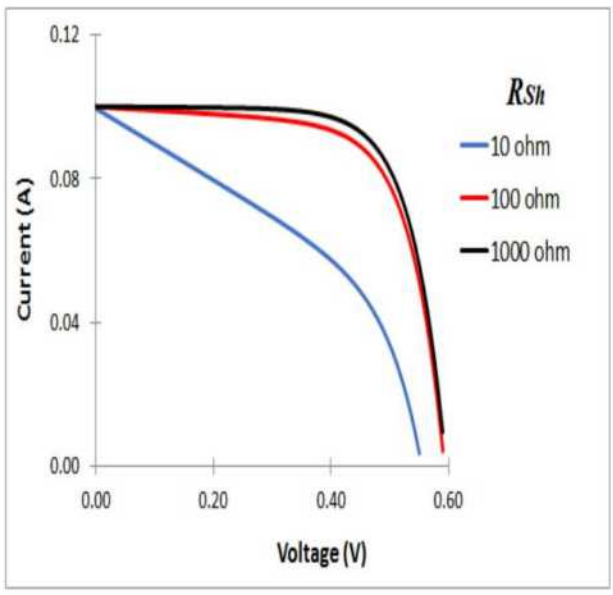

Fig. 2 *I–V* curves under illumination as a function of R_{sh}

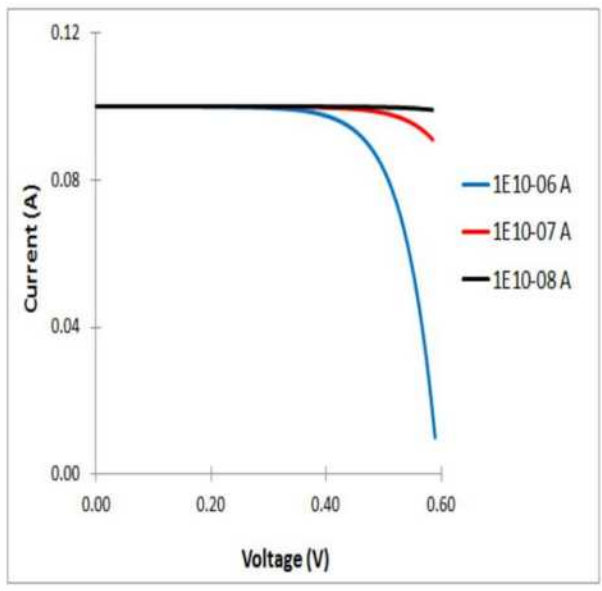

Fig. 4 *I–V* curves under illumination as a function of I_0

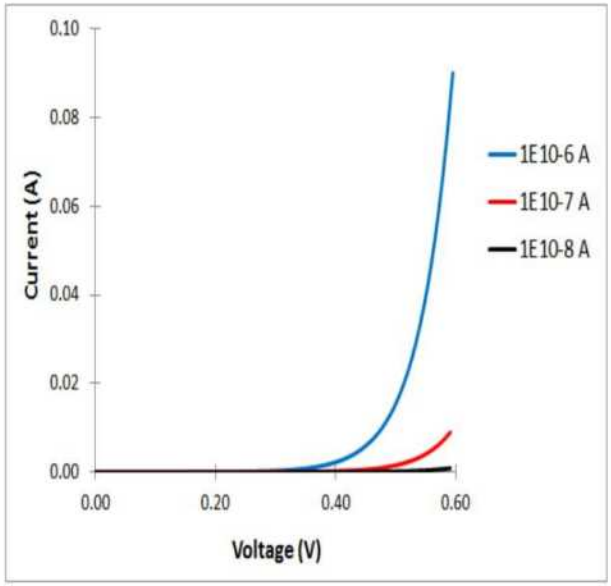

Fig. 5 *I–V* curves under dark condition as a function of I_0

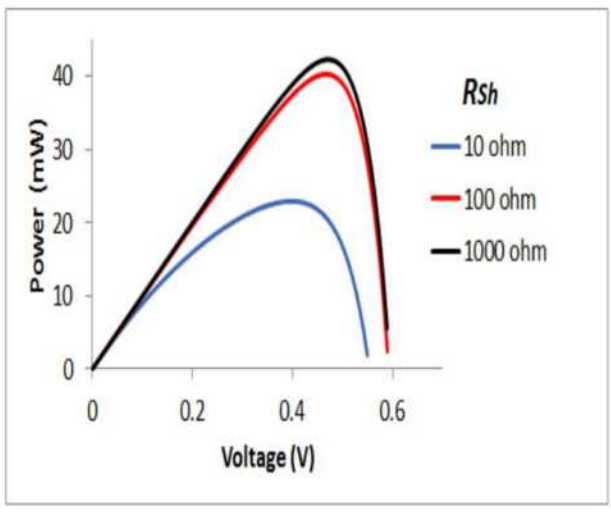

Fig. 6 *P–V* curves as a function of R_{sh}

3. Discussion

Let us now discuss the simulation results stated in section 2. As shown in Fig.2 R_{sh} influences *I-V* curves most significantly. Under the illumination, the *I-V* curve degrades when R_{sh} is decreased. A higher appropriate value of

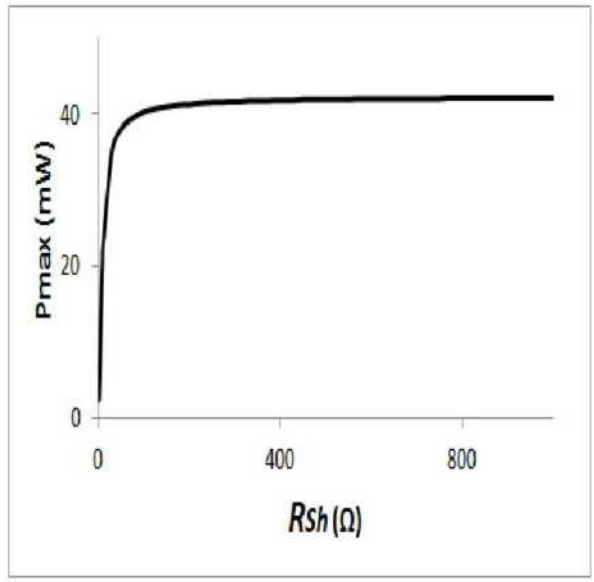

Fig. 7 Relation between P_{max} and R_{sh}.

R_{sh} leads to higher output power and also its maximum P_{max} as shown in Figs. 6 and 7, respectively. Ideal shape of *I-V* curve for large R_{sh} is obtained under the dark condition as shown in Fig.3.

To understand why R_{sh} influences the *I-V* curves (hence output power performances), we discuss an origin of R_{sh} itself. Note that *p-n* diode energy diagram is divided into three layers, i.e., *n*-layer, depletion region, and *p*-layer. Firstly, carrier recombination induces a decrease of R_{sh}. Secondly, small R_{sh} is attributed to leak current through bad depletion layer. Under illumination, excess electrons and holes are induced by illumination which causes an increasing of photocurrent. When the excess electrons and holes are recombined, they lead to a decrease in photocurrent which corresponds to the small R_{sh}. These are shown in Figs. 2, 3, 6, and 7.

It is found in Figs. 4 and 5 that the variation of saturated current I_0 also influences the shape of the *I-V* curve. A decrease of I_0 enhances the solar cell performance, resulting in higher output power.

It is known that reversible or irreversible PID has been found. The reversible PID returns to the original *I-V* condition, with some means; e.g., applying positive high voltage to the cell.

Let us discuss why R_{sh} decreases with illumination. The PID, either irreversible or reversible, is known to be caused by diffusion of sodium (Na) into the *n*-layer. Certain amount of Na-ions (Na^+) released from the soda lime glasses drifting through encapsulation layer which will then accumulate in the surface of the SiN_x anti-reflective coating (ARC) layer. In some case, Na^+ diffuses into the depletion layer (*p-n* junction) [1, 2, 4-7], causing irreversible PID.

Under the illumination, Na^+ diffuses into the *n*-layer and capture free electron of the conduction band;

$$Na^+ + e \rightarrow Na. \quad (5)$$

This reaction is a type of recombination that leads to a reduction of photocurrent, which can be equivalent to an increase of I_{sh} (See Fig.1). Further Na^+ diffusion might reach the depletion region which may act as recombination center in the depletion layer, and causes further reduction of photocurrent (irreversible).

In this paper, we focus only on recombination that occurs at the *n*-layer (reversible). Thus the increases of recombination rate cause the reduction of R_{sh}. This can be the main for the PID to occur. A loss of free electron (Eq. (5)) induces the Fermi-level shift (downward to the center of band gap) in the *n*-layer. Then the built-in potential V_D decreases, resulting in an increase of saturation current I_0. The PID may also be related to this effect.

4. Conclusion

The origin of PID on Si-based solar cells was discussed. The carrier recombination originated from the diffusion of sodium ion Na^+ into *n*-layer of Si causes the reduction of photocurrent (decreases of R_{sh}). This is the main reason for the PID to occur.

The presented results were model simulation only. The comparison with the experimental data will be presented in a future paper.

Acknowledgement

RJF wish to thank Profs. S. Nonomura, H. Yoshida and F. Ohashi, and their laboratory members for giving an opportunity to join the experimental work related to the PID in Gifu University. We would like to thank Mr. A. Takahashi (JICA-CADEFEST II project) for supporting this research activity.

References

[1] W. Luo, Y. S. Khoo, P. Hacke, V. Naumann, D. Lausch, S. P. Harvey, J. P. Singh, J. Chai, Y. Wang, A. G. Aberle, and S. Ramakrishna, "Potential-induced degradation in photovoltaic modules: a critical review", Energy Environ. Sci. **10**, 43, 2017.

[2] F. Ohashi, Y. Mizuno, H. Yoshida, H. Kosuga, T. Furuya, R. Fuseya, R. J. Freitas, Y. Hara, A. Masuda, and S. Nonomura, "Sodium distribution at the surface of silicon nitride film after potential-induced degradation test and recovery test of photovoltaic modules", Japanese Journal of Applied Physics **57**, 08RG05 , 2018.

[3] J. Berghold, O. Frank, H. Hoehne, S. Pingel, B. Richardson, and M. Winkler, "Potential Induced Degradation of solar

cells and panels", Proc. 25th European Photovoltaic Solar Energy Conf. Exhib./5th World Conf. Photovoltaic Energy Conversion, p. 3753, 2010.

[4] S. Jonai and A. Masuda, "Origin of Na causing potential-induced degradation for p-type crystalline Si photovoltaic modules", AIP ADVANCES **8**, 115311, 2018.

[5] V. Naumann, D. Lausch, A. Hahnel, J. Bauer, O. Breitenstein, A. Graff, M. Warner, S. Swatek, S. Groβer, J. Bagdahn, and C. Hagendorf, " Explanation of potential-induced degradation of the shunting type by Na decoration of stacking faults in Si solar cells", Solar Energy Materials & Solar Cells **120**, 383-389, 2014.

[6] V. Naumann, D. Lausch, A. Graff, M. Warner, S. Swatek, J. Bauer, A. Hahnel, O. Breitenstein, S. Groβer, J. Bagdahn, and C. Hagendorf, "The role of stacking faults for the formation of shunting during potential-induced degradation of crystalline Si solar cells", Phys. Status Solidi RRL**7**. **No. 5**, 315-318, 2013.

[7] P. echner, S. Hummel, D. Geyer, and H. Mohring,"PID-Behavior of Thin-Film and c-Si PV-Modules", proceedings of the 28th European Photovoltaic Solar Energy Conference and Exhibition, p.2810-2815, 2013.

Analysis of Tide Level in Frequency Domain at Dili Port: Origin of 1/*f* Fluctuations

Abelito Filipe Belo[a], Kenji Sasa[b], Jose Madeira Marques[b] and Koichi Shimakawa[c]

[a] *Faculty of Engineering Science and Technology, Universidade Nacional Timor Lorosa'e, Hera, East Timor*

[b] *Dili Port Authority, Edificio Central da APORTIL, Dili, East Timor*

[c] *Department of Electrical and Electronic Engineering, Gifu University, Gifu 501-1193, Japan*

E-Mail: abelitofilipe@gmail.com

Abstract:

The frequency spectrum of tide level at Dili port is obtained by the Fast Fourier Transform (FFT) of the tide level during 4 months in time-domain. The spectrum shows two special peaks which are related to the gravitational motions of the moon and the sun, combined with the so-called 1/*f* fluctuation. The frequency spectrum is a type of low pass filter in electrical circuit and is approximately replicated well by a RC series connection, which is a Debye-type relaxation in dielectrics. This equivalency may cast a new insight for the 1/*f* noise. It is also reported that the histogram of the tide level in time-domain is approximated to be the Gaussian or the Weibull distribution function.

Keywords: Tide Level, Fast Fourier Transform (FFT), 1/f Noise, RC Equivalent Circuit

1. Introduction

Tide level should have time-to-time variations (time domain), involving periodic cycles [1,2]. The character of the fluctuations can be examined in several ways: One simple method is to construct a histogram of the step size in output over time [3,4], and other one is to obtain a frequency spectrum (frequency domain) [5,6]. One of the techniques to obtain the frequency spectrum should be the Fourier Transform (FT) [2]. It is known that the tidal wave has so called "1/*f*" noise spectrum [2], which is widely observed in nature [7].

The gravitational attraction of the moon and the sun, and the earth rotation are the main origin of periodic change in the tide level. For any site, their height depends on the location of the Sun and the Moon. Additionally, atmospheric pressure and wind power etc. should also contribute to the fluctuations in the tide level, as well as the shape of the beach, coastline, and coastline depth [1,5]. All for these prevailing ocean currents may dominate 1/f character.

We report, for the first time, the frequency spectrum (FS) (frequency domain) of tide level at Dili Port (East Timor) where locates near equator (8.55° S, 125.56° E), over 3-month period continuously. The frequency spectrum, as expected, shows famous 1/*f* character with the two special peaks which are related to the motions of the moon and the sun.

Interestingly, the FS spectra have a similar nature of *dielectric relaxation* in which electric polarization is discussed in terms of dynamics of electric charges. Water *level* and *volume* may correspond to electric *potential* and *charge,* respectively. This equivalency may cast a new insight for the 1/*f* noise. It is also reported that the histogram of the tide level observed in time domain is approximated to be the Gaussian or the Weibull distribution function.

2. Measurement System and Analysis

Figure 1 shows the measurement system. The first and second diagram are ultrasonic and control circuit. This method is used to measure reflection between transmitting and receiving pulses of the ultrasonic wave. This transmitting to the object and receiving pulse from the object are controlled by control circuit.

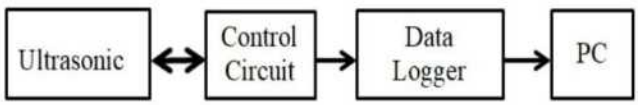

Fig. 1 Block diagram of the measurement system.

Fig. 2 Equipment installation: Dili port and control room.

The output pulse of control circuit is converted and transferred to the Data Logger (DL). The DL performs the arithmetic processing of several signals from sensors which observe water level. Data of the tide level at every 1 minute are stored in the built-in memory and SD card. The host device communication is output to the personal computer on which "data processing software" is installed by RS-232C. Collected data with the DL are Fourier transformed (Fast Fourier Transform: FFT), which will be briefly stated as follows.

Fourier analysis converts a signal from its original time domain to a representation in the frequency domain and vice versa [7]. The FT of a time-dependent function $f(t)$ is given by

$$F(f) = \int_{-\infty}^{\infty} f(t)e^{-i2\pi ft}dt\,, \qquad (1)$$

where $F(f)$ is the Fourier spectrum and f is the frequency (s^{-1}) [8].

FFT is an algorithm that computes the discrete $F(f)$ [9]. A limited number N (= 2^n) of discrete data, where n is an integer, should be required to perform the FFT. The time interval of the data Δt is therefore given by t_p/N, where t_p is the period of measurement time. In this paper we take N = 4096 (n = 12) in the EXCEL. The frequency interval Δf is given as

$$\Delta f = \frac{1}{N\Delta t}\,. \qquad (2)$$

The detail of the FFT is given elsewhere.

3. Results and Discussion

The sampled tide level data at Dili Port (Timor Leste) were obtained for the period from May 2018 to September 2018. In this paper, we discuss four data sets; one is sampled every 40 minnutes (#1: 114 - monitoring days) and others are every 10 minutes (#2-#5 for each 28 days). Figure 3 (a) shows the time-dependent tide level for the case #1 with second-time sale (time domain). The FFT result is shown in Fig. 3 (b). This is called the Fourier spectrum; the absolute value $|F(f)|$. One observes a decrease

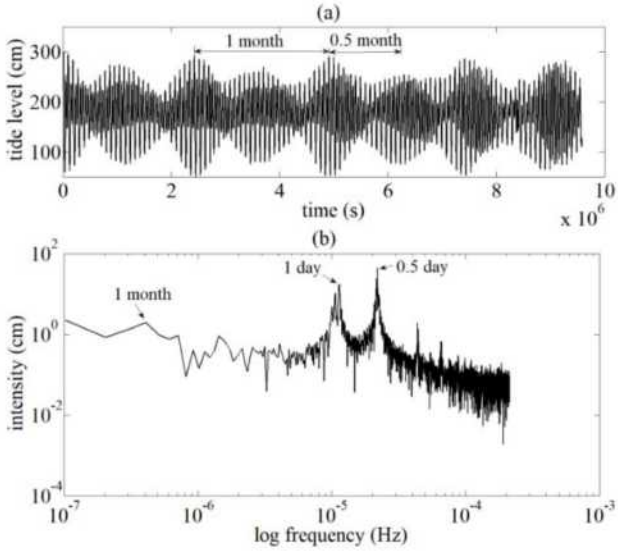

Fig. 3 a) Tide level at every 40 minutes in time domain, and b) frequency spectrum $|F(f)|$.

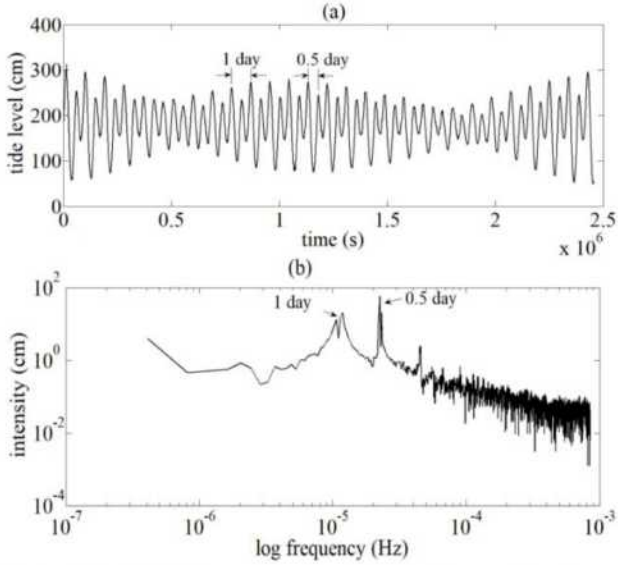

Fig. 4 a) Tide level at every 10 minutes in time domain, and b) frequency spectrum.

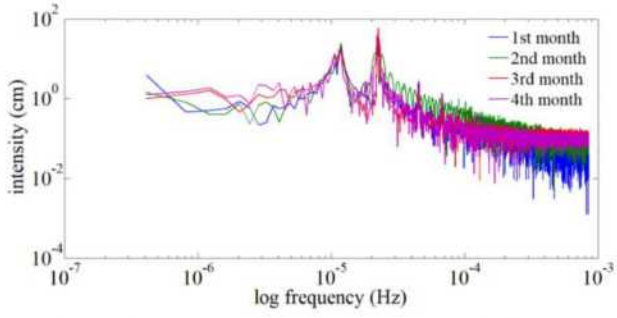

Fig. 5 Frequency spectrum at every 28 days for #2-#5 during around four months.

of the intensity with increasing frequency *f*, which is approximately proportional to *1/f*. This type frequency-dependent behavior is called the $1/f$ noise or $1/f$ fluctuation [7]. At low frequencies, the spectrum shows a constant, which is often called a *low pass filter* [10,11]. As shown in Fig. 3 (b), we can see three peaks corresponding to 1 month, 1 day, and half day.

Figures 4 (a) and (b) show the time- and frequency-dependent tide level for the case #2 (first one month), respectively. Features are not much different from those from #1, while the time scale is different. Two peaks shown in Fig. 4 (b) correspond to 1 day and half day.

The frequency spectrum for each #2-#5 is shown in Fig. 5, where #2 is the first 28 days and #5 is the last 28 days. The frequency spectrum is almost the same for each 28 days, indicating that no special event occurs during around 4 months at Dili port.

Figures 6 (a), (b), and (c) show the real, imaginary and absolute value (same as Fig. 3 (b)) of $F(f)$, respectively. As stated in Section 1, we will discuss an equivalency between the tidal and dielectric natures. The $F(f)$ is thus compared with the prediction from the Debye-type relaxation. The solid lines show the predicted results from the Debye-type relaxation equation given by [12].

$$F(f) = \frac{A}{1+i2\pi f\tau} = \frac{A}{1+(2\pi f\tau)^2} - i\frac{A2\pi f\tau}{1+(2\pi f\tau)^2}, \qquad (3)$$

where A is a constant and τ is the relaxation time (s). Then the absolute spectrum is given by

$$|F(f)| = A\sqrt{\frac{1}{1+(2\pi f\tau)^2}}. \qquad (4)$$

Equation (4) predicts that $|F(f)| \sim A$ for $2\pi f\tau << 1$ and $|F(f)| \propto 1/f$ for $2\pi f\tau >> 1$. This is just a feature of $1/f$ fluctuation. Fitting to the tide level with taking $A = 0.3$ cm and $\tau = 8 \times 10^3$ s (~ 2 hours) is fairly good. The meaning of τ is "delay of response" and hence in the present case τ (~ 2 hours) can be the response time

(delay) to the moon, which is a reasonable value [13].

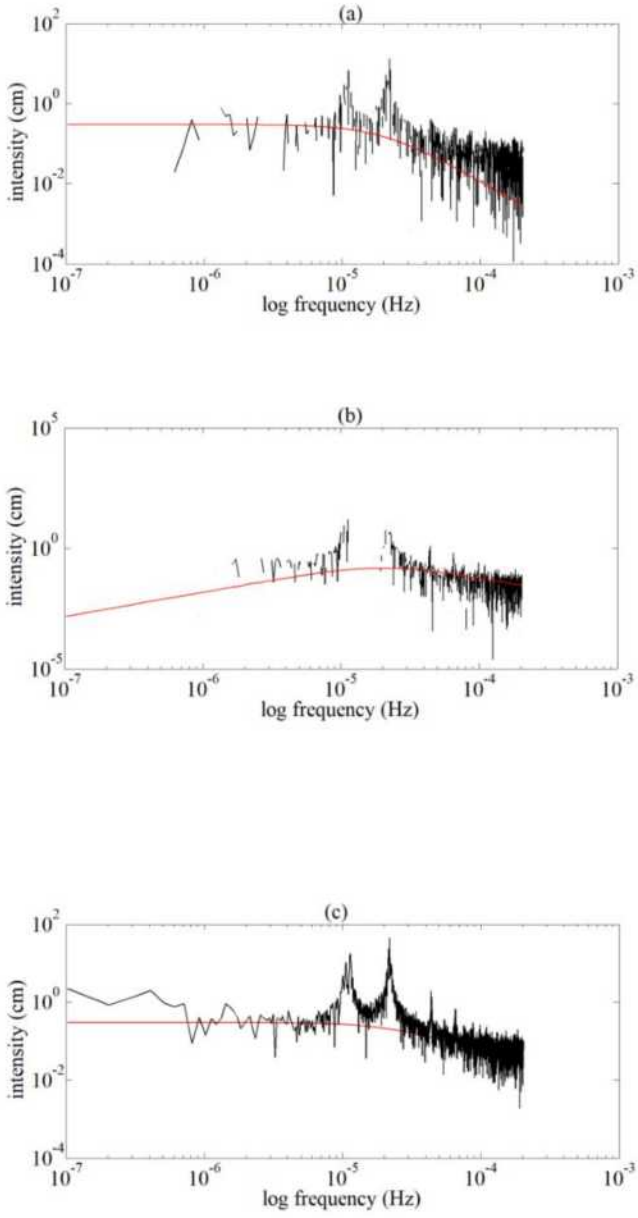

Fig. 6 (a) Real part of $F(f)$, (b) Imaginary part of $F(f)$, (c) Absolute value $|F(f)|$. Solid lines show the Debye-type relaxation function.

Let us discuss an equivalent electrical circuit which corresponds to the physics discussed above. As stated already, a feature of $F(f)$ looks like a low pass filter and hence the

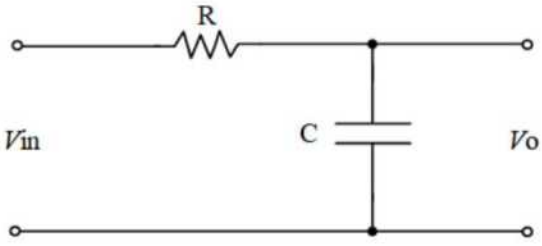

Fig. 7 Equivalent electrical circuit (low pass filter)

following RC electrical circuit, shown in Fig. 7, can be one of candidates, where R is the resistance and C is the capacitance. Note that V_i corresponds to the potential induced by the moon and/or the sun, and V_o to the tide level (potential) at any site. V_o is given by

$$V_o = \frac{\frac{1}{i2\pi fC}}{R+\frac{1}{i2\pi fC}} V_i = \frac{V_i}{1+i2\pi fCR} \tag{5}$$

Eq. (5) with $\tau = CR$ is equivalent to Eq. (3). Here, C and R, respectively, should correspond to "accumulation" and "resistance" for water flow. The phase difference θ between V_i and V_o in the sense of electrical circuit is given as

$$\theta = tan^{-1}\frac{1}{2\pi fCR}\,. \tag{6}$$

It should be noted that RL electrical circuit also gives the low pass filter [10]. We will discuss this point in a future paper.

A histogram approach to the tide level h, on the other hand, should be of interest to know the probability density at a particular level. For this purpose, the number of occurrences of each level is counted. Discrete bars shown in Figs. 8 (a) and (b) present the tide-level distribution for the total number of data ($N_T = 1.64 \times 10^5$). We try to find a proper probability density function, e.g., Gaussian or Weibull probability density, on the histogram.

A Gaussian probability density is given as [14]

$$G(h) = \frac{A}{\sqrt{2\pi\sigma^2}} exp\left\{-\frac{1}{2\sigma^2}(h - h_m)^2\right\}, \quad (7)$$

where A is a constant, σ is the standard deviation, and h and h_m are the tide level and its average, respectively. A Weibull distribution, on the other hand, is given as [14]

$$W(h) = \frac{kF_0}{F_p}\left(\frac{h}{F_p}\right)^{k-1} exp\left\{-\left(\frac{h}{F_p}\right)^{k}\right\}, \quad (8)$$

where F_0 is the shape parameter, F_p is the scale parameter of the distribution, and k is the failure rate [3,14]

Solid lines in Fig. 8 (a) show the probability density calculated from the Gaussian $G(h)$ ($A = 8.7 \times 10^5$, $\sigma = 55$, and $h_m = 178$) and the Weibull $W(h)$ ($F_0 = 8.5 \times 10^5$, $F_p = 195$, and $k = 3.8$) distributions, respectively. We cannot see any difference between $G(h)$ and $W(h)$ under these physical parameters.

More accurate comparison between the data and the probability distribution function should be given by integral form of the histogram and the probability density. This produces just the probability. Solid lines in Fig. 8 (b) show just probability calculated from the data (histogram) and the Gaussian distribution (red line) using the same parameters. The both curves fit well, suggesting that the histogram basically follows the Gaussian distribution.

4. Conclusion

The change in the tide level during 4 months in the time-domain at Dili port was discussed through the Fast Fourier Transform (FFT). The frequency spectrum showed the two special peaks induced by the gravitational motions of the moon and the sun.

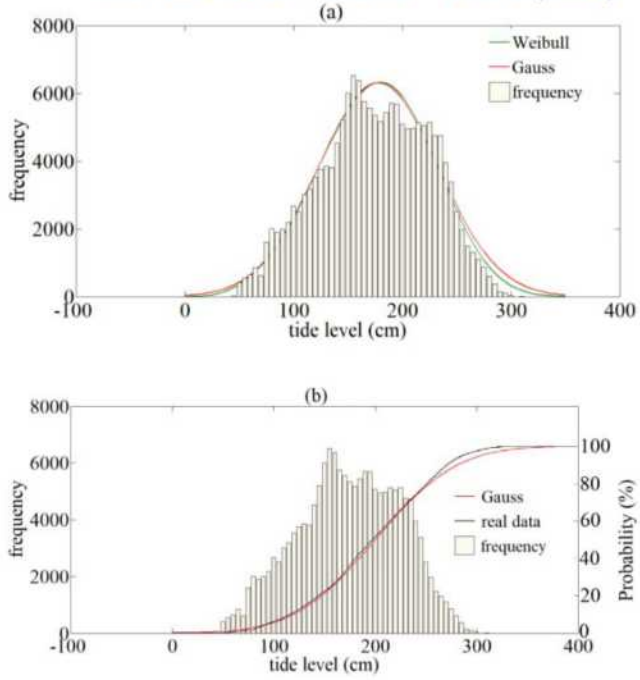

Fig. 8 (a) Tide-level distribution and the probability density for the Gaussian and the Weibull distribution, **(b)** Tide-level distribution and the probability for the Gaussian and the data (histogram).

So-called $1/f$ fluctuation (or noise) is found in higher frequencies and the overall behaviors can be identical with a type of low pass filter in the electrical circuit and was approximately replicated well by a RC electrical circuit. It was shown that the tidal level change was phenomenological analogous to a Debye-type relaxation found in dielectrics. This equivalency cast a new light for understanding the $1/f$ fluctuation being observed widely in nature which is a long-term mystery.

It was also found that the histogram of the tide level in time-domain was approximated to be the Gaussian or the Weibull distribution.

Acknowledgement

We would like to thank JICA CADEFEST 2 for financial support to the Faculty of Eng., Universidade Nacional Timor Lorosa'e.

References

[1] M. G. Kleinhans, M. Van Der Vegt, J. Leuven, L. Braat, and H. Markies, "Turning the tide : comparison of tidal flow by periodic sea level fluctuation and by periodic bed tilting in scaled landscape experiments of estuaries," pp. 731–756, 2017.

[2] M. Banno and Y. Kuriyama, "The characteristic of shoreline response to cyclic tidal change," *Dobuku Gakkai Ronbunshyu (in Japanese)*, vol. 68, pp. 576–580, 2012.

[3] G. B. F. Pietro Danilo Tomaselli, Carlo Lo Re, "Analysis of tide measurements in a Sicilian harbour," 2011.

[4] K. S. R. Murthy, "Estimation of Weibull Parameters using Graphical Method for Wind Energy Applications," 2014.

[5] E. Marone, F. Raicich, and R. Mosetti, "Harmonic tidal analysis methods on time and frequency domains: similarities and differences for the Gulf of Trieste, Italy and Paranguá Bay, Brazil."

[6] F. A.S, *Tides, Fundamentals, Analysis and Prediction*. São Paulo: IPT Press, 1997.

[7] S. Kogan, *Electronic noise and fluctuations in solids*, 2nd Editio. Cambridge: Cambridge University Press, 2008.

[8] A. Papoulis, *The Fourier integral and its applications*. Ney York: McGraw-Hill, 1962.

[9] A. E. Zonst, *Understanding the FFT*, 2nd editio. Titusville, Florida: Citrus Press, 2003.

[10] A. G. L. B. and G. T. H. Scott Draper , Thomas A. A. Adcock, "An electrical analogy for the Pentland Firth tidal stream power resource," 2014.

[11] J. Marcos, L. Marroyo, E. Lorenzo, D. Alvira, and E. Izco, "From irradiance to output power fluctuations : the pv plant as a low pass filter," 2011.

[12] S. O. Kasap, *Principles of Electronic materials and devices*, 3rd editio. New York: McGraw-Hill, 2006.

[13] K. Matsumoto, M. Ooe, T. Sato, and J. Segawa, "Ocean tide model obtained from TOPEX/POSEIDON altimetry data," *J. Geophys. Res. Atmos.*, vol. 1002 (C12), pp. 25319–29330, 1995.

[14] R. E. Walpole, R. H. Myers, S. L. Myers, and K. Ye, *Probability and statistics for engineers and scientists*, 9th editio. Prentice Hall.

Performance Analysis of a PV System at the Universidade Nasional Timor Lorosa´e

José Maria Xavier

Department of Mechanical Engineering, Faculty of Engineering, science and Technology, Universidade Nasionál Timor Lorosa´e , Rua Hera, Dili Timor-Leste.

E-mail: js_xvr@yahoo.com

Abstract: This paper presents an evaluation of the operating performance of Photovoltaic (PV) Grid-connected System installed in the Faculty of Engineering, Science, and Technology (FEST), the Universidade Nasional Timor Lorosa'e (UNTL) in Timor-Leste. The results of the performance evaluation of the energy installation during 2015 to 2016 is presented. Climatic data and energy output were collected and analyzed. The monthly average and annual performance parameters including energy generated, final yield, capacity factor, and the performance ratio of the system are calculated. The capacity factor and the performance ratio of the assessed systems also compared to other PV grid-connected system installed in other countries.

Keywords: Photovoltaic, Final yield, Capacity factor, Performance ratio

1. Introduction

Eelectricity became one of the most useful energy in our life. Increasing electricity demand led to the increase of the power generating capacity. Power generating based in fossil fuels is still dominant in the development of power plants, causing an environmental problem such as CO_2 emissions. Thus, it is necessary to increase the use of renewable energy in the development of power generation system [1].

Power generation in Timor-Leste is highly depends on diesel fuels. It is comprised of two main power plants, namely Hera Power Plant (HPP) and Betano Power Plant (BPP). The capacity of HPP and BPP are 120 MW and 130 MW, respectively. The national transmission grid is 150 kVA and has been connected throughout the country through ten substations to power community houses. Although the electricity is available for 24 hours across the country, the government has set its renewable energy policy to encourage the integration of renewable energy sources such as solar energy, wind energy and hydro power to the network, to reduce its energetic dependency and minimize fossil fuels imports [2].

There were some renewable electricity projects that had been implemented in the scope of an incentive program named Introduction of Clean Energy by Solar Electricity Generation System project.

Within this project, a micro solar PV grid-connected system with a capacity of 250 kW was built in 2014. This system is located in the

Faculty of Engineering, Science, and Technology (FEST) of the Universidade Nacional Timor Lorosa'e (UNTL) campus [3].

In order to support the investor expectation regarding system performance, the performance evaluation under factual climate condition is important. The performance analysis with real data can allow the discovery of possible system operational malfunction, facilitate the evaluation of systems that can be differ with regard to design, and evaluate the interaction of the installed system with main distribution grid.

In the literatures, several researches investigated the performance of grid-connected PV systems. Kumar et al. [4] carried out a study on a roof top 20 kWp PV grid connected system in a manufacturing industry in India. In this study, the operational behavior, economic calculation, and some significant features of the installation were emphasized. Moreover, important aspects of PV plant installation such as the viability of locality in terms of geographical data, solar panel inclination design and interfacing aspects of PV system with network were also discussed. The detail of the outcomes obtained from the study such as monthly energy generation, maintenance aspects, performance ratio, capacity factor, economic scrutiny of the system were also elaborated.

Kumar and Shudakar [5] carried out a performance study of a 10 MWp grid connected solar photovoltaic power plant installed at Ramagundam, India. In this study, solar PV plant design aspects along with its annual performance were developed. Various systems loss the power due to temperature, internal network, inverter and ohmic wiring. Apart from these losses, the system performance ratio and the energy final yield were also calculated. The performance results were then compared with the simulated values attained from the PV SYST and PV-GIS software.

Similar study was carried out by Attari et al. [6] on a 5 kWp PV grid-connected system installed in Tangier of Morocco. The system was installed in top of a government building and made up of 20 modules of 250 Wp. The experimental data during the periods of 2015 was recorded based on the real time surveillance. In this study, energy output of the system, final yield, modules temperature, plant efficiency, and system performance ratio were assessed. Various power losses were also investigated.

Shukla et al. [7] showed the simulated performance of a 110 kWp solar rooftop photovoltaic plant connected to distribution network for a residential hostel building at Manit, India. The authors analyzed the viability of solar PV system at the given location. In this study, four types of modules were used in the simulation to examine system performance ratio and energy yield. In addition, the Solar GIS PV Planner software was used to evaluate the performance of the system. Global in-plane radiation, shading effects, angular reflection at the surface of the arrays, system losses, and power conditioner performance were evaluated.

Allouhi et al. [8] investigated the performance analysis, economic and environmental evaluation of two 2 kWp solar power plant installed in High School of Technology of Meknes, Morocco. In this study, poly-Si module and mono-Si module were used, and the simulations were carried out using PVSYST software. The meteorological data for the site were taken from METEONORM database. System capacity factor, final yield, and system efficiency for both installed technologies were calculated.

Kumar et al. [9] analyzed a simulated performance of a 100 kWp Si-poly PV grid-

connected system. The authors simulated the proposed system to evaluate the feasibility of installing that system in an educational institute. The simulated system consists of 323 Si-poly modules of 310 Wp. All modules were arranged in 17 strings and each string was made up of 19 modules connected in series. Four solar inverters of 20 kW were used to connect the system to the main network through a utility meter. The PV SYST V6.52 software was used in the simulation. The effective energy output, energy supplied to the grid, and performance ratio of the system were evaluated. In addition, the system losses were also processed.

In this paper, the performance of the system at the FEST, Hera campus, for the average year 2015 to 2016 are analyzed. The parameters used in the performance assessed systems including reference yield, array yield, final yield, capture losses, system losses, capacity ratio and performance ratio. The data used are based on hourly, daily and monthly values.

2. PV Grid-Connected System

2.1 System Description

The PV system was installed at the FEST of UNTL in Dili, Timor-Leste. The latitude and longitude of the site are $8^0$33.1'S and $125^0$39.6E, respectively. The system, as shown in Fig. 1 consists of 1200 PV panels, polycrystalline silicon, of 215 W arranged in 12 series-connected modules with an overall capacity of 250 kW, covering a total surface area of about 1782 m^2 and mounted with the inclination of 10 degrees toward the North.

The system is connected to two 100 kW SUNUP inverters of P83BR104R model, and one 50 kW of PMC 500 model. A 350-kVA transformer is used to distribute electricity to the commercial grid and Faculty buildings. Technical specifications of the PV module are given in Table 1 [10].

Figure 1. PV grid-connected system in FEST-UNTL.

2.2 PV System Analysis

The performance parameters used in this study are the ones developed by International Energy Agency (IEA). The parameters were developed for analyzing the performance of grid-connected PV system. There are several parameters used to define the overall system performance regarding the energy production, solar resource, overall system losses, performance ratio, and capacity factor. For this study, some derived parameters related to energy and performance are calculated using the monitoring data recorded.

a. Reference Yield

The reference yield (Y_R) is the ratio of the incident energy in the array plane H_I to the array reference irradiance G_O. The total daily in plane irradiation is in units of kWh/(m^2.day) and reference irradiation is equal to one kilowatt per square meter. So, the reference yield is in unit of kWh/kW/day or in hours per day. It expresses an equivalent number of hours per day during which the solar radiation would necessary to be at reference irradiance levels in order to contribute with the same incidence energy as was monitored.

Table 1. Technical data of PV module Kyocera KD215GH-2PB

Electrical data	
Maximum power, Pmax	215 W
Maximum power voltage, Vpm	26.6 V
Maximum power current, Ipm	8.09 A
Open circuit voltage, Voc	33.2 V
Short circuit current, Isc	8.78 A
Maximum system voltage	1000 V
Module efficiency	14.4%
Limitting reverse current (series fuse rating)	15 A
Reduction of efficiency (from 1000 W/m^2 to 20 W/m^2)	6.0%
Nominal Operating Cell Temperature,NOCT	**45_degree C**
Temperature properties: Temperature coefficient	
V_OC [V/°C](V_OC [%/°C])	-1.2*10^-1*(-0.36)
I_SC [A/°C](I_SC [%/°C])	5.27*10^3(6.0*10^-2)
P_max [W/°C](P_max [%/°C])	-9.91*10^-1(-0.46)
Standard Test Condition (STC)	**Cell temperature 25 C**
	Spectrum AM 1.5; Irradiance level 1 kW/m^2

It can be calculated using the following equation [9]:

$$\boldsymbol{Y_R = \frac{H_I}{G_O}} \quad (1)$$

Where H_I is the incident energy in the array plane (kWh/m^2/day) and G_O is the array reference irradiance (1 kW/m^2).

b. Final Yield

The final yield (Y_F) of a PV system for a given period represents the net AC energy output divided by the rated power of the installed PV array at standard test condition

(STC) of 1000 W/m^2 solar radiation and 25 ^{0}C cell temperature. It indicates the number of hours of operation of the array required per day at its rated capacity to equal its monitored contribution to the daily useful energy. It can be written as [5]:

$$\boldsymbol{Y_F = \frac{E_{AC}}{P_{maxG,STC}}} \quad (2)$$

Where E_{AC} is the energy produced by the PV system (kWh) and $P_{maxG,STC}$ is the PV array rated power at standard condition test (STC) (kW).

c. System Losses

The system losses (L_S) are the ratio of energy injected to the grid to the nominal array power mentioned in the name plat of the PV array specifications. It can also be defined as the difference between the array yield (Y_A) and the final yield. This can be expressed by the following equation [6]:

$$\boldsymbol{L_S = Y_A - Y_F} \quad (3)$$

d. Annual Capacity Factor

Annual Capacity factor (CF_A) is defined as the ratio of the real annual energy output from the plant to the amount of energy the system would produce if it worked at full rated power for 24 h/day for a year (365 days). The *CF* has a direct implication on the cost of electricity production. The annual value of the *CF* is calculated by taking cumulative sum of useful

energy values at one-hour intervals using monitoring data recorded. It can be expresses as [8]:

$$CF_A = \frac{E_{AC,Year}}{(P_o * 24 * 365)} \quad (4)$$

Where $E_{AC,Year}$ is the annual energy produced by the PV system (kWh) and P_O is the rated power output of the installed array (kW).

e. Performance Ratio

The performance ratio (*PR*) is an indicator that normalizes the energy supplied to the grid with respect to nominal power mentioned in the specification of the PV array. Also, it indicates the overall effect of losses on a PV array´s normal output power. Its values indicate how close a PV system approaches ideal performance under actual operating circumstances. The *PR* is equal to the final yield divided by the reference yield. It can be formulated as [9]:

$$PR = \frac{Y_f}{Y_r} \quad (5)$$

Where Y_f is the final yield of a PV system (kWh/(kWp.d)) and Y_r is the reference yield (kWh/(kWp.d)).

The PR of a plant is independent of the location and is an important parameter which is frequently used to compare systems in different location and sizes. For a grid-connected system, PR around 0.8 – 0.85 is desirable because a high PR values indicates a high economic benefit. If the PR is less than 75% then reason for likely cause must be investigated and correspondingly addressed [11].

3. Result and Discussion

In this section, data from a 250 kW PV grid connected system located in FEST building are analysed based on meteorological data collected from the monitoring system from the site and performance parameters for an average of two years periods, from January 2015 to December 2016. The monitoring system record the data on hourly, daily and monthly basis which constitute the basis of this evaluation.

Solar radiation data are one of the most important input for an assessment of energy yield. Figure 2 shows the monthly averaged solar radiation and ambient temperature over the daytime hours. The highest value of solar radiation was in August with 191.4 kWh/m^2 and the lowest in February was 127.4 kWh/m^2. The ambient temperature ranged between a minimum of 24.5 ^{o}C, in August, and a maximum of 29 ^{o}C in November. The annual average of solar radiation and ambient temperature were about 163 kWh/m^2 and 26 ^{o}C, respectively. This lower solar radiation values reduce energy out-put of the PV modules. High ambient temperature increases PV cells temperature higher than 25^{0}C. This higher cell temperature will lower voltage open circuit (*Voc*) of the PV modules. These lower PV modules out-put and *Voc* values would reduce the energy yield by the PV system.

The average diurnal energy consumption of the FEST and energy generation of the PV system are presented in Figure 3. This trend represents the daily energy production and consumption for 24 hour per day per year. The average daily maximum energy consumption was just about 56 kWh which occurred during the mid-day time. The minimum load consumption happened early in the afternoon and remained almost constant throughout the night until early in the morning; it accounted for around 7 kWh on average. The daily maximum and minimum energy generated by the PV system were 128 and 14 kWh, respectively.

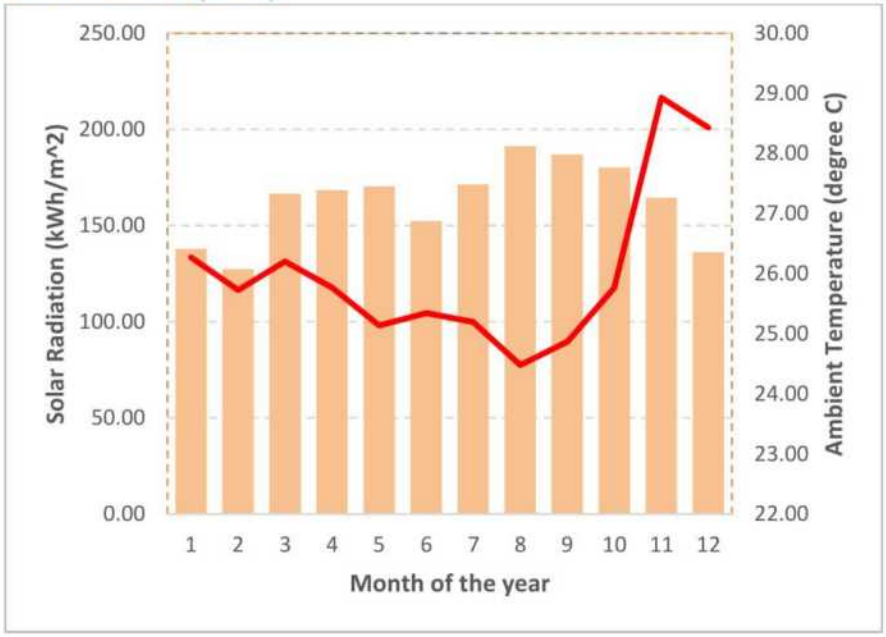

Figure 2. Solar radiation and ambient temperature values of the site.

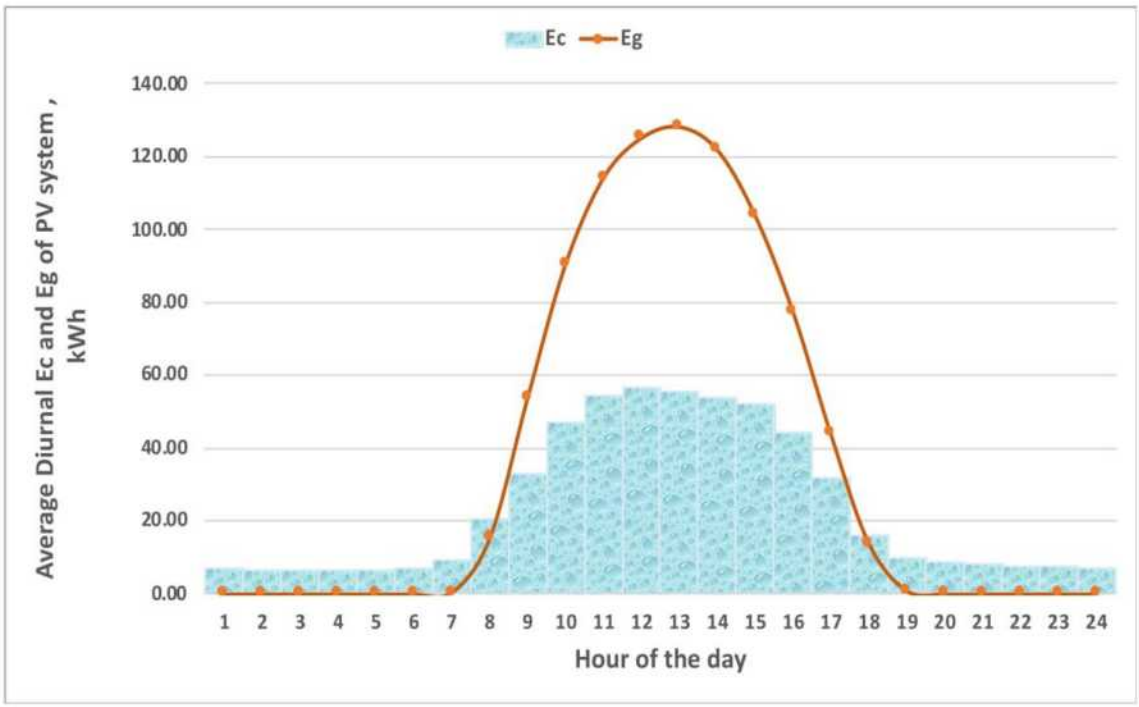

Figure 3. Diurnal energy consumption of FEST and energy generated by the PV system.

Monthly average daily PV system´s energy generated, energy supply to the grid, reference yield, final yield, array yield, and total system losses over the studied period are presented in Table 2. The monthly energy generated was varied between 643 kWh in December and 1166 kWh in September, the monthly energy supply to the grid was started from 329 kWh in December to 601 kWh in September. The average energy produced and supplied to the grid by the PV system were 889 kWh and 445 kWh, respectively. The monthly average daily reference yield was ranged from 4.4 in December to 6.2 kWh/kWp/day in September.

The final yield was high for September, accounted for about 4.5 kWh/kWp/day and was less for December, accounted for around 2.5 kWh/kWp/day. The array yield was varied between 4.5 kWh/kWp/day in December and 6.4 kWh/kWp/day in September. The energy yields values detected that for the month of December are less due to low solar radiation levels and can be soiling losses because of the dust cover during the summer period. The system losses (Ls) was ranged from 1.4 kWh/kWp/day in January to 2.6 kWh/kWp/day in July. As can be observed that system losses (Ls) were higher from May to August. These losses were due to the temperatures reached by the inverter were higher which is overheating the inverters thus unnecessarily reduce its efficiency [12].

Table 2. Main results of 250 kWp Si-poly PV system.

Month	Metrological parameters		Energy yields and system losses					
	Er, (kWh/m^2/day)	Ta, degree C	Energy generated, E_ac, kWh	Eenergy supply to grid, Eg, kWh	Yr, kWh/(kWp.d)	Yf, kWh/(kWp.d)	Ya, kWh/(kWp.d)	Ls, kWh/(kWp.d)
Jan	4.45	27.33	824.66	443.43	4.45	3.20	4.57	1.37
Feb	4.55	26.39	743.93	367.55	4.55	2.88	4.67	1.79
Mar	5.38	27.02	1053.41	503.73	5.38	4.08	5.52	1.44
Apr	5.62	26.32	943.56	454.91	5.62	3.66	5.76	2.11
May	5.50	26.12	794.94	378.45	5.50	3.08	5.64	2.56
Jun	5.08	25.76	734.49	332.68	5.08	2.85	5.21	2.37
Jul	5.53	25.46	788.14	404.84	5.53	3.05	5.67	2.62
Aug	6.17	25.18	1027.26	553.00	6.17	3.98	6.34	2.35
Sep	6.23	25.91	1166.13	601.69	6.23	4.52	6.40	1.88
Oct	5.81	26.65	1060.77	549.77	5.81	4.11	5.97	1.85
Nov	5.48	28.65	893.87	420.91	5.48	3.46	5.63	2.16
Dec	4.39	28.01	643.33	329.10	4.39	2.49	4.51	2.01
Average	**5.35**	**26.57**	**889.54**	**445.00**	**5.35**	**3.45**	**5.49**	**2.04**

The performance ratio (PR) and Capacity factor (CF) are calculated and presented in Fig. 4. The monthly averaged CF was ranged from 10.7% in December to 19.4% in September. The study results indicate that monthly *CF* values varied from month to month. These values variation was due to the system losses as a result of local climate conditions. The *CF* values of others similar studies shows that, according to Kumar and Sudhakar [5], a *CF* value varied from 12.7% to 20.0% based on one-year operation. Overall *CF* for the Indian PV plants varied from 12.3 to 18.8%. Attari et al. [6] conducted a performance investigation on a PV grid-connected system in Morocco and found the annual *CF* of the system to be 14.8%. There were also studies conducted by Makrides et al. [13] on performance assessment of a fixed PV system, found the *CF* annual average value to be 19.4%. Other studies conducted by Gottschalg et al. [14] found *CF* values between 20.8% and 26.0% for south-facing fixed and dual-axis tracking PV systems in Cyprus, respectively. To the knowledge of the author, there were no previous documentation or studies of *CF* for a fixed PV system in Timor-Leste. However, it can be deducted that *CF* value higher than 8.9% and less than 19.7% is a reasonable for a fixed PV system. The annual average *CF* value obtained in this study was 14.8%.

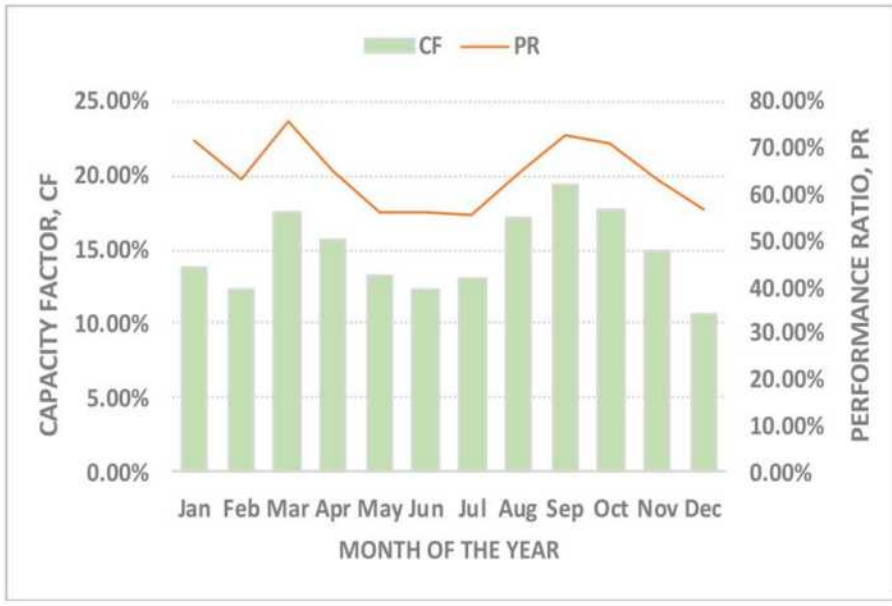

Figure 4. Monthly averaged Capacity Factor and Performance Ration of PV system.

It is noticeable, from Figure 4, that system PRs varies from 56.0%, in May, to 76.0% in March. The annual average PR was about 64.5% clearly indicating not an efficient performing system. This lower PR value was due to lower energy output from the system. Lower inverter efficiency can be the main cause that led to a low system performance. In order to perform further improvement of system performance, an advance technical investigation to systems components, such a case of inverter, must be conducted. The PR is used for comparing PV systems situated in different locations because of its ability to capture the actual insolation better and is independent of the plant size and location [11]. The average *PR* of other observed PV plant varied from country to country with an average value ranging from 49% up to 98%. A similar study conducted in Ghana found the PR ranges between 49% and 71% [15]; India, 80% [9]; in Serbia found the system *PR* was about 94% [16]. In the similar study conducted in Morocco found the *PR* values was ranged from 58% to 98% [6], this trend shows the highest PR value among other observed countries.

4. Conclusions

An analysis of the first PV grid-connected system project in Timor-Leste was carried out in order to observe systems characteristics behavior under specific climatic conditions. From the nominal installed power, the performance of the system has been evaluated. The following conclusions were drawn from the study:

1) From the author´s analysis, the performance of the PV system is considered not efficient. This conclusion is drawn in terms of the PR criteria pointed out early in Section 2.2.
2) Average annual PV energy output is 890 kWh. The months of August, September and October are the period where the PV system was the most efficient.
3) Average annual capacity factor is 14.8%. This value can be defined as the period of

time during a year when the PV system is producing energy at its full power output.

4) The average annual performance ratio is 65%. The maximum value can reach 76%. These values indicate the system performance under factual operating conditions, which should be considered inefficient.

Acknowledgement

The Author wishes to thank the member of PV groups in UNTL for permission of using PV data collected in UNTL, Hera campus. The PV system was given by JICA.

References:

[1] F. Blaabjerg, R. Teodorescu, M. Liserre and V. T. Adrian, "Overview of control and grid synchronization for distributed power generation system," IEEE Transaction on Industrial Electronics, vol. 53, no. 5, pp. 1398-1409, 2006.

[2] UNDP, "Promoting Sustainable Bioenergy Production from Biomass in Timor-Leste," United Nations Development Program, Timor-Leste, 2014.

[3] M. o. Education, "Introduction of Clean Energy by Solar Electricity Generation System Project," Ministery of Education, Dili, Timor-Leste, 2014.

[4] A. Kumar, K. Sundareswaran and P. Venkateswaran, "Performance study on a grid conected 20 kWp solar photovolatiac installation in an industry in Tiruchirappalli," Energy and Sustainable Development, vol. 23, no. 2014, pp. 294-304, 2014.

[5] S. Kumar and K. Shudakar, "Performance evaluation of 10 MW grid connected solar photovoltaic power plant in India," Energy Report, vol. I, no. 2015, pp. 184-192, 2015.

[6] K. Attari, A. Elyaakoub and A. Asselman, "Performance analysis and investigation of a grid connected photovoltaic installation in Morocco," Energy Report, vol. 2, no. 2016, pp. 261-266, 2016.

[7] A. Shukla, K. Shudakar and P. Baredar, "Simulation and performance analysis of 110 kWp grid-connected photovoltaic system for a residential building in India," Energy Report, vol. 2, no. 2016, pp. 82-88, 2016.

[8] A. Allouhi, R. Saadani, T. Kousksou, R. Saidur, M. A. Jamil and Rahmoune, "Grid-connected PV system installed on institutional buildings: technology comparison, energy analysis and economic performnace," Energy and Buildings, vol. 130, no. 2016, pp. 188-201, 2016.

[9] N. Kumar, M. Kumar, P. Rejoice and M. Mathew, "Performance analysis of 100 kWp grid-connected Si-poly photovoltaic system using PV syst simulation tool," Energy Procedia, vol. 117, no. 2017, pp. 180-189, 2017.

[10] FEST, Office of Faculty of Engineering, Science, and Technology, 2018.

[11] A. Khalid, I. Mitra, W. Warmuth and V. Schacht, "Performance Ratio - Crtial parameter for grid connected PV plants," Renewable and Sustainable Energy Reviews, vol. 65, no. 2016, pp. 1139-1158, 2016.

[12] F. Cherfa, A. Hadj, R. Oussaid, K. Abdeladim and S. Bouchakour, "Performance Analysis of the Mini-Grid Connected Photovoltaic System at

Algiers," Energy Procedia, vol. 83, no. 2015, pp. 226-236, 2015.

[13] G. Makrides, B. Zinsser, M. Norton, G. Georgiou, M. Schubert and J. Werner, "Performance assessment of different photovoltaic system under identical field conditions of high irradiance," in Science Application and Technology Conference, Edinburgh, UK, 2007.

[14] R. Gottschalg, T. Betts, S. Williams, D. Sauter, D. Infield and M. Kearney, "The effect of spectral variations on the performance parameters of single and double junction amorphous silicon solar cells," Solar Energy Material and Solar Cells, vol. 85, no. 2005, pp. 415-428, 2005.

[15] D. Quansah, M. Adaramola, G. Appiah and A. Isaac, "Performance analysis of different grid-connected solar photovoltaic (PV) system technologies with combined capacity of 20 kW located in humid tropical climate," International Journal of Hydrogen Energy, vol. 41, no. 2017, pp. 4626-4636, 2017.

[16] D. Milosavljevic, T. Pavlovic and D. Pirsl, "Performance analysis of a grid-connected solar PV plant in Nis, Republic of Serbia," Renewable and Sustainable Energy Reviews, vol. 44, no. 2015, pp. 423-435, 2015.

Technical Review on Biomass Resource for Wood Pellets in Timor-Leste

Lelis Gonzaga Fraga[a,b] José Carlos F. Teixeira[a] and Manuel Eduardo C. Ferreira[a]

[a] *Department of Mechanical Engineering, University of Minho, Portugal*

[b] *Department of Mechanical Engineering, Universidade Nacional Timor Lorosa'e, Rua Cidade de Lisboa, Dili Timor Leste*

E-Mail: lelisfraga@hotmail.com

Abstract: Wood pellets become an interesting biomass fuel to support energy demand. Development of a pellet market can create several benefits to the country, due to its contribution to the environment, energy sustainability, and social economy. Timor-Leste has biomass resources from the forest, agriculture, and waste, where the biomass resources were mostly used for cooking purpose. This paper presents the technical review on the wood pellets resource for the heating purpose in the household and/or industries.

Keywords: renewable energy, biomass resources, wood pellets

1. Introduction

Wood pellet is becoming an interesting biomass fuel to produce heat source in a boiler or furnace. The demand for wood pellets is predicted to be increased continuously [1]. In Korea, for example, the utilization of wood pellets have been developed over a decade and supported by government subsidies based on the standard regulation in 2011 [2]. Korea government has established some policies to increase new and renewable energy portion up to 6 % by 2020. These policies include a domestic wood pellet boiler supply policy. The benefit of using wood pellets is indicated by its high energy density, reduced transportation, and storage cost [3,4], the lower amount of indirect greenhouse gas emissions from its production and transportation comparing fossil fuel [4] and emissions nearly CO_2 neutral [5].

The combustion of wood pellets has minor gas emission in automatically fed appliances than manually fed systems using firewood [6]. The emission produced from wood pellets of different quality present significantly different values [7,8]. Arranz et al. [9] have investigated two commercial pellets from fruit tree pruning and pine wood pellets burning in a domestic pellet stove, showing that compared to fruit pruning, pine wood pellets showed better characteristics for their domestic use in small-sized stoves. This indicates their lower ash percentage and higher high heating value.

Meanwhile, pellets from pine, industrial wood wastes, and peach stones were combusted in a domestic boiler fired to evaluate their combustion and emission characteristics [10]. This study revealed that the type of pellets affects significantly the boiler emission

characteristics, and amongst those pellets, the pine pellets show better performances.

Wood pellets can be burned individually (100 %) or mixed with other fuel (co-combustion) such as coal [11], peat [12], and solid waste [13]. Mylläri et al. [14] investigated the co-combustion of coal and wood pellets in a large pulverized fuel-fired power plant boiler and revealed that the pellet addition lowered the total particle number concentrations in comparison to the coal combustion. The co-firing of peat with wood also decreased significantly fine particle (PM1) emissions [12]. Nevertheless, Ferreira et al. [13] stated that the co-combustion of wood pellets with industrial waste such as shoemaking residues, textiles, and plastics do not meet the legal concentration limits for CO.

Nowadays Timor-Leste is mostly imported energy sources to meet their energy requirements for transportation and power generation. To provide electricity in the country, two main power stations have been installed in Betano (Manufahi district) and Hera (Dili district) with the capacity of 137 and 120 MW respectively [15]. The power source is fuel oil which causes air pollution. Meanwhile, in Oecussi district 17 MW of diesel base power plant was completed in 2015 [16]. In the purpose of supporting the energy consumption in the country, the development of a renewable energy source is an important factor.

This paper presents a technical review of wood pellets as an energy source for heating purposes in the household and/or industries. The co-combustion of wood pellets is also presented. In addition, the potential for developing wood biomass use in Timor-Leste is also presented.

2. Results and Discussion

2.1 Application of Wood Pellets

Wood pellets are cylindrical shape produced from sawdust and wood shavings, which are mostly made from compressed material [17,18] with a higher high heating value which produced low emission to the environment [9]. Wood pellets are classified into several different classes. Class A (A1 and A2) are the high quality of wood pellets according to prEN 14961-2 which can be used for the domestic purpose [18]. Wood pellets are dry and have high energy content, easier to store and the convenient delivery or transport [19]. In addition, pellets are the ideal fuel for replacing heating oil or gas. As it is carbon neutral, then wood pellet is suitable biomass fuel in producing heat through the combustion process.

2.1.1. Pellets Combustion for Domestic Use

In converting the wood pellets into useful energy as for cooking or heating, the wood pellets are combusted in a pellet boiler or pellet stove. The combustion of wood pellets in a small scale pellet boiler or furnace for the domestic or household heating was investigated by many researchers [2,20]. Domestic wood pellet-fired boiler with a maximum thermal capacity of 22 kW was investigated by Rabaçal et al. [10]. The pellets from industrial wood wastes and peach stones used in this study show an attractive potential for use in domestic boilers. Orecchio et al. [21] investigated the different brand of wood pellets and burned in the stove operated at about 4 kW. This study revealed that there are very low risks for operators regarding non-carcinogenic and carcinogenic elements contained, regarding ashes produced during cleaning of pellet stoves in confined environments.

2.1.2. Power with Co-Combustion

The combustion of biomass with other fuels can have some advantages regarding cost, efficiency, and emissions [22]. Moreover, co-firing can reduce emissions of SO_X and NO_X and co-combustion of biomass reduces the CO_2 emissions. Co-combustion of unburned carbon 40% with lignite proved that will not deteriorate the behavior of the combustion including ignition behavior, flame stability, NOx and SO_2 emissions [23]. Adding a proper proportion of biomass with coal could enhance the ignition performance and thermal reactivity of coal [24].

In Europe, regarding the imported and co-fired pellets, these pellets are an attractive fuel for producing cost-effective renewable electricity and mitigating CO_2 emissions [25]. Two countries such as Germany and Austria consider it a competitive option to lower the production of CO_2 compared with other renewables. In Belgium, the Netherlands, and Great Britain are using the wood pellets mostly for co-incineration in coal-fired power plants [26]. Yousaf et al. [27] revealed that combustion of biochar fuels with coal increases combustion efficiency and improved the thermal characteristics compared to the coal and/or biomass-coal fuels. Note that biochar fuels are produced from peanut shell and wheat straw at 300, 500 and 700 °C.

2.1.3 Torrefaction

Torrefaction is the partial pyrolysis of wood carried out using a temperature between 220 – 320°C [28]. It is carried out under atmospheric conditions and in the absence of oxygen [29]. The product of torrefaction is in the solid phase and is referred to as the charred residue (char). Wood pellets from torrefaction have higher energy density compare to conventional wood pellets [28], and the heating value of torrefied spruce is higher than of raw spruce [30]. It is revealed that pellets obtained from torrefied sawdust have higher volumetric energy density than regular pellets, which is suitable for storage and long distance transportation compare to torrefaction pellets [31].

The benefit of pellet torrefaction is to reduce the CO_2-equivalent emissions from their transportation. Even though extreme torrefaction conditions need to be avoided as it maximizes the heating value, grindability, and hydrophobicity of wood, and also make the pelletisation process difficult, which will produce the pellets with inferior durability [28].

Different material shows different torrefaction behavior at the same temperature. Four biomass materials such as bamboo, willow, coconut shell, and wood were torrefied at a higher temperature. The results show that the influence of the torrefaction on bamboo and willow are superior to coconut shell and wood [32]. This behavior indicate that willow and bamboo can be classified into the relatively active species, while wood and coconut shell can be considered as the relatively inactive materials. This is indicated by the result of weight loss during torrefaction, where the weight of biomass remained in wood and coconut shell is higher than willow and bamboo respectively. Burning the torrefied biomass in a boiler can increase the efficiency of the boiler. Isemin et al. [33] show that, combustion of torrefied pellets made from coal sludge and straw mixture increases the boiler efficiency by 5%.

2.2 Resources for Pellets Production

The pellets are produced in plants composed of several production lines with individual capacities of approximately 100–200 ktons/a per line [26]. The resources for producing pellets are obtained from residues, by-products or waste

products both in agricultural and forestry and from agricultural cultivation for example plantation, miscanthus, and whole cereal plants. Moreover, any kind of woody biomass is possible to use as raw material for pelletisation, including sawdust, softwood, and hardwood [18]. Several types of chips, wood dust or cut wood pieces, are being used for producing wood pellets in central Europe.

2.2.1 Sawdust

Sawdust is obtained from the cutting processes and suitable for palletization [18]. The sawdust goes through grinding in a hammer mill before pelletizing for insuring homogeneity. Sawdust is considered as a better feedstock for pellet processing because it does not require any additional energy for grinding [34]. In the UK, the sawdust is produced either from a sawmilling operation or the manufacture of wooden structures [35].

2.2.2 Softwood and Hardwood

Softwood is commonly called coniferous, while hardwood is called deciduous. Softwoods typically have larger cells and longer cellulose fibers than hardwoods [36]. Hardwood is more difficult to process due to its higher density, which results in increased energy consumption of the pellet mill [18]. The rate where the hardwood and softwood release their energy can be different, the hardwood is much slower than softwood [19].

Based on the ash content, the softwood is usually better than hardwood, thus the hardwood would not meet the requirements of prEN 14961-2 for producing of pellets [18]. Softwood and hardwood show different behavior in terms of emissions. The emission of organic carbon (OC) produce from residential devices of softwood is higher than hardwood. The same condition for higher PAH (Polycyclic aromatic hydrocarbon) emissions in residential wood combustion [37].

2.3. Potential Development of Pellets Production

Wood pellets as a biomass feedstock which has several advantages including easier transport, affordable price, high energy density, low emissions, carbon neutral, and some more others [34,38]. In addition, producing the wood pellets under several conditions are needed to be identified including the potential of biomass resources, the production facility and energy demand and the government policy in developing the renewable energy resource [15,26,35]. There are several processes of manufacturing wood pellet such as storage, cleaning, drying, grinding, pelletizing (pressing), cooling, screening, and distribution [19]. Before the grinding process, the raw material is dried to have a water content in a suitable condition. The water content in the wood should not be more than 10 % [26,35], otherwise, it will be difficult to pelletize [35].

In 2013 it was indicated that the primary energy supplies are approximately 66 % from consumption of coal in China. However, in northern areas, the government implemented strict rules on coal control policies for heating buildings, and this might provide the opportunity to the large-scale development of wood pellets [34]. Thomson and Liddell [38] stated that in Europe countries, demand for wood pellet heating is rising, as the government support for renewable energy in combination with high fossil fuel prices and environmental concerns. In addition, the development of wood pellets will also create more job opportunity which contributes to the social and economic of the country.

Nowadays, some households in Europe countries have used this wood pellet from sawdust for about 1.4 tons of oil equivalent per dwelling [4]. In 2012, 27 countries of European Union countries consumed about 15.1 million tons of wood pellets, and almost six million tons used for residential heating [38].

2.4. Potential Use in Timor-Leste

Timor-Leste (TL) is a tropical country which has the potential of biomass resource in almost all of the territory. About 73 % of the territory is categorized as forest use and some of these area are in tropical monsoon forest [39]. The highest concentration of biomass plant is in upland areas, medium areas, and low forest density. These highest resources of biomass are available in the districts of Manatuto, Viqueque, Lautem, and Covalima with a capacity of between 90 – 160 tons/ha [15].

Various types of biomass resources from agriculture are available in TL such as tree trunks, branches, leaves, shoots, bark, pine cones, etc. based on the estimation, the amount biomass (stock) above-ground are 127,370, and 381 ton with an annual increment 5,213, and 645 tons/year and the usable biomass in the country are 4,901, and 483 tons/year [39]. The availability of the usable biomass in the country from agricultural and agroforestry correspond to 49.2 and 4,901.5 ktons/year, respectively. From the number of biomass identified in TL, it is shown that the potential of usable biomass energy including forestry and agriculture is 1.68 x 10^6 toe/year, animal waste is 4.81 x 10^3 toe/year, and urban solid waste is composed of 9.55 x 10^3 toe/year [15].

2.4.1 Review on Heating Needs

Timor-Leste has two seasons, wet (November - May) [40] and dry season (May - November) [41], but some parts of the country experience cold weather. The average temperature in some parts of the country is 18-25 ^oC. The cold weather mostly appears in the evening. Some places have an average low temperature at 3 ^oC [39], as this temperature needs the heating system. Several districts referred to this low temperature are, for example, Aileu, Ainaro, and Ermera districts.

For cooking purpose, the firewood is mostly consumed by most of the households in TL. About 93 % of households in TL use firewood, to use for their energy needs, which represents the consumption of 1.3 million m^3 or approximately 0.8 million tons. Increase of using the firewood for cooking will impact on the biomass resources. A very traditional method of cooking causes severe air pollution and health problem [15]. Several emissions produced from biomass combustion with the negative impact on health are presented in Table 1. Among those emissions, the CO and particle emissions are the two most widely targeted pollutants in the evaluation of stove performance [42].

Biomass from commercial Miscanthus straw (MS), softwood chips (SWC) and beech wood chips (BWC) were burned in a domestic-scale boiler (40 kW) and observed the emission factor on human health [43]. This study revealed that the particles emitted from biomass fuel combustion, causing the cytotoxic and genotoxic effects on the human lung. The study revealed that during the ignition and recycle period of a fireplace, a critical moment that could result in harm on the human health, for example, a respiratory problem as caused of smoke and a particle matters [44]. The emission result from the household was measured both indoor and outdoor sample to know the different concentration of each [42]. The different concentration of emission was measured such as

Table 1. The emission effect on the human health

Emissions	Health problem	References
Polycyclic aromatic hydrocarbons (PAHs)	Cell-damaging potential upon interaction with human lung cells, cardiopulmonary and lung cancer mortality, DNA damage.	[43].
Carbon monoxide (CO)	Related to the lungs, impairs the physical and mental abilities; affect fetal development.	[46].
Hydrocarbons (HC)	Irritation in the eyes, nose, and throat; Prolonged exposure may cause cancer.	[46].
Nitrogen oxides (NOx)	Respiratory and cardiovascular diseases.	[46].
Sulfur dioxide (SO_2)	Classified as slightly irritating to the respiratory system, leading cause of acid rain.	[46].
Particle matters	Cardiovascular and respiratory illnesses, skin diseases, increased blood pressure, etc.	[37].
Wood smoke	Health effects including eye, nose, and throat irritation, decrements in lung function, reduced resistance to infections and increased severity/incidences of acute asthma.	[37].
Aerosols	Atmospheric chemistry, radiative forcing, biogeochemical cycles, visibility, etc.	[37].

Total Suspended Particles and $PM_{2.5}$ from outdoor, and particle of <0.25 μm and 0.25-1.0 μm for indoor. In order to prevent indoor emissions, good ventilation is important to maintain good air quality.

2.4.2 Review on Forest Sources

Various types of biomass from agriculture are available in TL; some from forestry include tree trunks, branches, leaves, shoots, bark, pine cones, etc. [39]. Some biomass sources are from agriculture plantations such as coffee, rice fields, agricultural parcels with surrounding trees, meadows, etc., showing that the increment of forest biomass in the highlands, between 1,000 and 2,000 meters is about 30 % of the number of the actually produced.

Most part of the country is dominant by the small mountains and about 50 % of the total land area is forestry, which is equivalent to approximately 745,174 hectares [45]. The annual biomass production based on the precipitation of 500 mm is 4.2 tons/ha, with an average of more than 1,500 mm per year is about 10.8 tons/ha [39]. District Lautem, Manatuto, and Viqueque were identified as a potential area for the biomass development for energy utilization.

The forests in TL are important for a fuel source, where the average household uses for cooking up to 24 kg wood per day. Most of the households are used wood for cooking. The data

in 2015 show that 81 % of the households in TL are using wood for cooking, mostly for a rural area of about 92 % and urban area is 53 % [47]. All these life styles cause degradation of watershed and catchment areas, and loss of biodiversity and habitat [38]. The government of TL has developed a policy to perform an effective protect the ecological integrity and biological composition of the forestry area with not less than 70 % in 2020. With the goal of the forestry sector development is the sustainable management of forest resources and watersheds to provide environmental, social and economic benefits to the people of Timor-Leste [48].

3. Conclusions

Wood pellets become an interesting biomass fuel to support the energy requirements. Wood pellets have some advantages such as, easier transportation, affordable price, high energy density, low emissions, and carbon neutral [3-5,34,38]. Various methods can be applied to improve the wood pellets combustion efficiency such as co-combustion and torrefaction.

Timor-Leste has biomass resources from the forest, agriculture, and waste, where the biomass resources were mostly used for cooking purposes. In some areas where heating is needed, there is some potential for starting a pellet market. It was pointed out that several studies are needed to developing a steady market with respect to local conditions including economic, social, and environmental.

References

[1] J. Barrette, E. Thiffault, A. Achim, M. Junginger, D. Pothier, and L. De Grandpré, "A financial analysis of the potential of dead trees from the boreal forest of eastern Canada to serve as feedstock for wood pellet export," Appl. Energy, vol. 198, pp. 410–425, 2017.

[2] J. Ahn and J. H. Jang, "Combustion characteristics of a 16 step grate-firing wood pellet boiler," Renew. Energy, vol. 129, pp. 678–685, 2018.

[3] M. Mancini, A Rinnan, A. Pizzi, C. Mengarelli, G. Rossini, D. Duca, and G. Toscano, "Near infrared spectroscopy for the discrimination between different residues of the wood processing industry in the pellet sector," Fuel, vol. 217, pp. 650–655, 2018.

[4] B. Škrbić, V. Marinković, S. Spaić, V. Milanko, and S. Branovački, "Profiles of polycyclic aromatic hydrocarbons in smoke from combustion and thermal decomposition of poplar wood pellets and sawdust," Microchem. J., vol. 139, pp. 9–17, 2018.

[5] G. Schmidt, G. Trouvé, G. Leyssens, C. Schönnenbeck, P. Genevray, F. Cazier, D. Dewaele, C. Vandenbilcke, E. Faivre, Y. Denance, and C. Le Dreff-Lorimier, "Wood washing: Influence on gaseous and particulate emissions during wood combustion in a domestic pellet stove," Fuel Process. Technol., vol. 174, pp. 104–117, 2018.

[6] S. Ozgen, S. Caserini, S. Galante, M. Giugliano, E. Angelino, A. Marongiu, F. Hugony, G. Migliavacca, and C. Morreale, "Emission factors from small scale appliances burning wood and pellets," Atmos. Environ., vol. 94, pp. 144–153, 2014.

[7] V. K. Verma, S. Bram, I. Vandendael, P. Laha, a. Hubin, and J. De Ruyck, "Residential pellet boilers in Belgium: Standard laboratory and real life performance with respect to European

standard and quality labels," Appl. Energy, vol. 88, pp. 2628–2634, 2011.

[8] V. K. Verma, S. Bram, F. Delattin, and J. De Ruyck, "Real life performance of domestic pellet boiler technologies as a function of operational loads: A case study of Belgium," Appl. Energy, vol. 101, pp. 357–362, 2013.

[9] J. I. Arranz, M. T. Miranda, I. Montero, F. J. Sepúlveda, and C. V. Rojas, "Characterization and combustion behaviour of commercial and experimental wood pellets in South West Europe," Fuel, vol. 142, pp. 199–207, 2015.

[10] M. Rabaçal, U. Fernandes, and M. Costa, "Combustion and emission characteristics of a domestic boiler fired with pellets of pine, industrial wood wastes and peach stones," Renew. Energy, vol. 51, pp. 220–226, 2013.

[11] P. Xing, L. I. Darvell, J. M. Jones, L. Ma, M. Pourkashanian, and a. Williams, "Experimental and theoretical methods for evaluating ash properties of pine and El Cerrejon coal used in co-firing," Fuel, vol. 183, pp. 39–54, 2016.

[12] O. Sippula, H. Lamberg, J. Leskinen, J. Tissari, and J. Jokiniemi, "Emissions and ash behavior in a 500 kW pellet boiler operated with various blends of woody biomass and peat," Fuel, vol. 202, pp. 144–153, 2017.

[13] P. T. Ferreira, M. E. Ferreira, and J. C. Teixeira, "Analysis of Industrial Waste in Wood Pellets and Co-combustion Products," Waste and Biomass Valorization, vol. 5, pp. 637–650, 2014.

[14] F. Mylläri, P. Karjalainen, R. Taipale, P. Aalto, A. Häyrinen, J. Rautiainen, L. Pirjola, R. Hillamo, J. Keskinen, and T. Rönkkö, "Physical and chemical characteristics of flue-gas particles in a large pulverized fuel-fired power plant boiler during co-combustion of coal and wood pellets," Combust. Flame, vol. 176, pp. 554–566, 2017.

[15] L. Gonzaga Fraga, J. Carlos F. Teixeira, and M. Eduardo C. Ferreira, "The Potential of Renewable Energy in Timor-Leste: An Assessment for Biomass," Energies, vol. 12, pp. 1441, 2019.

[16] P. da Silva, "Electricity Industry Development in Timor-Leste," in Programa de Pós-Graduação e Pesquisa Unidade dos Produção e Dessiminação do conhecimento UNTL, 2016, vol. 4, pp. 16.

[17] European Biomass Association, "A Pellet Road Map for Europe," AEBIOM, pp. 1–11, 2008.

[18] I. Obernberger and G. Thek, "The pellet handbook: The production and thermal utilisation of biomass pellets", London: Earthscan, pp. 1–549, 2010.

[19] D. Jenkins, "Wood Pellet Heating Systems", London: Earthscan, pp. 1–126, 2010.

[20] F. Fachinger, F. Drewnick, R. Gieré, and S. Borrmann, "How the user can influence particulate emissions from residential wood and pellet stoves: Emission factors for different fuels and burning conditions," Atmos. Environ., vol. 158, pp. 216–226, 2017.

[21] S. Orecchio, D. Amorello, and S. Barreca, "II) Wood pellets for home heating can be considered environmentally friendly fuels? Heavy metals determination by inductively coupled plasma-optical emission spectrometry (ICP-OES) in their ashes and the health risk assessment for the operators," Microchem. J., vol. 127, pp. 178–183, 2016.

[22] T. Nussbaumer, "Biomass Combustion In Europe Overview On Technologies and Regulations," New York: NYSERDA, pp. 1-92, 2008.

[23] W. Rybak, W. Moroń, K. M. Czajka, A. M. Kisiela, W. Ferens, W. Jodkowski, and C. Andryjowicz, "Co-combustion of unburned carbon separated from lignite fly ash," Energy Procedia, vol. 120, pp. 197–205, 2017.

[24] C. Zhou, G. Liu, X. Wang, C. Qi, and Y. Hu, "Combustion characteristics and arsenic retention during co-combustion of agricultural biomass and bituminous coal," Bioresour. Technol., vol. 214, pp. 218–224, 2016.

[25] R. Ehrig and F. Behrendt, "Co-firing of imported wood pellets - An option to efficiently save CO_2 emissions in Europe?," Energy Policy, vol. 59, pp. 283–300, 2013.

[26] S. Döring, Power from pellets: Technology and applications, London: Springer, pp. 1–223, 2013.

[27] B. Yousaf, G. Liu, Q. Abbas, R. Wang, M. Ubaid Ali, H. Ullah, R. Liu, and C. Zhou, "Systematic investigation on combustion characteristics and emission-reduction mechanism of potentially toxic elements in biomass- and biochar-coal co-combustion systems," Appl. Energy, vol. 208, pp. 142–157, 2017.

[28] D. A. Agar, "A comparative economic analysis of torrefied pellet production based on state-of-the-art pellets," Biomass and Bioenergy, vol. 97, pp. 155–161, 2017.

[29] P. Bergman, A. Boersma, J. Kiel, M. J. Prins, K. Ptasinski, and F. J. Janssen, "Torrefaction for entrained-flow gasification of biomass," 2nd World Conf. Technol. Exhib. Biomass Energy, Ind. Clim. Prot., pp. 1–50, 2005.

[30] S. H. Larsson, M. Rudolfsson, M. Nordwaeger, I. Olofsson, and R. Samuelsson, "Effects of moisture content, torrefaction temperature, and die temperature in pilot scale pelletizing of torrefied Norway spruce," Appl. Energy, vol. 102, pp. 827–832, 2013.

[31] J. Peng, J. Wang, X. T. Bi, C. J. Lim, S. Sokhansanj, H. Peng, and D. Jia, "Effects of thermal treatment on energy density and hardness of torrefied wood pellets," Fuel Process. Technol., vol. 129, pp. 168–173, 2015.

[32] W. H. Chen and P. C. Kuo, "A study on torrefaction of various biomass materials and its impact on lignocellulosic structure simulated by a thermogravimetry," Energy, vol. 35, pp. 2580–2586, 2010.

[33] R. Isemin, A. Mikhalev, D. Klimov, P. Grammelis, N. Margaritis, D. S. Kourkoumpas, and V. Zaichenko, "Torrefaction and combustion of pellets made of a mixture of coal sludge and straw," Fuel, vol. 210, no. September 2016, pp. 859–865, 2017.

[34] C. Wang, Y. Chang, L. Zhang, M. Pang, and Y. Hao, "A life-cycle comparison of the energy, environmental and economic impacts of coal versus wood pellets for generating heat in China," Energy, vol. 120, pp. 374–384, 2017.

[35] M. T. Hansen, A. R. Jein, S. Hayes, and P. Bateman, English Handbook for Wood Pellet Combustion, vol. 30. Pelletsatlas, 2009, pp. 1–86.

[36] S. Gaur and T. B. Reed, "An atlas for thermal data for biomass and other fuels", Colorado: NREL, pp. 1–189, 1995.

[37] E. D. Vicente and C. A. Alves, "An overview of particulate emissions from

residential biomass combustion," Atmos. Res., vol. 199, pp. 159–185, 2018.

[38] H. Thomson and C. Liddell, "The suitability of wood pellet heating for domestic households: A review of literature," Renew. Sustain. Energy Rev., vol. 42, pp. 1362–1369, 2015.

[39] A. M. Pires, "Disponibilidade de Biomassa em Timor Leste. Avaliação de potencial e de disponibilidade para aproveitamento para produção de energia eléctrica," Oporto: MEGAJOULE, pp. 1–70, 2009.

[40] I. Macro, "Timor-Leste Demographic and Health Survey 2009-10," Dili: National Statistics Directorate Ministry of Finance, pp. 1-428, 2010.

[41] FAO, "Timor-Leste National Action Programme To Combat Land Degradation," Dili: Timor-Leste National Action Programme, 2008.

[42] W. Du, G. Shen, Y. Chen, X. Zhu, S. Zhuo, Q. Zhong, M. Qi, C. Xue, G. Liu, E. Zeng, B. Xing, and S. Tao, "Comparison of air pollutant emissions and household air quality in rural homes using improved wood and coal stoves," Atmos. Environ., vol. 166, pp. 215–223, 2017.

[43] A. T. Arif, C. Maschowski, P. Garra, M. Garcia-Käufer, T. Petithory, G. Trouvé, A. Dieterlen, V. Mersch-Sundermann, P. Khanaqa, I. Nazarenko, R. Gminski, and R. Gieré, "Cytotoxic and genotoxic responses of human lung cells to combustion smoke particles of Miscanthus straw, softwood and beech wood chips," Atmos. Environ., vol. 163, pp. 138–154, 2017.

[44] A. Castro, A. I. Calvo, C. Blanco-Alegre, F. Oduber, C. Alves, E. Coz, F. Amato, X. Querol, and R. Fraile, "Impact of the wood combustion in an open fireplace on the air quality of a living room: Estimation of the respirable fraction," Sci. Total Environ., vol. 628–629, pp. 169–176, 2018.

[45] PED, "Timor-Leste Plano Estratégico de Desenvolvimento 2011 - 2030," Dili: RDTL, 2011.

[46] P. Ferreira, "Combustion of alternative biomass fuels in a domestic boiler and in a large-scale furnace," PhD Thesis, University of Minho, 2016.

[47] E. dos S. Ferreira, "Launch of The Main Results of The 2015 Census of Population and Housing," 2016, Available at: https://www.laohamutuk.org/DVD/DGS/Cens15/Launch_2015_census_presentationEn.pdf.

[48] FAO, "Forestry Sector Policy Goal, Objectives And Strategies," Dili: National Forest Policy, pp. 1–14, 2005.

An Optimization of Cross-Flow Turbine Vanes in Enhancing Efficiency of Generating Voltage

Domingos de Sousa Freitas, Junior Raimundo da Cruz, Domingos de Regulau dos Santos, Octavio da Costa, and Miguel da Costa Soares

Departamentu Engenharia Mecanica, Universidade Nasionál Timor Lorosa'e (UNTL), Avenida Hera Cristo Rei, Dili, Timor-Lorosa'e

Email: nidodesousafreitas@gmail.com, jcruz.ray@gmail.com

Abstract: Hydropower energy is a renewable and clean source of energy which guarantees a sustainable energy development in future. This study is to optimize the cross-flow turbine vanes in enhancing the efficiency of the generated voltage. Three Types vane inclination are investigated. The efficiency of the generating voltage is measured and is compared to the existing result of pelton turbine at the same experimental setup. The experimental result shows that the enhanced vane of cross-flow turbine is performed better than the existing pelton turbine.

Keywords: renewable energy**,** cross-flow turbine, pelton turbine, penstock inclination

1. Introduction

Since 2011, the Timor-Leste government has invested the amount of annual budget 3 billion USD on infrastructure in general and particularly on the National electrification for more than 497 million USD [1]. As a result, 85% of communities who live in remotes, rural areas and national level have benefited from the power plants energy. These power plants were installed in 3 Municipalities with capacity 120 MW in Dili, 130 MW in Betano and Enclave Oekussi 17MW, and have been operating and supplying massive energy. The massive energy were supplied to only 1.2 million populations within the territory for multipurpose ends user such as international agency 7 %, socials 20 %, domestics 18 %, and commercials 5 % [2]. The energy is greater than energy proportion in Timor-Leste that only 65 % from the total energy were installed. Therefore, the national energy supplies in the country are considered surpluses which mean that, the supplied energy is greater than demanded energy. Referring to the National Program of Electrification, the demanding energy in the country were identified only 104,491 hh [3]. Figure 1 shows on of the country power plant at Hera power station and Figure 2 shows the map of national grid connection map throughout the country.

The power plant energy has brought its advantages to communities in remotes areas as well at national for education, health, and economy [4]. However, the technology itself has disadvantaged to current and future environmental sustainability such as climate change, extreme weather and high temperature [5]. In addition, it is also affect the maintenance costs of 53 million annual budgeting for operational and maintenance for two power plant stations in Dili and Betano [6].

Fig. 1 The power plant site at Hera Power Station

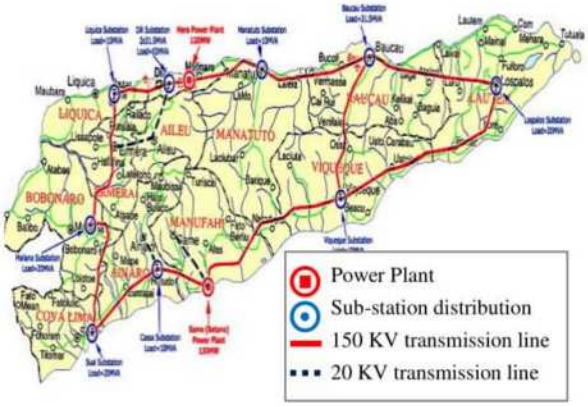

Fig. 2 The country national grid connection map

Even though Timor-Leste has been benefited with energy sources from fossil fuel, on the other hand, Timor-Leste also granted with renewable energy that given by the nature freely. The renewable energy sources are: Solar, Wind, Geothermal, Biomass, Hydroelectric, Wave and Hydrogen [8]. The development of renewable energy is aligned to the National Strategic Development Plan (PEDN) 2011-2030 which is highlighted that by 2020 Timor-Leste should implement half (50%) of energy system from renewable energy [10].

Even though some of the minis hydroelectric have been installed in Gariwai, Ainaro, most of them have been damaged. Since the average water sources in Timor-Leste are less than 10 meters, therefore the low head turbine is needed in such conditions. Hence, development of mini Pelton turbine for low head of 4 meters has been done and studied [11]. The development of an alternative cross-flow turbine should be required by investigating the effect of the vane inclination in order to optimize the efficiency of the runner speed and the output of the generated voltage.

2. The Existing Pelton Turbine and a New Turbine

We have developed a mini pelton turbine for low head of 4 meters. The developed mini pelton turbine is shown in Fig. 3. The type of runner in this study is bucket-type runner. The study performed on this turbine is to define the optimum angle of penstock. In order to optimize the turbine rotation, 220-volt electric output voltage is used. The result showed that penstock without reducer sprayed more water with more force therefore more electric voltage is produced.

However, the type of penstock without reducer wasted a lot of water which will become a bigger problem for low intake reservoir.

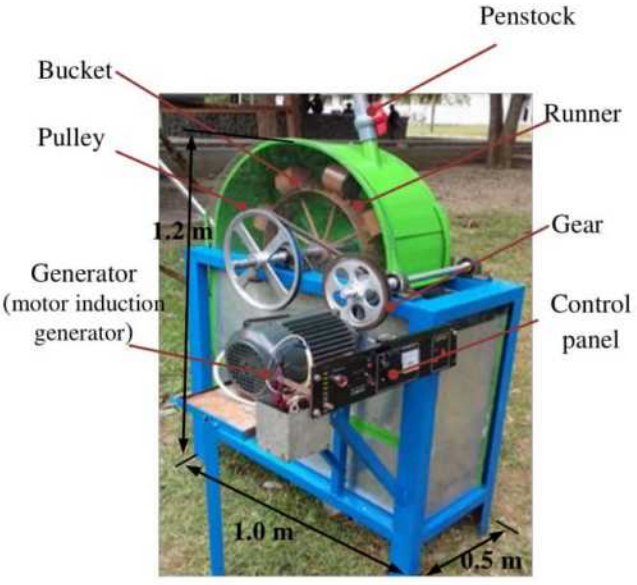

Fig. 3 Existing pelton turbine developed in ME laboratory-FECT-UNTL

The reservoir will be drained faster when the amount of output water is larger than intake water. The amount of flow-rate for penstock without reducer was 960 l/min in the previous study, while with reducer was only 75 l/min. Based on this result, we consider that it is the best to improve the turbine by using penstock without reducer. On the other hand, the turbine is performed better when the inclination of the penstock set at angle of 90°.

However, since it is a little difficult to set the 90° inclination on the field, we decided to optimize the turbine at the inclination of 40° angle in this study. If we are able to optimize the efficiency of runner and generated voltage at 40° inclination of penstock, the efficiency at 90° will be improved.

In the present study, we are trying to optimize the turbine runner using guide vanes which is known as cross-flow turbine. This turbine can be operated at vary head range from less than 2 m to more than 100 m [12]. The present cross-flow turbines with modified runner developed in Mechanical Engineering Department, Faculty of Engineering Science and Technology is shown in Fig. 4. The turbine property is presented in Table 1.

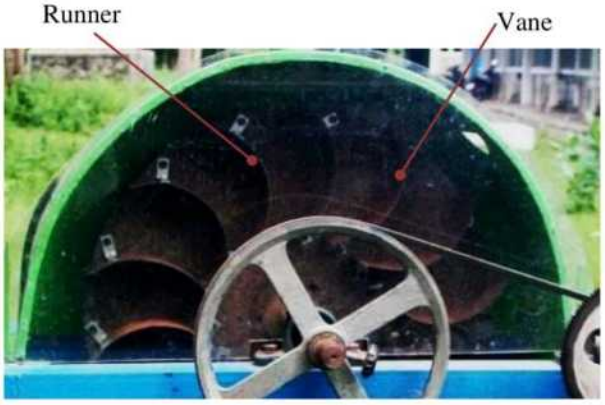

Fig. 4 Modified turbine runner with vanes (cross-flow type turbine)

Table 1. Technical property of cross-flow turbine

Head	4 m
Input pipe	1 inch
Runner	Ø 270 mm
Number of vanes	14
Big Pulley	300 mm
Small pulley	70 mm
Penstock	2 Inch
Penstock Reducer	2 inch to 1 inch
Number of Nozzle	Single
Type of generator	Converted generator (from induction motor)
Runner/generator rotation ratio	1 : 18

3. The Cross-Flow Turbine Performance Testing Method

3.1 The Support of Fundamental Equation

The Evaluation for turbine performance can be done using calculation method and experimental results. The general equations used are continuity, Bernoulli equation, brake horse power (BHP), water horse power (WHP), flow rate, and velocity. Turbine cross-flow power input can be calculated using the following formula:

$$\mathrm{BHP} = \frac{2\pi .n.T}{60}, \qquad (1)$$

where n is the turbine rotation (rpm) and T is the Torsi (Nm).

Turbine cross-flow power output can be determined using the following formula:

$$\mathrm{WHP} = \frac{\rho . g. Q. H}{3600}, \qquad (2)$$

where ρ is the water spesific weight (kg/m^3), g is the gravitational velocity (m/s^2), Q is the water flow rate (m^3/s), and H is the turbine head drop (m). Turbine efficiency can be determined by using the Bernoulli equation as an ideal fluid formula that particularly applied

for energy conservation law. In applying such equation, several criteria need to be considered. The fluid should be at steady flow, the fluid ideally should not be a viscosity (frictionless flow), and the fluid density (ρ) is constant (incompressible) that considered no energy losses during fluid flow.

$$\frac{P}{\rho .g} + \frac{V^2}{2 .g} + z = \text{total head (H) konstan}.....(3)$$

where P is the fluid static pressure (N/m^2), V is the fluid speed (m/s), g is the gravitational velocity (m/s^2), z is the elevation of the same datum (m), and ρ is the water spesific weight (kg/m^3).

The mass of a fluid flow occurred in a turbine can be calculated by using continuity equation as mathematical equation used to calculate the net of amount of fluid mass flow on a limited surface which is equal to the mass on the fluid flow surface. The volume of fluid to the input entry is equal to the fluid volume on the output entry.

$$\dot{m} = \rho_1 . A_1 . V_1 = \rho_2 . A_2 . V_2 \qquad (4)$$

The power of turbine can be calculated by using the formula

$$P = Q \times \rho \times g \times h \ . \qquad (5)$$

The water flow through the pipe has its mass. It gives a high pressure to the runner of turbine continues rotated the generator and turbine torque (T). The torque is obtained as follows:

$$T_t = F_t \times R \qquad (6)$$

$$F_t = \frac{P}{\omega \times R}, \qquad (7)$$

where F_t is the tangential force of water, R is the runner radius, and ω is the angular velocity.

3.2. The Experimental Setup

The schematic view of the experimental setup is shown in Fig. 5 In this experiment, we used the same setup as our previous experiment on Pelton turbine [10]. In this setup, water is filled into the reservoir that set on the top of tower with capacity 1100 ml and the distance of the reservoir from the ground level is 4 meters. The 2-inch diameter of polyvinyl chloride (pvc) pipe is connected to the reservoir outlet. This pipe is used to transfer water from reservoir to the turbine blades. At the outlet of the 2-inch pvc pipe, the 1-inch diameter of pvc pipe is installed to increase water velocity. This high velocity of the water will hit the vanes of runner which is installed at the end of the pipe. The angle of the water hits the turbine blades is set to 40°. When water hits the vanes, turbine runner rotates. This rotational force of the runner is then transmitted to the generator trough belt and gears. To increase the transmitted speed from the runner to generator, we used fixed pulley and gear with ratio 1:18. Since the rotation of turbine runner has a great influence on the performance of the output voltage from generator, therefore, we consider that by improving the angle of the vane will greatly improve the turbine output. The rotational speed of the runner is measured using Tachometer by measuring the rotation of the driving pulley and the output voltage is measured using multimeter.

3.3 The Experiment Parameters

In this experiment, we considered some reference value, fixed value and control variables as the parameters. These parameters are shown in Fig. 6. As explained earlier, the turbine head is 4 meter. This head was used, based on the consideration of the average head of waterfall in Timor-Leste. Other parameter is the inclination of the penstock which set to 40 ° angle. This angle of penstock inclination was decided with reference to our previous experiment on Pelton turbine [10]. We found on experiment that the

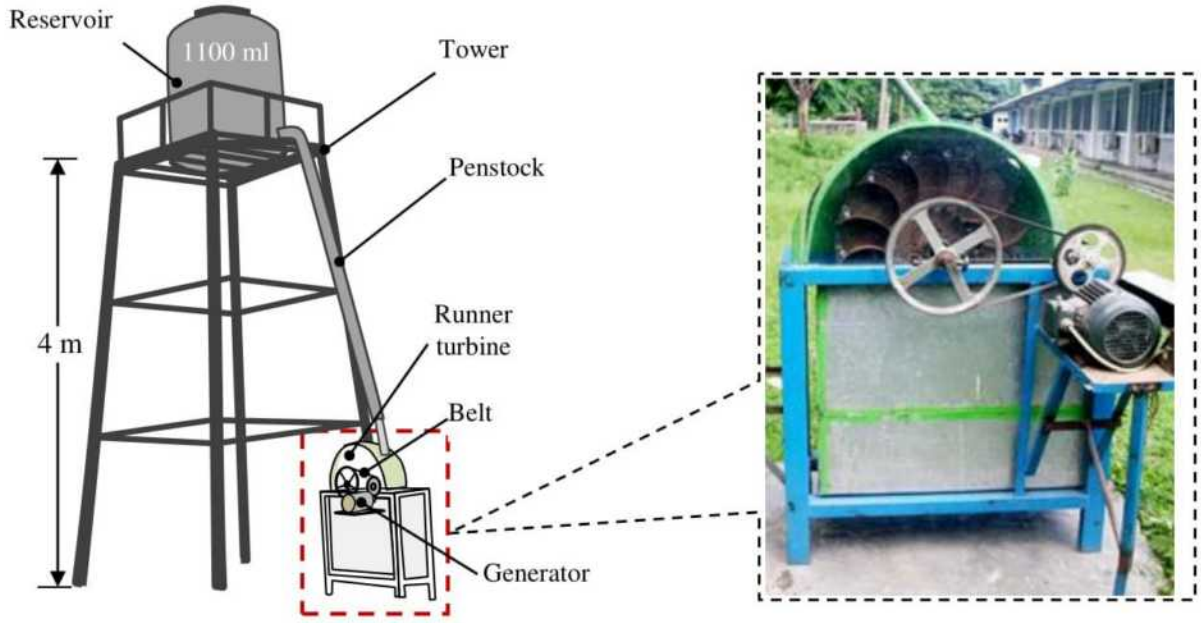

Fig. 5 The experimental setup

optimum angle of inclination is 90°. However, considering the difficulty of the installation and rigidity of the pipe, we take the 40° angle of penstock inclination and assuming that if we can improve the turbine efficiency at 40° angle, at the 90° inclination will also be improved. Hence, we used 40° angle of penstock inclination as a reference. Another fixed parameter is the transmission ratio. The used transmission ratio of the runner and generator in this experiment was set to 1:18, while the concave of runner´s vane was set to radius 45^0 and the reference output voltage of the generator is set to 220 volts. Since the rotation of turbine runner has a great influence on the performance of the output voltage of the generator, therefore increase the reservoir head, use optimum penstock inclination, use the optimum transmission ratio based on the runner rotation and use optimum angle of the runner´s vane can greatly improve the generator efficiency. Since the parameter for reservoir head, penstock inclination, transmission ratio and reference output voltage have been set to fix value, we find the optimum angle of the runner´s vane in order to improve the output efficiency of the generator voltage. Therefore, we consider the variation of the vane´s angle of the 7°, 14°, and 40°. The inclined vanes at position are aimed to accumulate the sprayed water from nozzle to the runner which can optimize the runner rotation and torque. As a result, the generator can rotate at its optimum rotation to produce the output voltage of 220 volt.

4. Result and Discussion

4.1 Relation Between Flow Rate and Turbine Rotation

The rotation of turbine´s runner depends on the water flow rate. The higher flow rates products the faster rotation of the runner and thus the energy will also be greater. Since the flow rate depends on the gravity force, increase in the height of the reservoir could improve the flow rate. However, we used the fixed height of reservoir which is 4 meter based on the average height of waterfall in Timor-Leste. This is referring to the most of

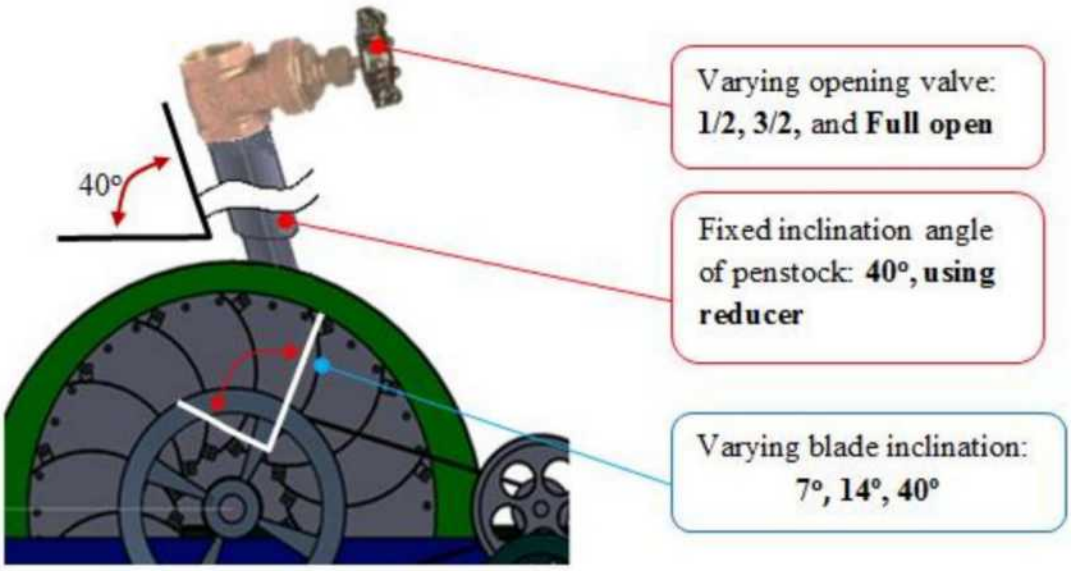

Fig. 6 The experimental parameters

Table 2. Control parameter and experimental condition

	Parameter	Value
Fixed parameter	Head (Reservoir)	4 m
	Penstock inclination	40°
	Penstock with reducer	2" to 1 "
	Concave vane radius	45°
	Transmission ratio (Runner: Generator rotation ratio)	1:18
	Output voltage	220 Volts
Variable parameter	Vane´s angle	7°
		14°
		40°

turbine that are applied in the field head, which is more than 10 meters (depends on turbine type). Therefore, our objective is to design and optimize the turbine which can be operated at low head.

Another condition that we used to increase the water velocity is reducing the diameter of pipe at the end of penstock from 2 inch to 1 inch. This reduction is made with accordance to the Venturi effect and Bernoulli principle that is: if the pipe or channeling shrinks, the fluid accelerates and the pressure decreases. Inversely, if the pipe goes larger, then the speed goes down and the pressure increases. In this experiment, the opening valve were varied from 1/2, 3/2, and full open in order to measure the flow rate based on the opening valve. Figure 7 shows the relation between opening valve and flow rate of water. When the valve is on half opening, the flow rate is 65 l/min, on 3/2 opening; the flow rate becomes 70 l/min, and on full open increase to 78 l/min. Based on this result, the full opening of the valve with flow rate of 78 l/min will be used throughout this research.

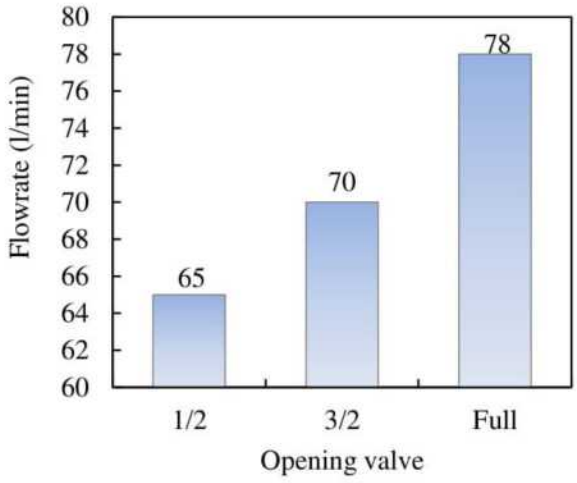

Fig. 7 Relation between opening valve and water flow rate

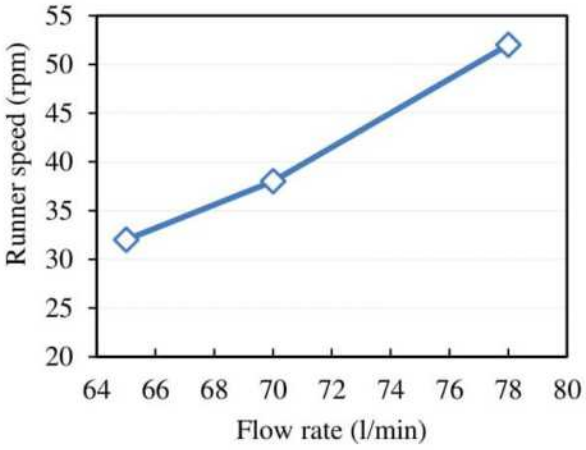

Fig. 8 Relation between flow rate and runner speed

Figure 8 shows the relation between the flow rate of water and turbine rotation. It is clear that when the flow rate goes up, the runner rotation will also increase. Therefore, the rotation of runner depends on the water flow rate which is setting at varies 65, 70, and 78 l/min, hitting the runner is 32, 38 and 52 rpm, respectively.

4.2. Relationship Between Angle of the Vane and the Runner Rotation

As explained in Section 3.3 that the blades inclination had a great impact on the runner rotation, therefore varying the vane's angle are important to define the optimum blade angle (inclination). The blade angle is considered optimum when the sprayed water hit on the vane at that angle that can create higher rotation speed that on other angle. Therefore 3 types of different blade inclination are used in this experiment such as; 7°, 14°, and 40°. The experimental result obtained from the relation between vane´s inclination and the rotation speed of the runner is shown in the Fig. 9. The result shows that the larger inclination of the vane gives the runner rotation becomes higher. The vane setting will obtain different runner rotation. When the vanes are set at the 7°, the rotation of the runner is 32 rpm. The runner rotation became 38 rpm at the vane's inclination of 14°, and is increased to the 52 rpm when the vanes were set at the 40°. The vary blade inclination of 7°, 14°, and 40° is the maximum angle that we were able to set on our turbine. The study proved that the vanes inclination at 40° degree gives runner higher rotation than other lower angle, hence we considered that the 40° is the optimum inclination angle for the vanes.

By observing at the water flow behavior that occurs, it can be seen that the acceptable runner blade inclination and direction of water flow rate would also affect the turbine performance. Inaccurate runner vanes inclination would affect the stability of turbine rotation. This is because the water turbulence will not hit right on the vanes to create optimum force in order to rotate the runner at the optimal speed. Because of not hitting on the right angle of vanes, it will cause a kinetic energy partial loss and as a result of unstable turbine rotation, and surely would reduce the turbine power.

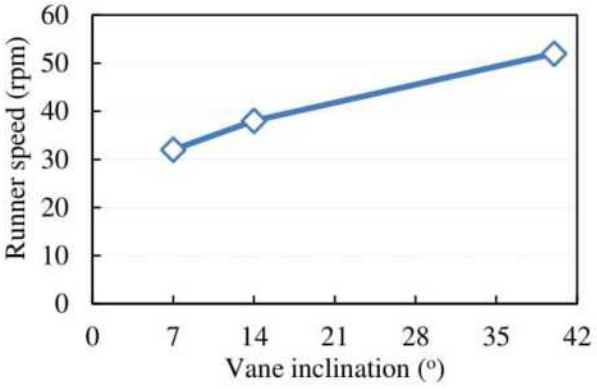

Fig. 9 Relation between vane inclination and the runner speed

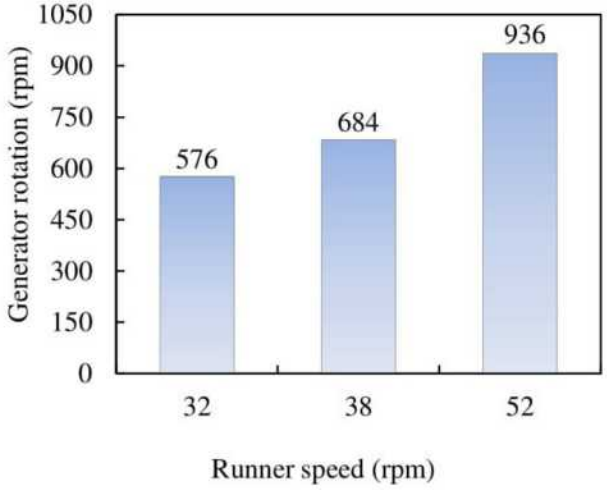

Fig. 10 The Relationship between runner speed and the generator rotation

Figure 10 shows the relationship between the runner speed and the generator rotation. The generator speed was calculated by measured runner speed multiply with the rotational ratio of the generator. The result shows that when the runner rotates at 32 rpm, the generator rotates at 576 rpm. The speed of rotation increases to 684 and 936 rpm when the runner rotates at 38 and 52 rpm, respectively. This generator rotation, from the speed of 936 rpm produces 105 V.

4.3. Comparison of Output Voltages Between with the Existing Result

In our previous experiment on pelton turbine [10], we achieved the output voltage of 200 V.

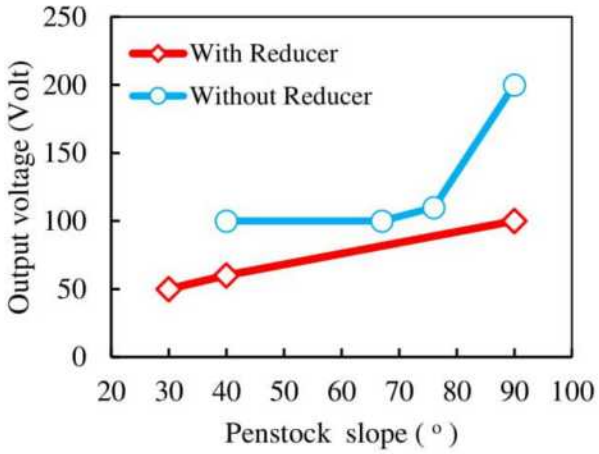

Fig. 11 The Relationship between runner speed and the generator rotation

Comparing to the current study on cross flow turbine, the results achieved on the pelton turbine is greater than the current output voltage. It seems very low. However, if we observe from the setting of penstock slope, there is big improvement on our current result. Figure 11 shows the result of our previous experiment for the pelton turbine on the relationship between penstock slope and the output voltage.

This result clearly shows that without using reducer, we achieved output voltage of 200 V at the penstock slope of 90° while without reducer, the voltage only 100 V at the same inclination of the slope. At inclination of 40°, the output voltage was 60 V without reducer and 100 V with reducer. Since our current experiment was performed using 40° angle of penstock inclination, the comparison will be done on this condition of penstock inclination.

Figure 12 shows the comparison between runner speed for cup type (pelton) and vane type (cross-flow) runner when the penstock inclination is set to 40°. At this inclination, the force of sprayed water can rotate runner with vanes about 37 % faster than cup type runner (pelton).

Figure 13 shows the comparison of output

voltage and its efficiency between our previous experiment on pelton turbine and current experiment on cross-flow turbine at the same penstock inclination of 40°. We observe that at the same penstock inclination of 40° angle, pelton turbine produces 60 V while cross-flow turbine produces 105 V, which is 21 % more efficient than pelton turbine. From this result we suggest that if pelton turbine is able to obtain the voltage of 200 V at the 90° of penstock inclination, our cross-flow turbine will definitely achieve the reference voltage of 220 V.

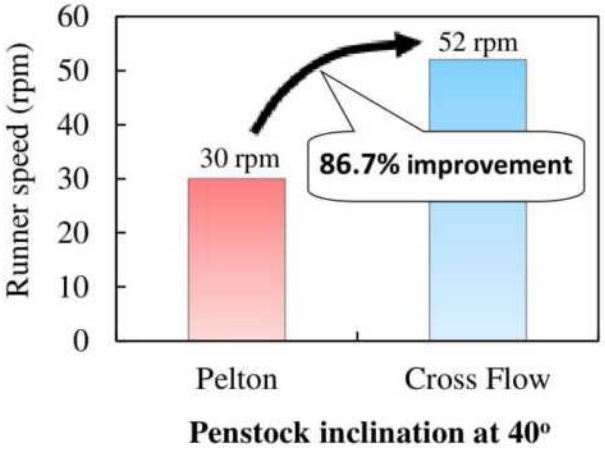

Fig. 12 Comparison of runner speed between pelton and cross-flow turbine.

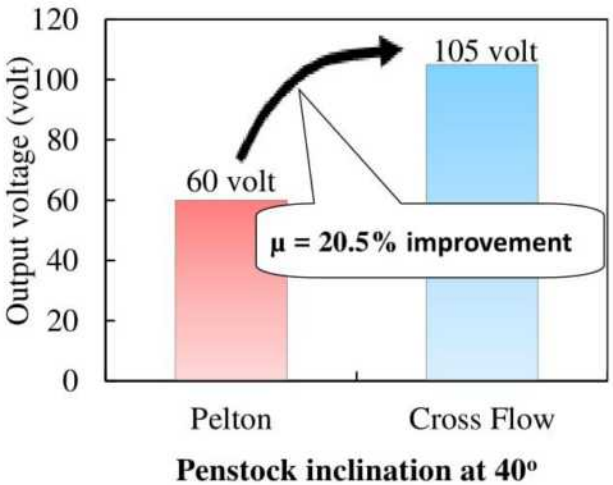

Fig. 13 Comparison of output voltage and efficiency between pelton and cross-flow turbine at 40° penstock inclination.

5. Conclusion

It was concluded that the vanes (blade) inclination was greatly affect the cross-flow turbine performance especially on the torque, transmitted power and the efficiency of the output generated voltage. The present experimental results have shown that by setting the penstock inclination at the angle of 40° and also vanes inclination at 40°, the runner can be rotated at the speed of 52 rpm, which rotates generator at the speed of 936 rpm and resulting in the output voltage of 105 V. Comparing this result to the existing result of the pelton turbine, which generate only the output voltage of 60 V when the penstock inclination was set at the same 40° angle, the current type of turbine perform better with efficiency of the output-voltage improvement of 21 %. Based on this result, it can also be concluded that since the current turbine has improved the output voltage with efficiency about 21 % on the penstock inclination of 40°. The output voltage will be surely improved.

References

[1] H. Davor (2015, October) Our Energy. [Online] Avaiable URL: https://www.our-energy.com/non_renewable_energy_sources.html

[2] E. Morse. (2013, February) National Geography Society. [Online] Avaiable URL: https://www.nationalgeographic.org/encyclopedia/non-renewable-energy/

[3] IJRER. International Journal of Renewable Energy Research (IJRER). [Online] Avaiable URL: http://www.ijrer.org

[4] Hydro Timor. (2010) Hydro Timor: Coordinating unit for hydroelectric development in Timor-Leste East Timor. [Online] Avaiable URL:https://www.loc.gov/item/lcwa00096642/

[5] Government of Timor-Leste. (2011, July) Timor-Leste Strategic Development Plan 2011-2030. [Online] Avaiable URL: http://timor-leste.gov.tl/wp-content/uploads/2011/07/Timor-Leste-Strategic-Plan-2011-20301.pdf

[6] V. Pierre-Louis, "From the water wheel to turbines and hydroelectricity. Technological evolution and revolutions," *Comptes Rendus Mecanique*, Vol. 345, No. 8, pp. 570-580, 2017. [Online] Avaiable URL:https://www.sciencedirect.com/science/article/pii/S163107211730092X?via%3Dihub

[7] Y. Nish, T. Inagak, Y. Li, and K. Hatano, "Study on an Undershot Cross-Flow Water Turbina with Straight Blades,"

[8] V.M Prajapati, R.H Patel, and K.H Thakkar. (2015) Design, Modeling & Analysis of Pelton Wheel Turbina Blade. [Online] Avaiable URL: http://www.ijsrd.com/articles/IJSRDV3I100075.pdf

[9] S. A. S. Obayes and M. A. K. Qasim, "Effect of Flow Parameters on Pelton Turbina Performance by using different nozzles", *International Journal of Modeling and Optimization*, Vol. 7, No.3, pp. 128-133, June 2017.

[10] S. Piyawat and S. Ratchaphon, "Comparative Study of Small Hydropower Turbina Efficiency at Low *Head* Water", *Energy Procedia*, Vol. 138, pp. 646-650, October 2017.

[11] Junior R. da Cruz, et al. A Study on Different Penstock Slope for Improvment of Pelton Turbine Efficiency, Timorense Academic Journal Science and Technology (TAJST), first edition, pp. 65-74, 2018

[12] J. Hoeiseth and K. Kassius. (2007) Gariuai Mini HEP: The First Hydroelectric Plant in a New Country. [Online] Avaiable URL: http://ahec.org.in/links/International conference on SHP Kandy Srilanka All Details\Papers\Policy, Investor & Operational Aspects-C\C22.pdf

Improvement of Surface Roughness of Ball and Radius Shape Workpiece by Using New Grinding Tools

Valerio de Sousa Gama, Agustinho Soares Madeira

Department of Mechanical Engineering, Universidade Nacional Timor Lorosa'e, Avenida Hera, Cristo-Rei, Dili, Timor-Leste

E-mail: valerio.gama@untl.edu.tl

Abstract: Three types of grinding tools for improving quality and accuracy of workpiece is proposed. The effectiveness of proposed technique is evaluated by several methods. Surface roughness of the workpiece is improved significantly by the proposed method, as compared with a normal cutting technique. It is concluded that, the surface roughness of the workpiece by using proposed method is 86% improved, compared to normal cutting.

Keywords: top slide, ball and radius shapes, grinding tools, surface roughness.

1. Introduction

Improvement of high quality and high accuracy of the ball and radius shape workpiece is required for each manufacturing company. Several methods have been using for producing ball and radius shape [1-4]. In previous studies, the apparatuses of new top slide were produced and in order to reduce the vibration, the modified one developed [5-6]. Those methods technically insufficient to perform ball or radius shape, when we require the improvement in quality and accuracy.

To achieve the high quality and high accuracy, technically higher quality of grinding tools is demanded for optimize the problem that we have mentioned. In this paper, we develop a new grinding tool especially for our proposal of top slide to grind a ball and radius shape workpiece. This new grinding tool is more compatible, more accurate and more suitable for the new top slide. Surface roughness of a ball and radius shape workpiece can be improved significantly.

2. Development of Top Slide and Newly Developed Grinding Tools

2.1 Development of Top Slide

It is important to enhance the quality of ball and radius shape produced by every method of cutting in machining process. The top slide is an attachment for lathe machine is used to perform ball and radius shape cutting. There were various types of top slide being developed by us, which are new top slide reducing vibration and surface roughness [5-6].

Figures 1(a), (b) show our developed new top slide in 3D model.

2.2 The Proposed New Grinding Tools

We have developed a lathe machine`s attachment for cutting ball and radius shape. However, the cutting result by conventional cutting tools is still not optimum. Therefore, in this study we develop a new grinding tool as shown in Fig. 2. This grinding tool is attached on the top slide to grind the ball and ball radius

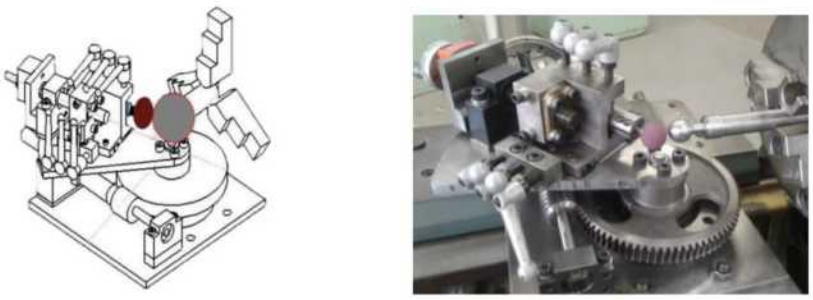

(a) 3D model **(b)** Photograph of top slide

Fig.1 3D model and photograph of top slide

workpiece in order to optimize the surface roughness.

The grinding tool of pink aluminum (PA) oxide was used in this method, because of utilization for the general-purpose grinding of most type of steel and iron and suitable for precision grinding application [7-8]. In Table 1 shows the properties of grinding tools. In case of the effectiveness of the grinding tools, we developed three different types of grinding tools; the rotating grinding tools, the fixed grinding tools and the rotating grinding tools with sand paper.

Table 1 Properties of grinding tools

Abrasive material				
Aluminum oxide			87-96%Al_2O_3	
Mounted point				
shape		Spec	code	
A25		PA46PV	CG9025	
Chemical properties				
High chromium				
Al203 (%)		Cr203 (%)		Na (%)
≥96.50		1.00-2.00		≤0.70
Physical properties				
Basic mineral	Crystal size	True density g/cm3	Bulk density g/ cm3	Knoop hardness kg/mm2
α-Al2O3	600-2000	≥3.90	1.40-1.91	2200-2300

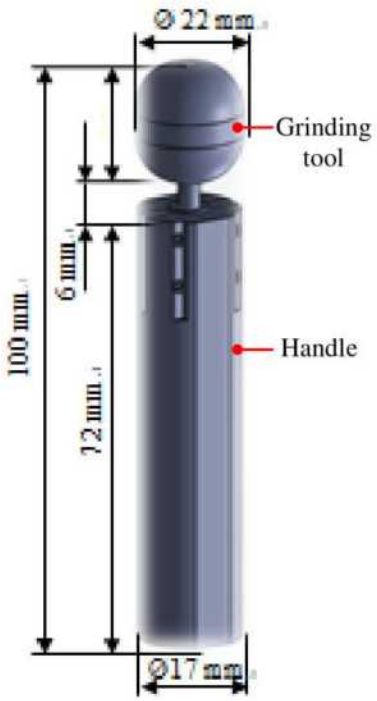

Fig. 2 3D of grinding tools

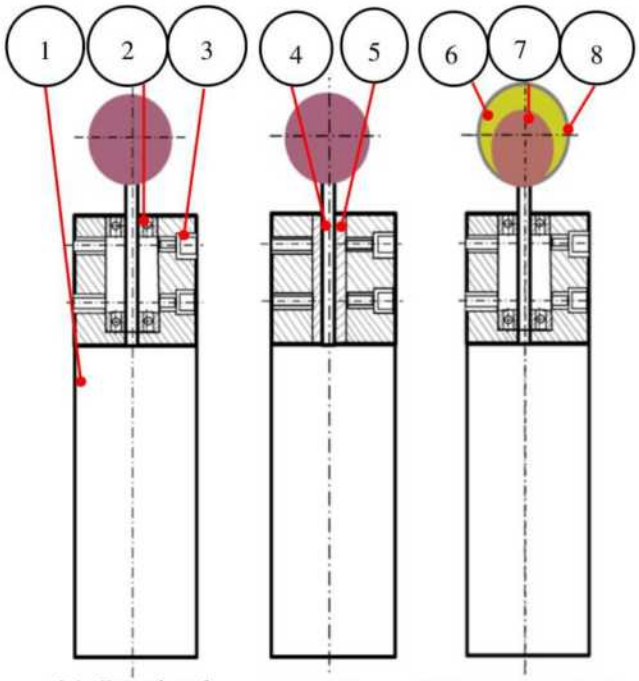

Fig. 3 schematic view of 3 types of grinding

Figure 3 shows the schematic view of three types of grinding tools. In Fig. 3(a) the grinding tools is inserted into the handle with the support of the two ball bearings. These bearing allow grinding tool to rotate freely inside the handle. Figure 3(b) shows the type of the grinding tool with fixed tools. The grinding tool is tightened and fixed to the handle using the screw. Figure 3(c) shows the same methods as grinding tools in Fig. 3(a). However, the head of the grinding tool is covered the head of the grinding tool with sponge and sand paper with grit No. 100. The name parts in each type of grinding tools, i.e., handle (1), bearing (2), screw (3), shaft of grinding tool (4), collect (5), sponge (6), grinding tool (7) and sand paper (8).

2.3 Cutting Mechanism of Proposed Grinding Tools

The grinding process by utilizing proposed grinding tool is performed by attaching and inserting the grinding tools to the top slide. At first, the workpiece is cut using cutting tools which is inserted on the top slide. After the desired ball or radius shape are achieved, then the cutting tools is removed and replaced with the proposed grinding tools to further improvement of the accuracy and surface roughness of the workpiece. The positioning of the grinding tools on the top slide is shown in Fig. 4. While the angle and maximum positioning of the grinding operation is performed, the grinding tools adjustment must be made towards the workpiece. The same adjustment method has been explained in our previous paper [5-6] is used in this study. As shown in Fig.5, the maximum angle for grinding tools movement is 139^0 from the center point of the workpiece and maximum is 278^0 angle around the workpiece. This is the limit of grinding tool movement.

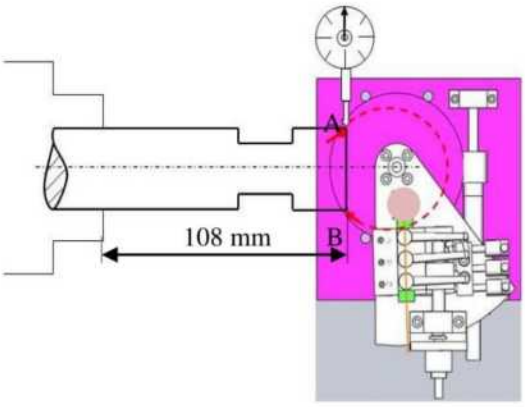

Fig. 4 Placement of tools grinding

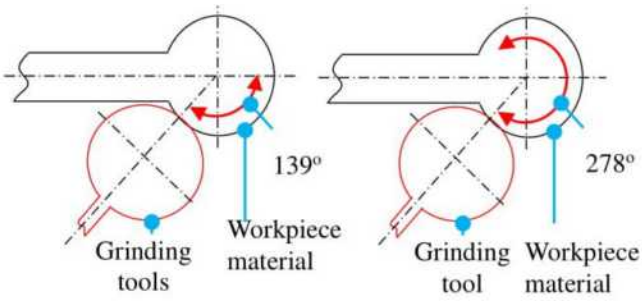

Fig. 5 Positioning of maximum operation grinding

3. Evaluation of Design

3.1 Mechanisms for Ball or Radius Shape

The schematic view of the mechanism for ball and radius shape grinding is shown in Fig.7. As explained earlier, the grinding is performed by inserting grinding tool on the top slide. The movement of top slide depends on the diameter of the ball or radius shape. At first, the grinding tool is set to the positioning (a), which is horizontal to the workpiece that is clamped on the penstock. When the handle of the top slide is turned, the grinding tools will move depending on the radius of ball. The moving sequence of the grinder is from (a) to (d). The maximum angle of the grinder movement from (a) to (d) is 139^0 as explained in the previous Section 2.3, making sure that, the feed speed of the grinding tool should be steady on moving continuously as an automatic operation. The maximum diameter of workpiece is allowed to be 40 mm

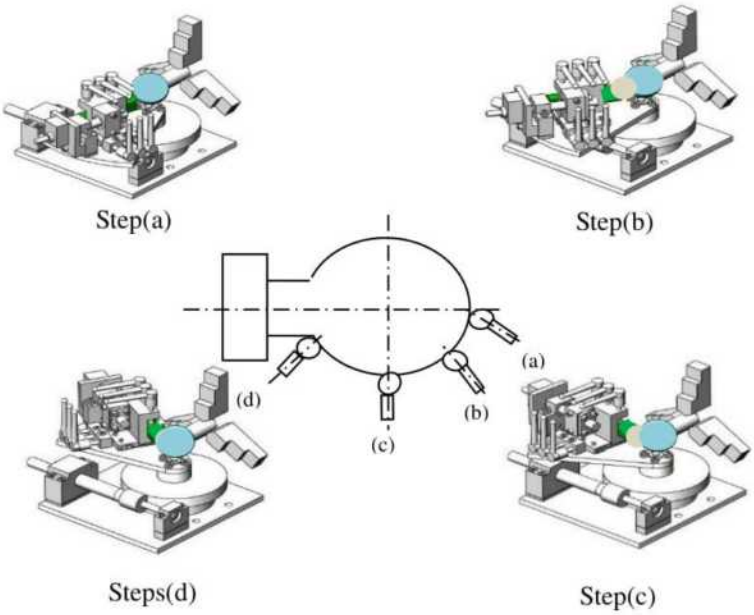

Fig. 7 Schematic view of the mechanism for radius shape

Table 2 Cutting condition and component force

	Item	Cutting condition	
Process condition	Cutting Speed	113 m/min	
	Feed speed	Manual	
	Depth of cut	0.5 mm	
Workpiece	Material	S45C	
	Size	ø 20 mm	
Tools	Material	Carbide	
	Coating	TiAiN	
	Rake angle	5^0	
Calculation main component of force, of the back-minute power			
Fh	Main component of force	126.07	N
Fv	Thrust force	44.013	N
I	Length rake face contact	0.18	mm
θt	Tool tip temperature	658.01	^{0}c

Table 2 shows the cutting condition and component force. The feed speed was operated manually. Therefore, the movement of feed speed should be constant (same as automatic operation). On the other hand, for grinding process, feed speed of grinding tool was also operated in manual operation but the rotational of grinding tools was rotated, same as the rotation of machine tools.

The main component of force, the back-minute power shown in Table 2 is calculated when carbide cutting tools is used for cutting the ball and radius shape [9-11]. The main component force is calculated by Eq. (1) and the specific cutting resistance is 2518.87 N/mm^2.

$$F_h = kfd_p \quad (1)$$

where, $F_h$is the main cutting force (N), k is the specific cutting force (N/mm), f is feed speed (mm/rev) and dp is the depth of cut (mm).

The back-component force is calculated by using Eq. (2). In this study the friction angle is 19.29^0 and the rake angle was 0^0.

$$F_v = F_h \tan(\beta - \gamma) \quad (2)$$

where; F_v is back component force (N), β is the friction angle (°) and γ is the rake angle (°).

The shear force on shear plane is calculated by using Eq. (3). In this study the shear angle was 25.71^0.

$$F_s = F_h \cos\emptyset - F_v \sin\emptyset \quad (3)$$

where; F_s is the shear force on shear plane (N) and Ø is the shear angle (^{0})

The tool tip temperature is calculated by using Eq. (4). In this study the flow ratio of chips to the frictional heat was 0.90 (-), unit time at the rake face, heating value of the area was 4.36E+08 W/m^2, and the length rake face contact is 0.000184 mm and thermal conductivity of the tool is 18 W/mK.

$$\theta_t = \frac{(1-R_2)q_f lS}{k_t}. \quad (4)$$

where; θ_t is the tool tip temperature (°C), R_2 is the flow ratio of chips to the frictional heat(-), $q_f$is the unit time at the rake face, heating value of the area(W/m^2), l is the Length rake face contact(mm), S is the Shape factor(-) and k_t is the thermal conductivity of the tool(W/mK).

3.2 Evaluation of Surface Roughness

The surface finish of the workpiece is the final step that could be achieved as small as possible. The advantage of the new grinding tool is that it can easily grind ball and radius shape to achieve high quality and high accuracy. In this cutting method, the surface roughness of the workpiece is under the International Standard Organization (ISO) standard [12, 13].

Figures 8(a) and (b) show the comparison of surface roughness between the normal cutting using carbide and finishing using our proposed grinding tools. The stylus type of surface roughness was measured with the surface roughness measuring instrument SJ-210. In our previous study [5.6], the result of surface roughness for the developed top slide and modified one was Ra 1.97μm and 1.06 μm, respectively.

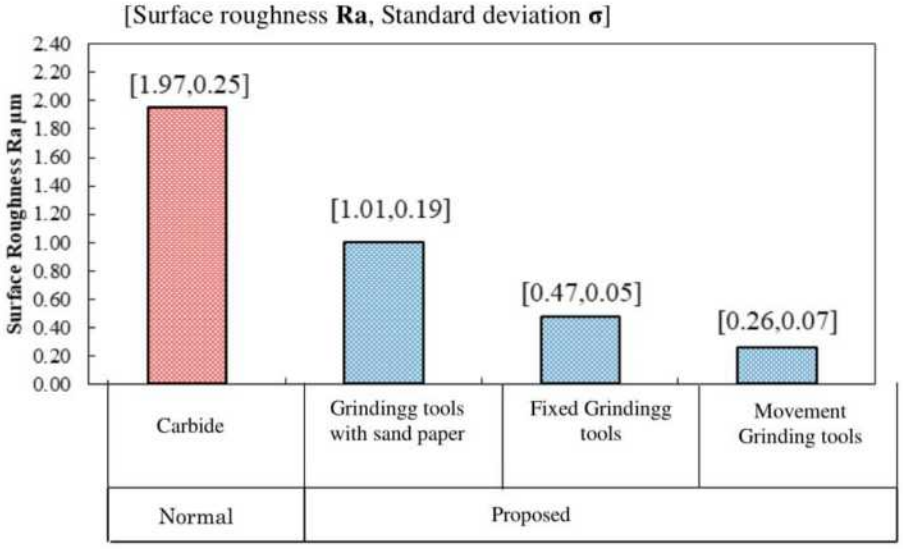

(a) Comparison of surface roughness

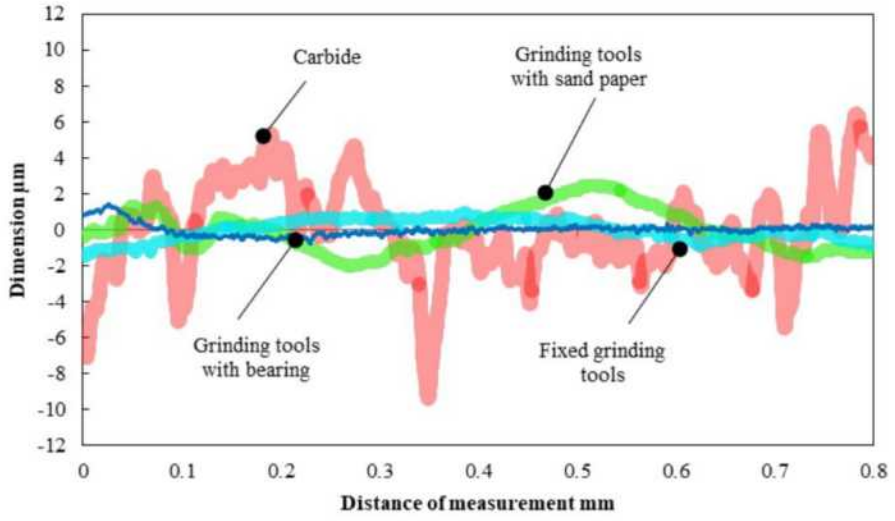

(b) Comparison of Surface profile

Fig. 8 The comparison result of surface roughness between normal cutting using carbide tool and proposed grinding tools

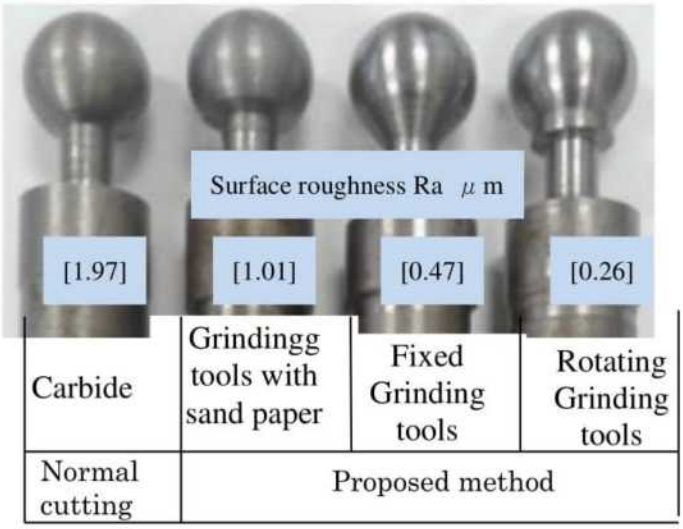

Fig. 9 Photograph of production results of the workpiece

In this study three types of grinding tools were developed and showed performance and surface roughness improved in each type. When using rotating grinding tools covered with sand paper, the obtained surface roughness was Ra 1.004 μm, which is 49 % improvement compared to the previous study. When the fixed grinding tool was used, the surface roughness reduced to Ra 0.472 μm, which is 76 % improvement. The surface roughness reduced further to 0.261μm, which is 86% improvement compared to the previous study when using proposed rotating grinding tool. The obtained surface roughness and the surface profile proved the effectiveness of the new top slide and development methods. On the other hand, the standard deviation of each surface roughness shown in Fig. 8 shows the extent of the accuracy of the measured surface roughness [14]. The smaller the standard deviation, the more accurate surface result will be given by

$$\sigma = \sqrt{\frac{\sum(x_i-\mu)^2}{N}} \qquad (5)$$

where; $\sigma$is the standard deviation, x_i is the data of measure surface roughness and μ is the average value and N is the number of measurements. The standard deviation of surface roughness obtained by carbide tool was 0.251. It should be noted that, by grinding tools with sand paper, fixed grinding tools and movement grinding tools the standard deviation, respectively, were 0.186 0.053 and 0.074. Therefore, the improvement of surface roughness of each type of grinding tools shows the effectiveness of the proposed method.

Figure 9 shows the photograph of the production result. It is shown that, the ball produced by the new top slides is similar to the ball produced by CNC lathe machine.

4. Conclusion

We obtained the following conclusions:

(1). The top slide was designed for changing the original tool post, for the ball and radius shape cutting on conventional lathe machine.

(2). The new top slide could be mounted and operated easily.

(3). The effectiveness of each grinding tools has shows good enough.

(4). The improvement of surface roughness of the workpiece obtained by the proposed method was 86%.

References

[1] Omnitasker, "Quick change radius (ball) turner for metal lathe", Feb. 10, 2016. [Online].Available:URL:http://www.instructables.com/id/Quick-Change-Radius-Ball-Turner-for-Metal-Lathe.

[2] M. Patel, D. Pateliya, A. Parmar, B. Kapadiya, "Design of fixture for radius turning on lathe machine", International Journal of Advance Research and Innovative Ideas in Education (IJARIIE)-ISSN (O), vol. 3 issue-2 pp.2395-4396, 2017.

[3] Sherline Products, "Radius Cutting Attachment". [Online] Available URL:https://sherline.com/Wordpress/wp-content/uploads/2015/01/2200inst.pdf

[4] Reed M. Streifthau, "Spherical turning tool". [Online] Available: URL:http://www.opensourcemachinetools.org/archive-manuals/spherical-turning-tool.pdf.

[5] V. de S. Gama, H. Hoshino, H. Kawanishi, I. Tanabe, L. da Costa, "Design and fabricate new top slide for making Ball and Radius Shape in conventional Lathe Machine", Timorese academic journal of science and technology, Vol 1, pp. 30-36, April 2018.

[6] V. de S. Gama, Adelson Lopes, "Development of new top slide for ball and radius shape cutting on conventional lathe machine" Timorese academic journal of science and technology, Vol 1, pp. 46-53, April 2018.

[7] GRINDING WHEELS,[online], available on;https://www.sgabrasives.co.nz/wp-content/uploads/2016/04/S-G-Bonded-Super-Abrasives-2016-1.pdf.

[8] Abrasive vortex group[online] available on:http://www.vortexabrasive.com/pink-aluminium-oxide.html.

[9] Paragon Invent D.O.O. SrečkoFratnik, All Rights Reserved. Graphic Design, Copyright © SWATYCOMET 2015, pages 66, [online] available, URL:http://www.swatycomet.com/fileadmin/documents/VsiPDF/IBO_2015_VITRIFIED&RESIN_BONDED.pdf.

[10] Geoffrey Boothroyd, Winston A. Knight, Fundamentals of Machining and Machine Tools, Second Edition, University of Rhode Island Kingston, Rhode Island, pp 90-94.

[11] Edward M. Trent, Paul K. Wright, Metal Cutting, Fourth Edition, Copyright © 2000 by Butterworth–Heinemann, pp. 57-68.

[12] Geoffrey Boothroyd, Winston A. Knight, Fundamentals of Machining and Machine Tools, Second Edition, University of Rhode Island Kingston, Rhode Island, pp 112-113.

[13] Erik Oberg, Franklin D. Jones, Holbrook L. Horton, Henry H. Ryffel, "Machinery`s handbook", 26th edition, industrial press Inc. New York, p. 703, 2000.

[14] Erik Oberg, Franklin D. Jones, Holbrook L. Horton, And Henry H. Ryffel, 26th Edition, Machinery's Handbook, 2000, INDUSTRIAL PRESS INC. NEW YORK, pp. 1216-1224.

Effects of Transmission Errors on Noise and Vibration of Gears

Marfim Guimaraes

Department of Mechanical Engineering, Faculty of Engineering Science and Technology, Universidade Nacional Timor Lorosa'e, Avenida Hera, Cristo-Rei, Dili, Timor-Leste

E-mail:marfim_guimaraes@yahoo.com

Abstract: This article deals with the effects of transmission errors on noise and vibration of spur gears. Two types of gears, plastic and steel gears, are used for evaluation of the noise and vibration of spur gear system. The transmission errors of test gears were estimated by the Multi Body Analysis (MBA). It was found that a reasonable correlation between calculated results obtained by the MBA and the experimental results.

Keywords: Spur Gears, transmission errors, Multi body analysis

---

1. Introduction

The plastic gears have considerable advantages in cost, weight, noise, wear, lubrication etc., comparing with steel gears [1]. It is generally suggested that noise of the plastic gears is smaller than that of the steel gears. Further noise reduction is strongly desired because the products with plastic gears are often used [1, 2].

Previous experimental results showed that the sound pressure level of plastic gears is lower than that of steel gears. In order to realize further noise reduction of plastic and steel gears, it is essential to investigate the fundamental features of the plastic gear noise. In this research, effect of transmission errors on noise and vibration of gears is investigated, because this affects the noise and vibration of gears system [3, 4].

The transmission error TE is defined by [3]:

$$TE = \theta out - \gamma \theta in, \quad (1)$$

where, θ_{in} is the input rotational angle, θ_{out} is the output rotational angle and γ is the reduction ratio.

In the past decade, the classification and basic formula of the spur gears, pressure angle, and tooth profiles have been studied [2,3]. However, the transmission errors of the spur gear have not been studied, expect for the measurement as a product evaluation. It is commonly understood that the transmission of gears is a vibration source. Therefore, study of the transmission error is important to reduce the vibration.

2. Experiment

2.1. Experimental Apparatus

(a) Steel drive gear (b) Plastic driven gear (c) Steel driven gear

Fig. 1 Test gears specification

Test gears are shown in Fig.1 and Fig.2 shows the top view of the experimental apparatus used in this study. Experimental apparatus is composed of a drive motor (a stepping motor, 450~3000rpm), a drive shaft with a steel master gear and a driven shaft with a tested plastic gear. Both shafts are supported by pedestals through ball bearings. A driven shaft span (a distance between bearing center lines) is adjustable by changing the driven shaft length and a pedestal position in the shaft axial direction. A shaft center distance between the two shafts is adjusted by moving the assembled driven shaft system in the lateral direction of the shafts with the aid of a slider table.

Specification of the gears is shown in Table1. The drive gear is made of steel (JISM0 grade) and has 0.8 modules, number of teeth 60, pressure angel 20ºand gear width 12mm. The material of plastic gears is poly acetylene resin. The modules, pressure angle and numbers of the teeth of the tested gear, are the same as the drive gear (precision JISM3 grade).

vibration is show in Fig.3.

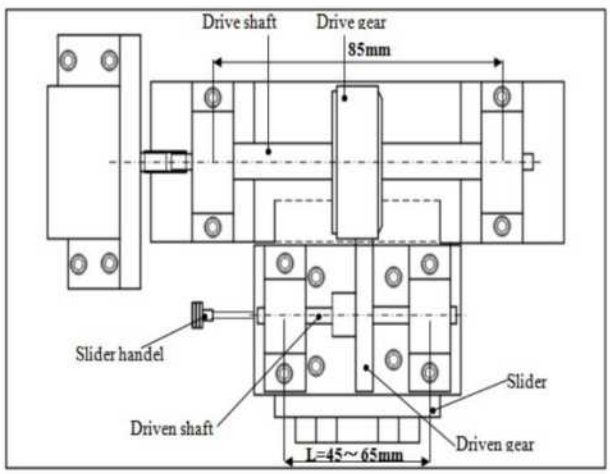

Fig. 2 Experimental apparatus

Table 1 Gear specification

	Drive gear	Driven gear
• Module	0.8 mm	0.8 mm
• Number of teeth	60	60
• Pressure angel	20°	20°
• Radius of pitch circle	24mm	24mm
• Radius of outside circle	24.75 mm	24.75 mm
• Radius of base circle	23.15mm	23.15mm
• Tooth width	12mm	5mm
• Materials	steel	plastics and steel

2.2. Measurement Method

In the experiment, rotational speeds are from 450 rpm until 3000R rpm with zero range and 30Nm load torque. Input rotational angel θ_{in} and output rotational angle θ_{out} were detected by rotary encoder. Then transmission error TE calculated using Eq. (1) with the result of

3. Multi Body Analysis (MBA)

To analyze the effects of transmission errors, the multi body analysis (MBA) software is used. In the MBA, model contact force between two gears is defined by [3]:

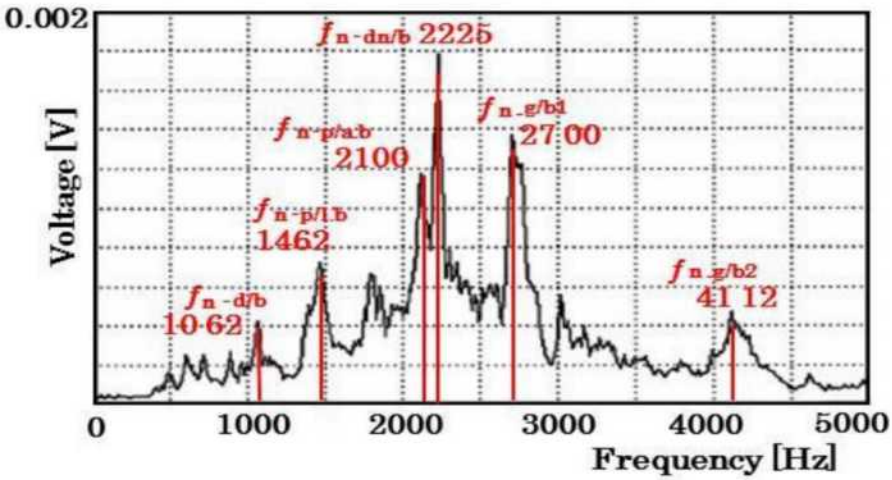

Fig. 3 Overall vibration and noise spectrum

$$F = \sqrt{F_N{}^2 + F_F{}^2} \quad (2)$$

Where F_N is the normal force and F_F is the friction force.

F_N and F_F are normal force and friction force on the tooth surfacein the two spur gear, respectively, [3]. The normal contact force is obtained by:

$$F_N = 1.85 \times 10^4 \times LW^{0.89} \times \delta^{1.11} \quad (3)$$

for steel/ plastic gears, and

$$F_N = 8.06 \times 10^4 \times LW^{0.89} \times \delta^{1.11} \quad (4)$$

for steel/ steel gears,

where L (mm) , efective contact length between surface of twin gears and δ (mm) is a normal elastic deformation for two gear. The friction characteristic bewteen tooth surface used in MBA are shown in the Fig. 4.

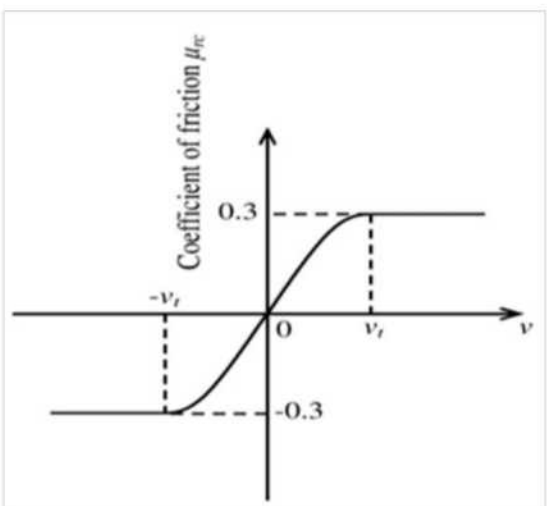

Fig. 4 Friction characteristics of tooth

Here,μ (v) is the friction coeficient at the realtive velocity v. The friction charcateristic between tooth surface is assumed to increases as relative velocity increases, while the relative velocity is changed from zero to transition velocity [3]. For the MBA, the comercial software RECURDYN was used. The results with the MBA will be carried out base on operational conditions in Table 2. The results is shown in Fig. 6,

Transmission error of palstic gear is lower than the steel gear.

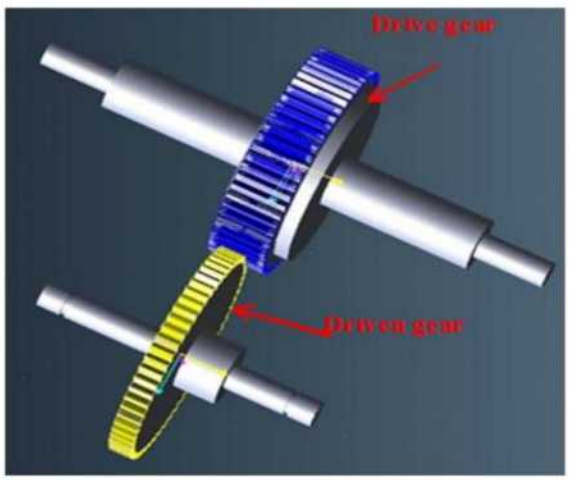

Fig. 5 Multi Body Analysis Model (MBA)

3.1 MBA Model

A model used in the MBA is shown in Fig. 5. In the MBA model, the drive and driven gears were assumed as rigid bodies expect for mesh of gear. For the sake of simplicity, the drive and driven gear were supported by revolute joints and they were constrained in an in-plane position. Due to this simplicity gears can only rotate around the input and output shaft. The operational conditions in MBA are shown in Table2.

Table 2 Operational conditions on MBA

Rotational speed N = 450 and 3000 rpm
Load toque T = 0 and 30 Nmm
Length of driven shaft L = 60 mm
Diameter of driven shaft = 6 mm
Thickness of driven gear t = 5 mm
Length of drive shaft = 110 mm
Diameter of drive shaft = 12 mm
Two revolute joint
Two spur gear
Gear contact element

4. Multi Body Analysis (MBA) Results

4.1 Calculated of Transmission Error

The typical results of spur gear by the MBA are shown in Fig.6 In the MBA model there are two pair of gear; the first is steel gear installed on drive shaft and we called drive gear and the second, the steel or plastic gear installed on driven shaft and we called driven gear. Based on this MBA, load (T), transmission error and rotational speed have a linier relationship but transmission error of steel gear and Plastic gear pair is lower than steel gear and steel gear pair.

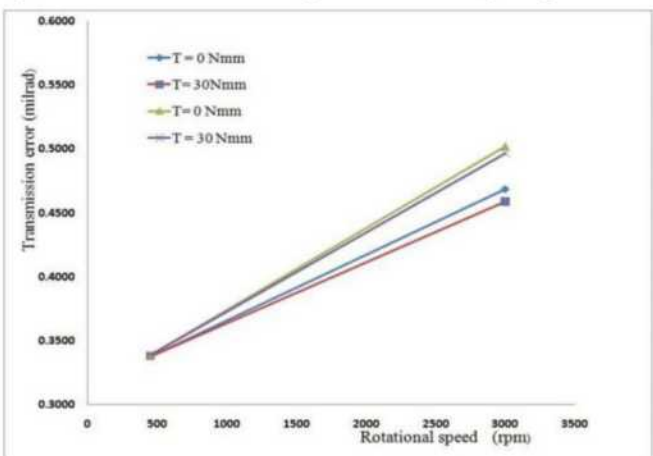

Fig. 6 Result of Multi Body Analysis (MBA) model

4.2 Transmission Error Waveform

The typical results of transmission error by MBA are shown in Figs.7 and 8. Peak to peak value of transmission error of gear meshing ($1/f_m$) and transmission error of rotational speed ($1/f_r$) are shown in figures [3]. The results of waveform transmission error of steel and plastic gear under rotational speed (N) 450 and 3000 rpm are 0.338, 0.338, 0.469, and 0.459 mrad, respectively.

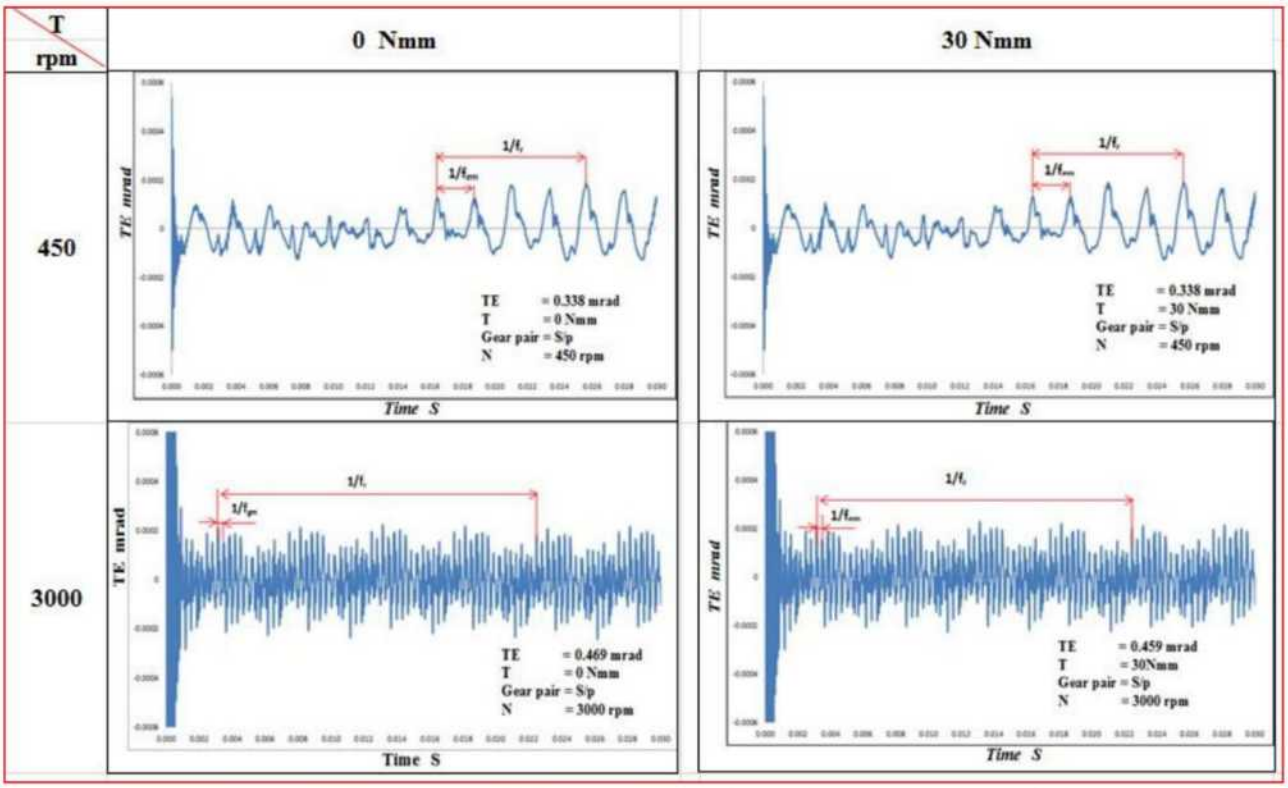

Fig. 7 Calculated transmission error waveform of gears (Steel/Plastic)

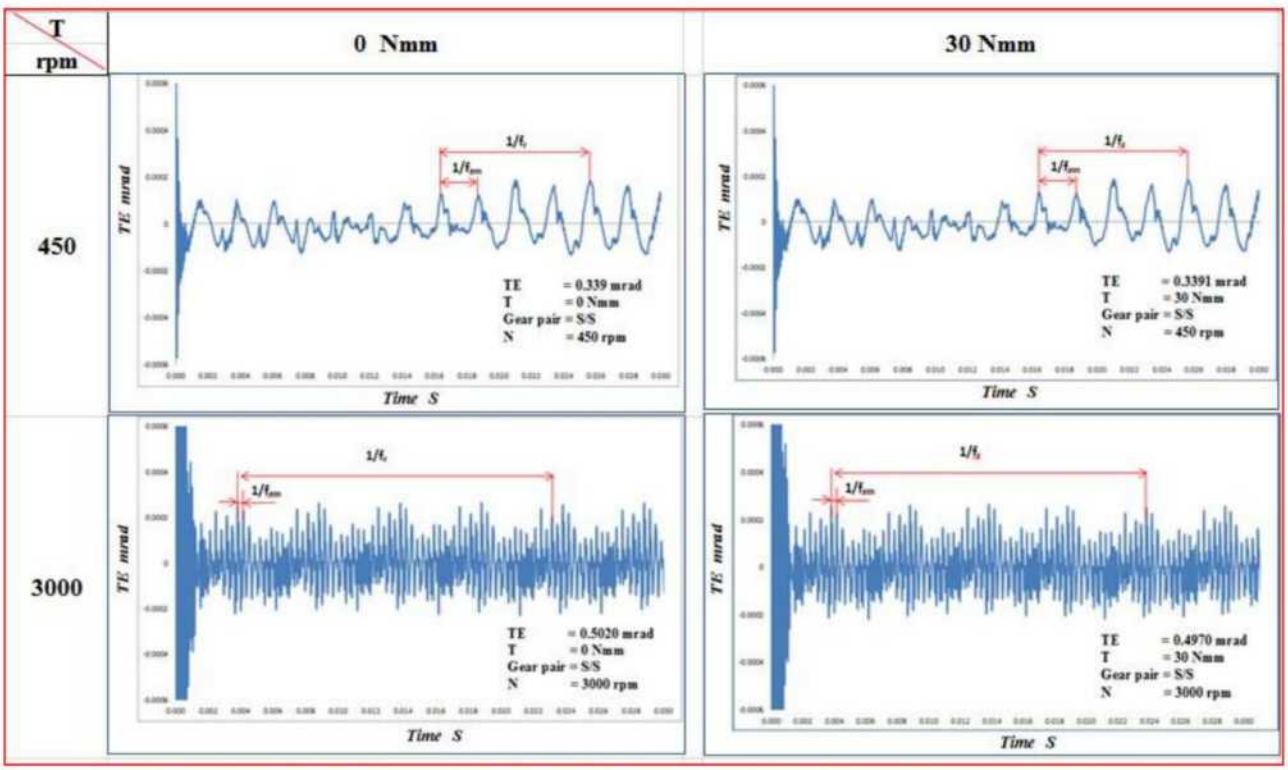

Fig. 8 Calculated transmission error waveform of gears (Steel/Steel)

4.3. Transmission Error Spectrum

The typical results of transmission error of spectrum by MBA are shown in Fig. 9 and Fig. 10 Spectrum of gear meshing frequency and rotational frequency related transmission error of gear system of steel and plastic gear under rotational speed (N) 450 and 3000 rpm are 0.3378, 0.4685, 0.3391, and 04587mrad, respectively.

The spectrum transmission error of steel and steel gear under rotational speed (N) 450 and 3000 rpm are 0.3392, 0.5020, 0.3391, and 0.4790 mrad, respectively. Waveform and spectrum of gear system, both parameters used to determine transmission error (TE) of gears and roll mechanism.

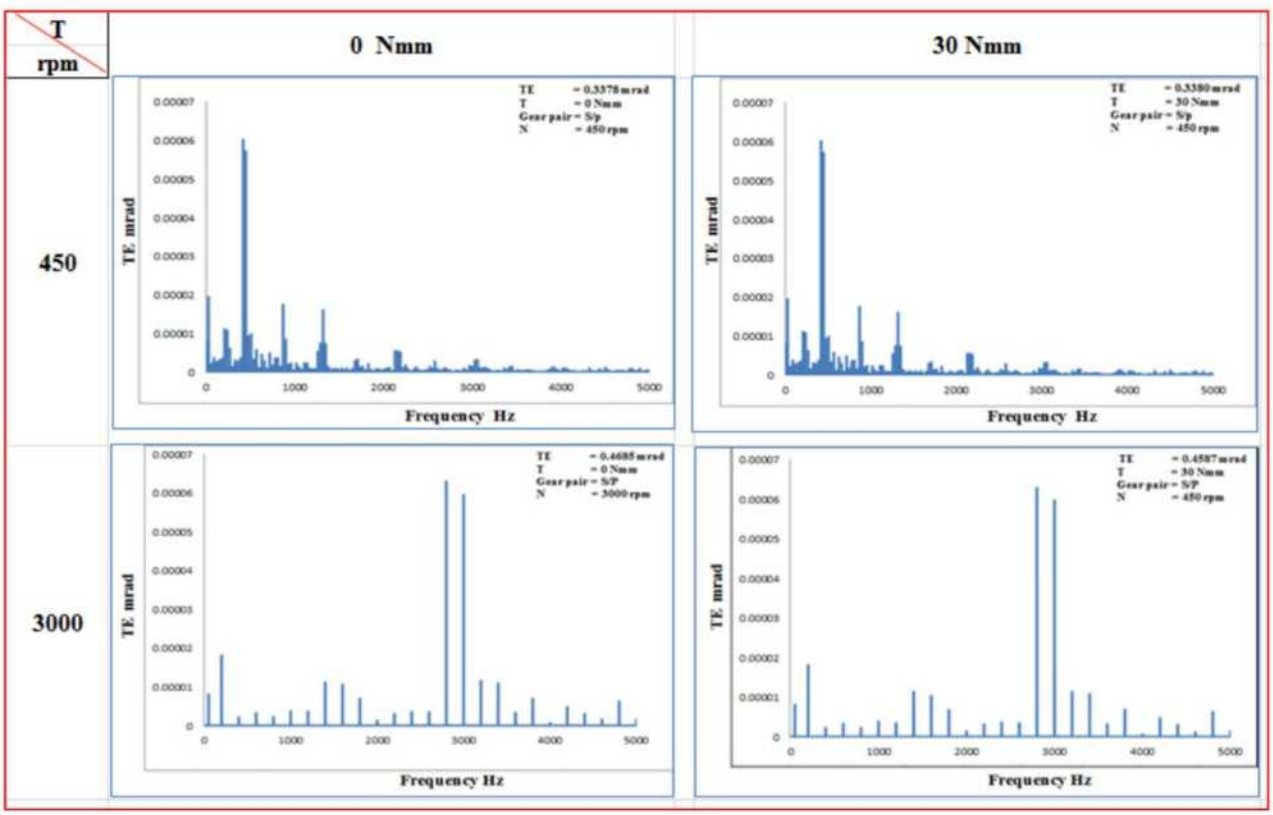

Fig. 9 Calculated transmission error spectra of gears (Steel/Plastic)

5. Conclusions

Summary is given as follows:

1. Calculated transmission error *TE* of the gears increases as the rotational speed increases.
2. Load torque does not significantly affect on the calculated transmission errors.
3. Under the same operating condition, the

Acknowledgement

The author wishes to thank the JICA CADEFEST project for supporting the present research. Furthermore, the author also acknowledges the Department of Mechanical engineering for helpful support in conducting research activities. Finally, thanks to all my colleagues directly or indirectly support my research activity.

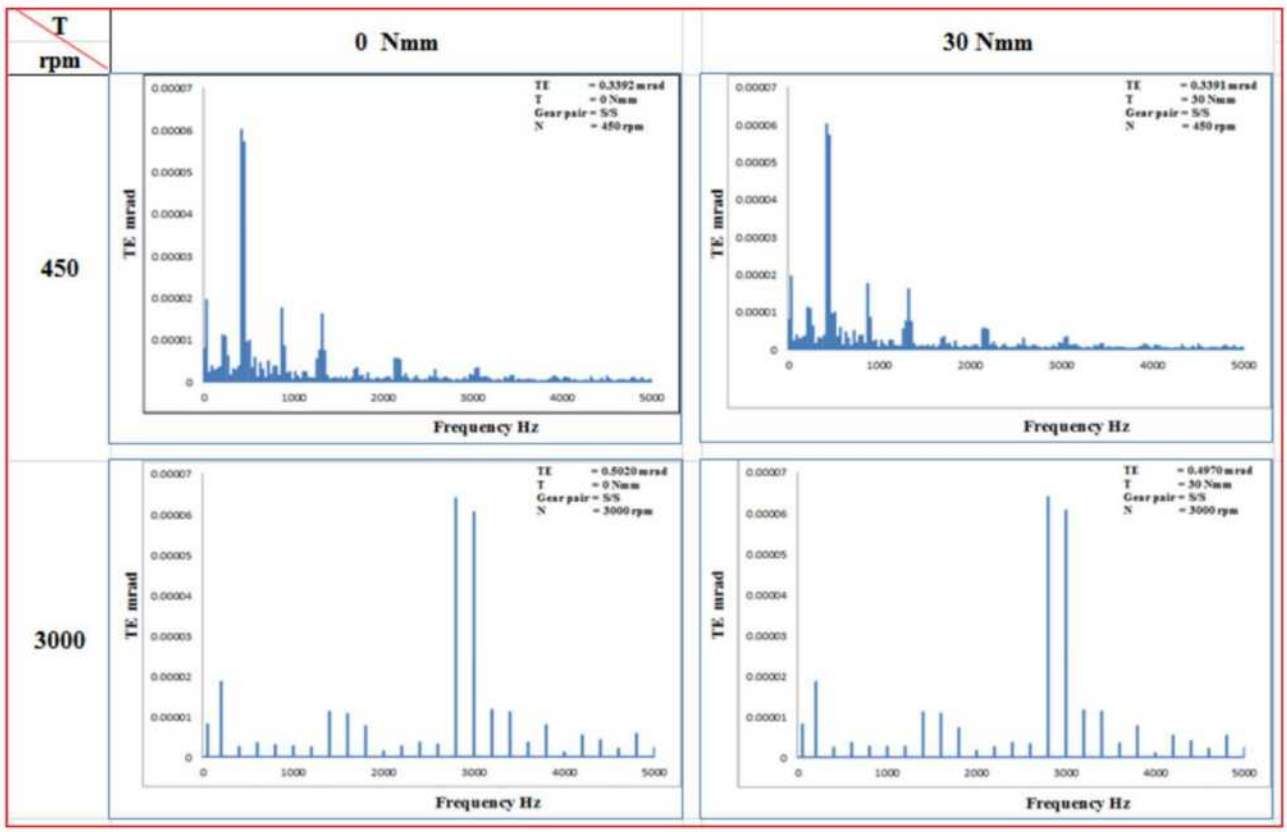

Fig. 10 Calculated transmission error spectra of gears (Steel/Steel)

References

[1] Oogiya, Y. *et.al*, "Noise and Vibration of Plastic Gears for Power Transmission Influence of meshes State on noise Generation", MPT-symposium, L5171A, Vol.2007, pp.242-245.

[2] Ashish N. Taywade,Dr.V.G Arafpura "Experimental Investigation of Noise and Vibrations in Nylon 66 Plastic Helical Gear used in Automotive Application",Journal of Mechanical Engineering, SSRG-IJME-Vol. 2 Issue 3, March 2015.

[3] Hiroyuki Otha, Ayumu Yamakawa, Yoshitaka Katamaya "Effects of Eccentricity on Transmission Errors of Trochoidal gears", copy right@ by ASME, January 2012, Vol.134/011102-1, Journal of Tribology).

[4] R. Kumar, N. Tiwari, D. Kunwar, R.R Vara Lashmi, M. Chhetri "Transmission error on spur gears", International Journal of advanced Engineering research and studies (IJAERS) Vol. I, Issue III, April-June 2012, pp. 122-125)

[5] Kuriso, T. *et.al*, "Mechanism Analysis of Automatic transmission gear noise", Seoul-2000 FISITA word automotive congress, (200-6), F2000H229.

Experimental Study on Noise of Gear System

Marfim Guimaraes

Department of Mechanical Engineering Technology, Faculty of Engineering Science and Technology, Universidade Nacional Timor Lorosa'e, Hera East Timor (UNTL)

E-mail: marfim_guimaraes@yahoo.com

Abstract: Effects of the bearing span and backless on the noise of a gear system are experimentally investigated. The apparatus is composed of a driving motor, a steel master gear on a drive shaft, tested plastic (poly-acetylene) and steel gears attached on driven steel shaft. The tested gear is made of Poly-acetylene resin. The Fast Fourie Transform (FFT) is performed to analyze with operating these gears in the speed range of 450~3000rpm under no load, truly, both noise and vibration of the gear system. The main frequency components are clearly obtained through the FFT technique.

Keywords: Noise, plastic gear, bearing span and shaft center distance

---

1. Introduction

The plastic gears have considerable advantages in cost, weight, noise, wear, lubrication. It is of interest to compare with steel gears. It is generally understood that noise of the plastic gears is smaller than that of the steel gears. Further noise reduction should be highly requested, since the products with plastic gears are now very popular [1-3].

In order to realize further noise reduction of plastic gears, it is essential to investigate the fundamental features of the plastic gear noise. In this research, effect of bearing span and backlash of the noise of the plastic gear are experimentally investigated by using a horizontal type apparatus with parallel two shafts. The apparatus is composed of a driving motor, a steel master gear in drive side, a tested plastic driven gear with steel shaft. Effects of the plastic gear thickness and plastic gear shaft length on the noise are investigated [2-4]. The present system in the speed range of 450~3000rpm under no load conditions, noise of the gears system is operated in Sound Pressure level (SPL) and is analyzed by the Fast Furrier Transformer (FFT).

2. Experimental

Figure 1 shows a top view of the experimental apparatus used in this study, which is composed of a driving motor (a stepping motor, 450~3000rpm), the driven shafts with the steel master gear and the testing plastic gear. The both shafts are supported by pedestals through ball bearings.

A driven shaft span (a distance between bearing center lines) is adjustable by changing the driven shaft length and a pedestal position in the shaft

axial direction. A shaft center distance (between the two shafts) can be adjusted by moving the assembled driven shaft system in the lateral direction of the shafts with the aid of a slider table.

The specifications of the gears are shown in Table1. The drive gear is made from the steel (JISM0 grade) and has 0.8 modules, number of teeth 60, pressure angel 20ºand gear width 12mm.

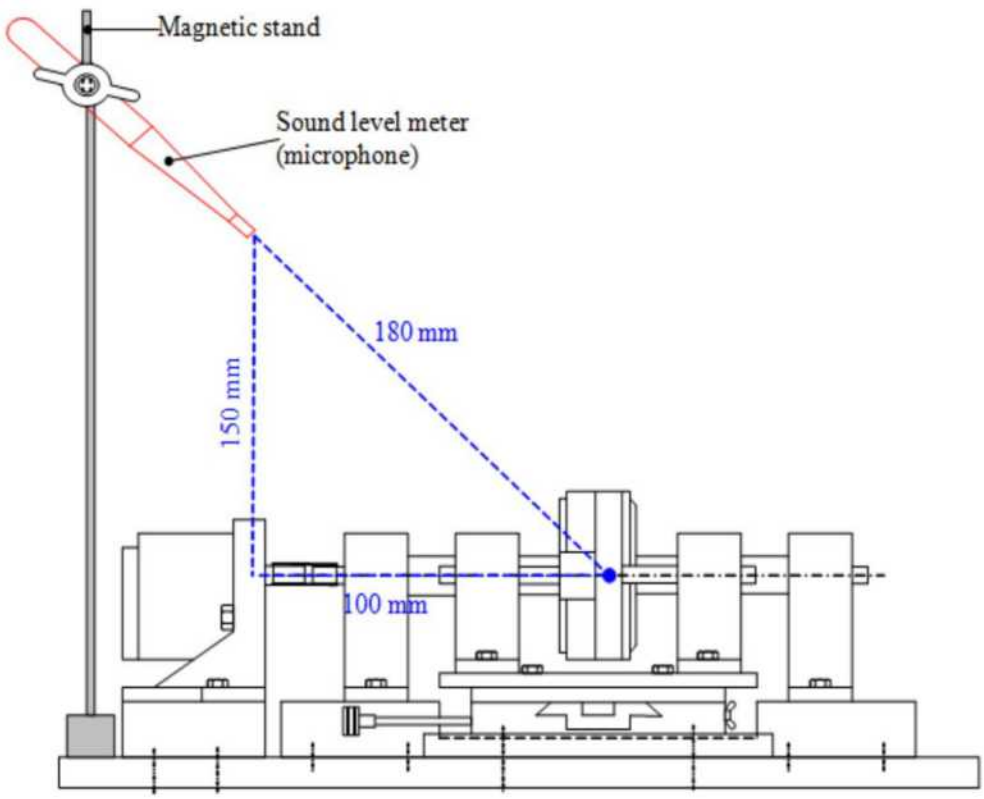

Fig. 1 Experimental apparatus

The material of plastic gears is poly-acetylene resin, the module, pressure angle and numbers of the teeth of the tested gear are the same as the drive gear (precision JISM3 grade).

These systems are connected with Sound Level meter (RION, NL-15) and FFT analyzer, to measure the sound level and noise spectrum of gear. The sound level meter with a microphone position is shown in Fig.2. The microphone position is 180 mm apart from the gear meshing point, 100 mm horizontally and 150mm vertically apart from the point. The sound pressure level [dB (A)] at each rotational speed is measured.

Table 1. Experimental condition

	Drive Gear (master gear)	Driven gear (test gear)
Module (m)	0.8	0.8
Teeth number (z)	60	60
Pressure angle (α)	20°	20°
Material	Steel	Polyacetal
Shaft diameter	12mm	6 mm
Width of teeth (b)	12 mm	5 mm
Bearing expand	80mm	55 mm

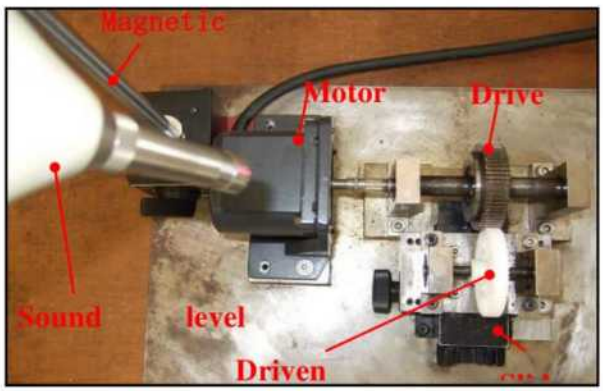

Fig. 2 Photograph of experimental apparatus

spectrum. The magnitude of the peak seems to increase with the rotational speed.

Table 2. Standard experimental condition

Shaft Center Distance : L	48.1 mm
Bearing Span : S	55 mm
Gear Thickness : t	5 mm

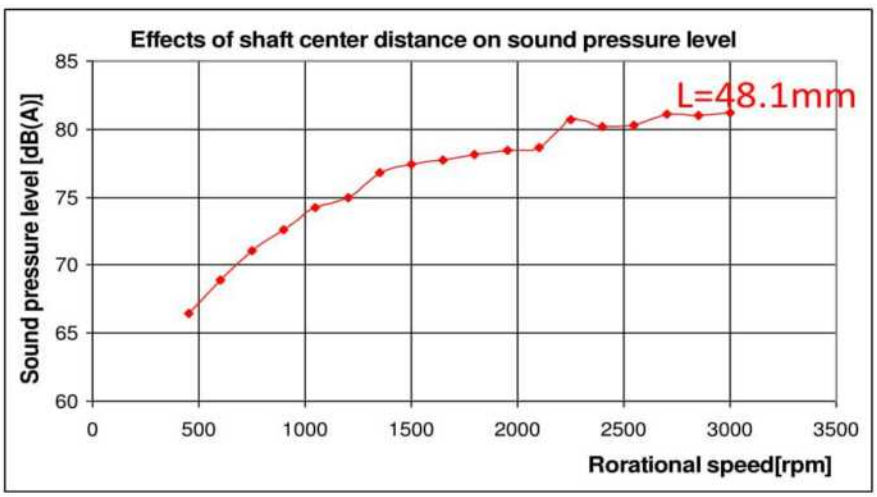

Fig. 3 Change of SPL against rotational speed

3. Typical Experimental Results

3.1 Standard Measurement

The standard experimental conditions are shown in Table 2.A change of the sound pressure level (SPL) obtained under the standard experimental conditions is shown in Fig 3. The SPL increases gradually with the rotation speed and asymptotes to a certain value. A three-dimensional diagram of the frequency analysis (frequency spectrum) of the SPL of the gear system noise at each rotational speed is shown in Fig. 4and is called the cascade plot. There are some remarkable peaks in the frequency

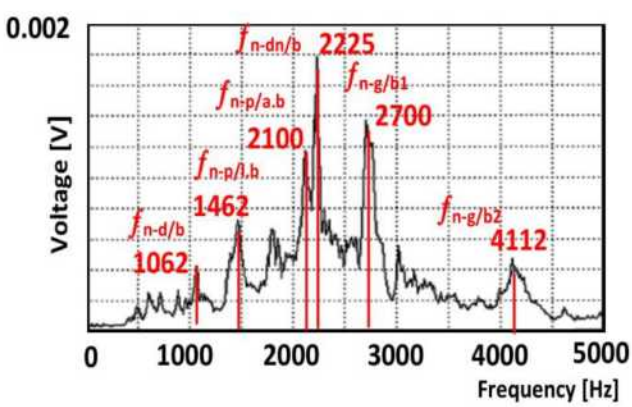

Fig. 4 Over all noise spectrum (L=48.1mm, S=55mm, t= 5mm)

The difference of the SPL at 450rpm and

3000rpm is about 15dB.By using averaging function of the FFT analyzer, all the FFT data obtained during the increase in rotational speed from 450 to 3000rpm are averaged and the result is shown in Fig.4. It is called an overall noise spectrum. This figure is a kind of response curve and the peaks correspond to resonances, where the rotational speed (in rpm) coincides with the natural frequencies of this gear system. The figure shows there are 6 large peaks, 2225, 2700, 2100, 1462, 4112 and 1062 Hz.

3.2 Effects of Shaft Center Distance on the Sound Pressure Level

The shaft center distance L in the three levels of 48.1, 48.4and 48.7mm, bearing span (S=55mm) and gear thickness (t=5mm) were changed as parameters. The rotational speed of the drive shaft is changed from 450rpm to 3000rpm.

Variations of the sound pressure level [dB] for the above three cases are shown in Fig. 5. It is shown that the sound pressure level of the system gradually decreases as the shaft center distance L increases. The sound pressure level (SPL) decreases by 5-8dB corresponding to the change of L. Overall noise spectra are shown in Figs.6(a), (b), (c).

The main frequency components of the noise are 2225, 2700 and 4112 Hz, which correspond to the natural frequencies of the driven shaft, the pedestal axial, and the plastic gear one nodal line bending vibration, respectively. These results seem to indicate that the increase in L makes a meshing excitation force smaller.

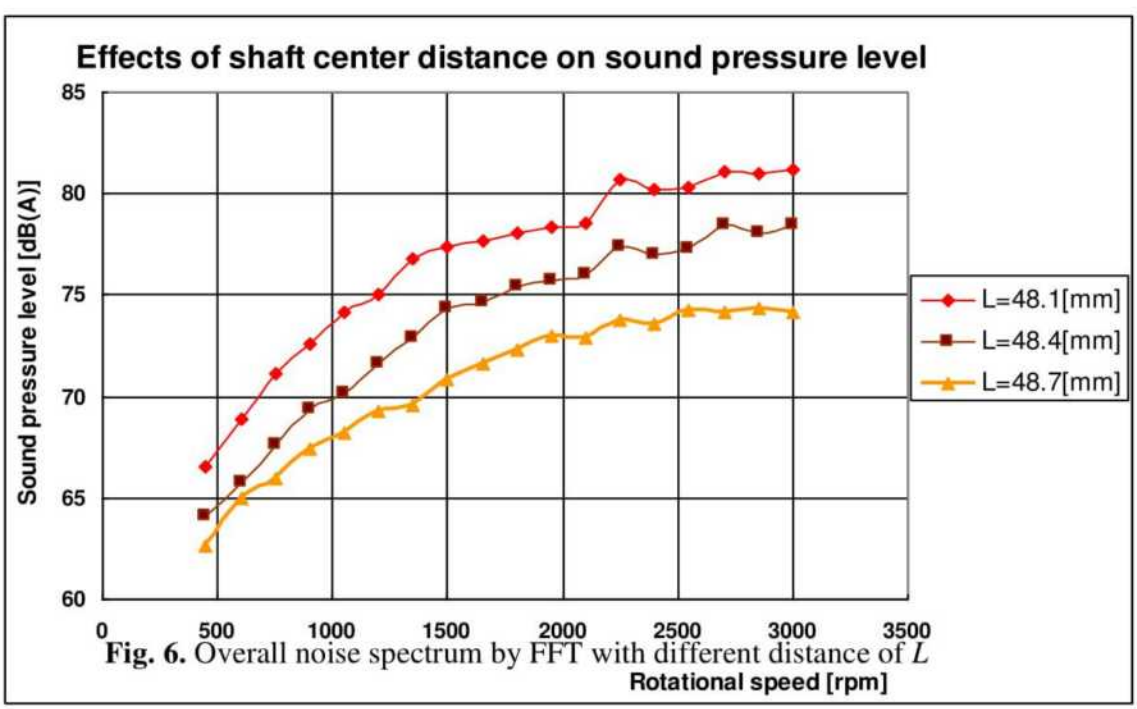

Fig. 6. Overall noise spectrum by FFT with different distance of L

Fig. 5 Effects of the shaft center distance (L)

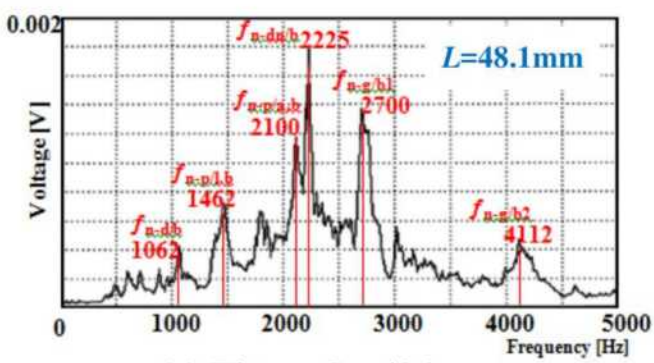

(a). Distance L = 48.1mm

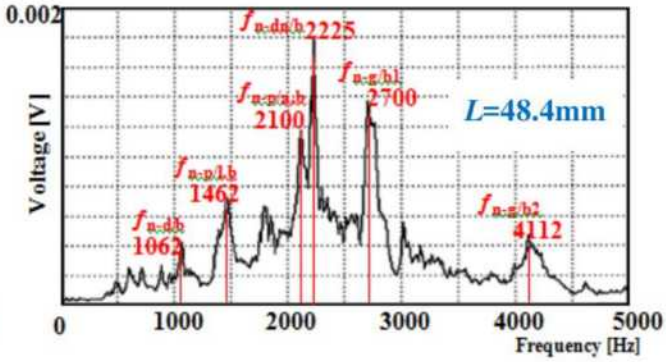

(b). Distance L = 48.4mm

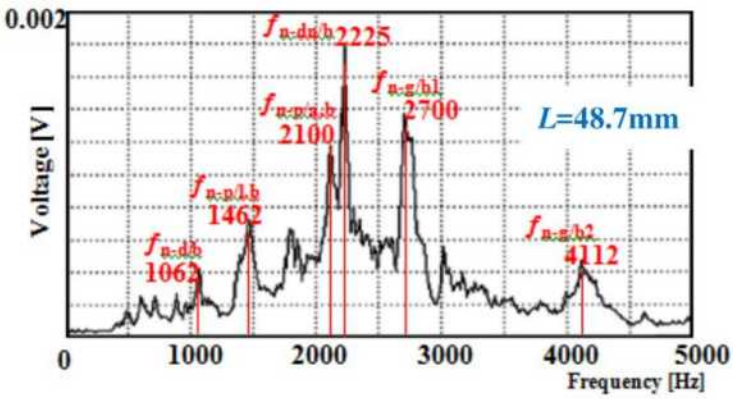

(c). Distance L = 48.7mm

Fig. 6 Overall noise spectrum by FFT

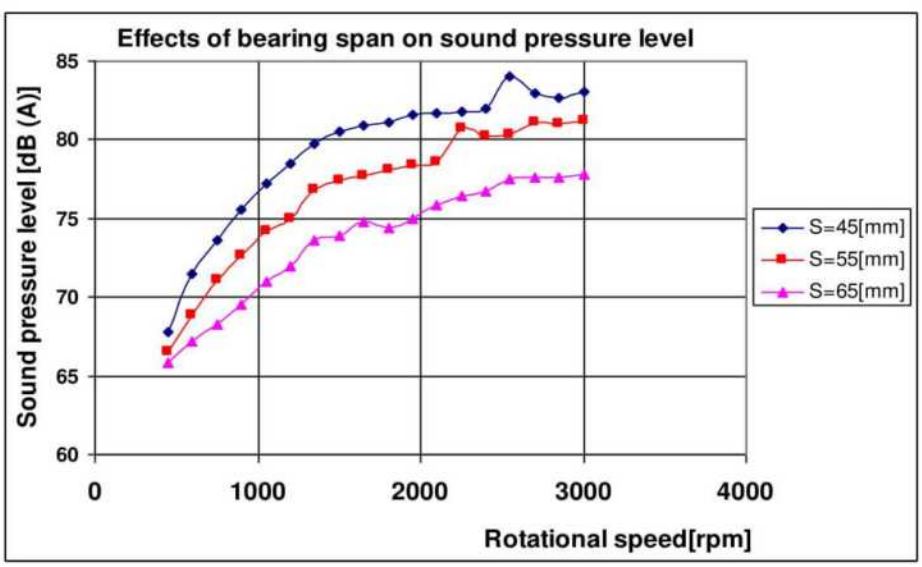

Fig. 7 Effects of bearing span (*S*)

3.3 Effects of Bearing Span on the Sound Pressure Level

Changing the bearing span *S* in the three levels of 45, 55. and 65, the shaft center distance (*L*=48.1mm) and gear thickness (*t* = 5mm). The rotational speed of the drive shaft is changed from 450 to 3000rpm at the constant velocity interval 150rpm.

Variation of the sound pressure level [dB] for the above three cases are shown in Fig 7. As the bearing span of driven shaft *S* increases and sound pressure level of the system gradually decreases.

The sound pressure level (SPL) decreases by 3-6dB due to the change of *S*. Overall noise spectrum are show in Fig 8.(a),(b),(c).The main frequency components are 2225, 2700, and 4112 Hz, which correspond to the natural bending frequencies of the driven shaft, the pedestal axial and the plastic gear one nodal line bending vibration, respectively. The results indicate that the increase in *S* makes a shaft easy to deflect and a meshing excitation force smaller.

4. Conclusions

In this experimental study, noise of a plastic gear system was investigated experimentally. The experimental apparatus was composed of a drive motor, a drive shaft with a steel master gear and a driven shaft with a tested plastic gear. These shafts are supported by pedestals through ball bearings. The system was operated in the speed range of 450~3000rpm under no load conditions.

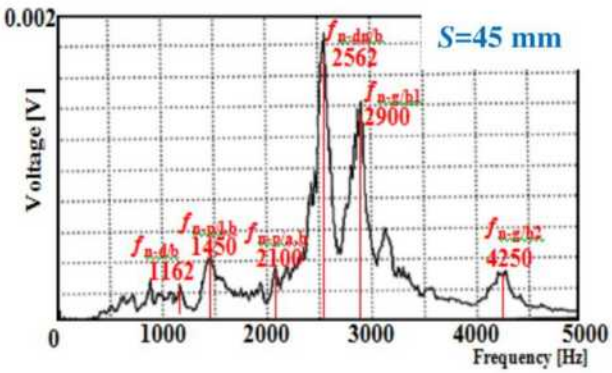

(a). Effects of bearing span(*S=45mm*)

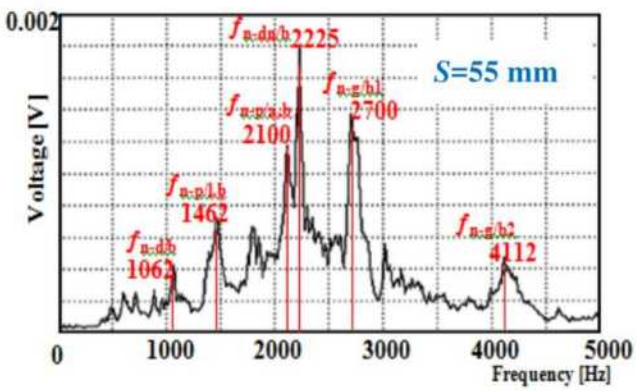

(b). Effects of bearing span(*S=55mm*)

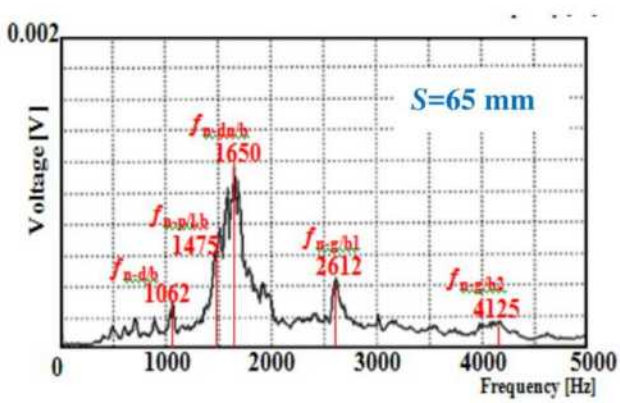

(c). Effects of bearing span(*S=65mm*)

Fig. 8 Overall noise spectrum with different S

The results obtained are summarized below:

1. The SPL of the plastic gear system increases from 67 to 81dB as the rotational speed increases from 450to 3000rpm under the standard experimental conditions.
2. As the shaft center distance increases from 48.1 to 48.7mm, the SPL decreases by 5-8dB.
3. With increasing bearing span of the driven shaft from 45 to 65mm, the natural frequency of the driven shaft decreases from 2560 to 1650 Hz, and the SPL decreases by 3-6dB.

Acknowledgement

The author wishes to thank the JICA CADEFEST project and all Professors from Japanese supporting University. The author also would like to thank all colleagues for supporting my research activity.

References

[1] J. Derek Smith "Gears Noise and Vibration", Second edition, Revised and expanded (Cambridge University, Cambridge –England)

[2] Oogiya, Y. *et.al*, "Noise and Vibration of Plastic Gears for Power Transmission (Influence of Mesh State on Noise Generation)", (MPT symposium, L5171A, Vol.2007, pp.242-245.

[3] KD Dearn and D Walton, "Acoustic Emissions from Polymeric Dears", Proceeding of World Congress on Engineering—2009, Vol. III, London, U.K, July 1-3, 2009.

[4] K. Mani Kandan, Jishuchandran and A. Devaraj, "Characterization of Plastics Gear for Heavy Duty Applications", International Journal of Mechanical Engineering and Technology (IJMET), Vol. 9, Issue 6, pp. 9-13, June 2018.

Case Study of Asphalt Pavement Design in Consideration of Temperature in Timor-Leste

Viegas, H.M.S. [a], Nakashima, S.[b]

[a] *Faculty of Engineering, Science and Technology, Universidade Nacional Timor Lorosa'e, Rua Hera, Cristo-Rei, Dili, Timor-Leste.*
[b] *Department of Civil and Environmental Engineering, Yamaguchi University, Ube, Japan.*

E-Mail: humbelina.viegas@untl.edu.tl.

Abstract: Climatic conditions have a significant influence on the behavior of granular materials and bituminous materials of road pavements. This work presents a study concerning the influence of climatic conditions in Timor-Leste, particularly the temperature influence on the flexible pavements design. This study, after summarizing the behavior of flexible pavements for design purposes and climatic conditions in Timor-Leste, presents a study on the influence of temperature and bitumen stiffness on the structural behavior of a flexible pavement.

Keywords: climatic conditions; Timor-Leste; temperature; flexible pavement; traffic.

1. Introduction

The Timor-Leste is in the process of developing infrastructures. The growth of the road network proves to be important and a priority for the country economic development. This study aims to analyze the influence of temperature on the structural behavior of flexible pavements. The essential function of road surface is to ensure the vehicles to drive comfortably and safely during a pavement life under the action of the traffic in the climatic conditions [1].

This paper considers only flexible pavement since it is usual in Timor-Leste. The flexible pavement is composed of surface course (asphalt concrete), base course (aggregate stabilized with asphalt) and sub-base course (aggregate) as shown in Fig. 1, which is distinguished by their deformability and material constitution.

The main objective of this work is to characterize climatic conditions for the design of pavements in Timor-Leste, and to analyze the influence of temperature on the behavior of elastic modulus of asphalt concrete.

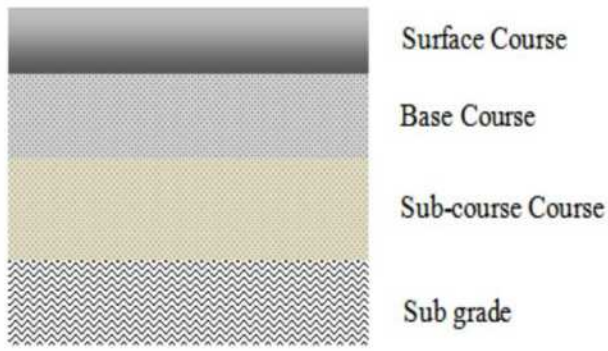

Fig. 1 Basic structure of flexible pavement

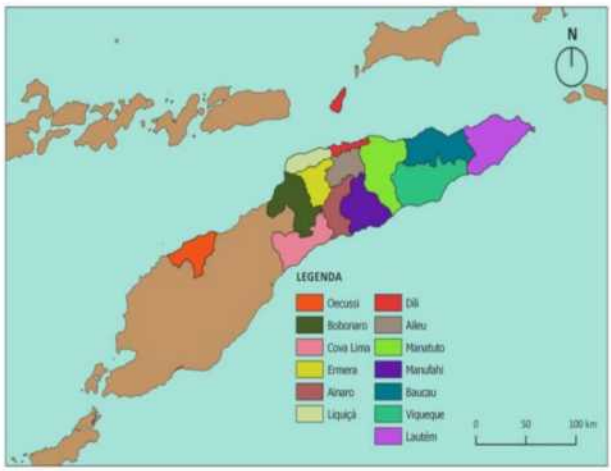

Fig. 2 Map of Timor-Leste

2. Climate Condition in Timor-Leste

Timor-Leste has two seasons, namely, dry and rainy seasons. The climate is tropical, hot and humid [2]. The air temperature considerably varies by region, and it confuses the effect of bitumen temperature and stiffness on the behavior of flexible pavement structure.

First of all, this study collected atmospheric temperature data in Dili and analysed it to obtain the temperature to be used in the pavement design. Fig. 3 shows the annual average atmospheric temperature in Dili between 2003 and 2014. The monthly averaged atmospheric temperature ranges from 28.0 °C in August to 30.4 °C in November. It is noted that the temperature in Dili is relatively constant with no great fluctuation. Based on these data, this case study determined to employ 29.0 °C as the annual averaged atmospheric temperature. Similar to the atmospheric temperature data, this study analyzed the precipitation data between 2003 and 2014 in Dili and found that the monthly mean rainfall was approximately 74 mm varying between 5.2 mm and 162.5 mm. The wettest months are February and December, while the driest months are August and September.

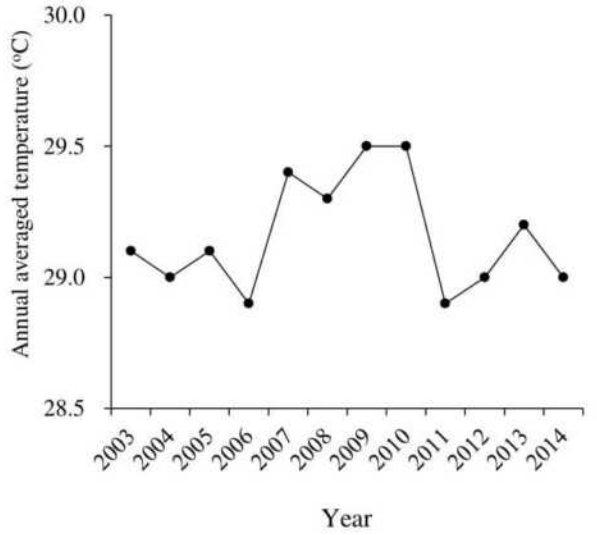

Fig. 3 Annual average temperature in Dili between 2003 and 2014.

3. Design Methodology for Asphalt Pavement

The Shell method [3] and Nottingham method [4] were applied in this study for the pavement design. These methods are known as mechanicstic-emperical pavement design methods. They control horizontal tensile strain on the bottom of asphalt concrete and vertical compressive strain on the subgrade surface to prevent from fatigue cracking and rutting.

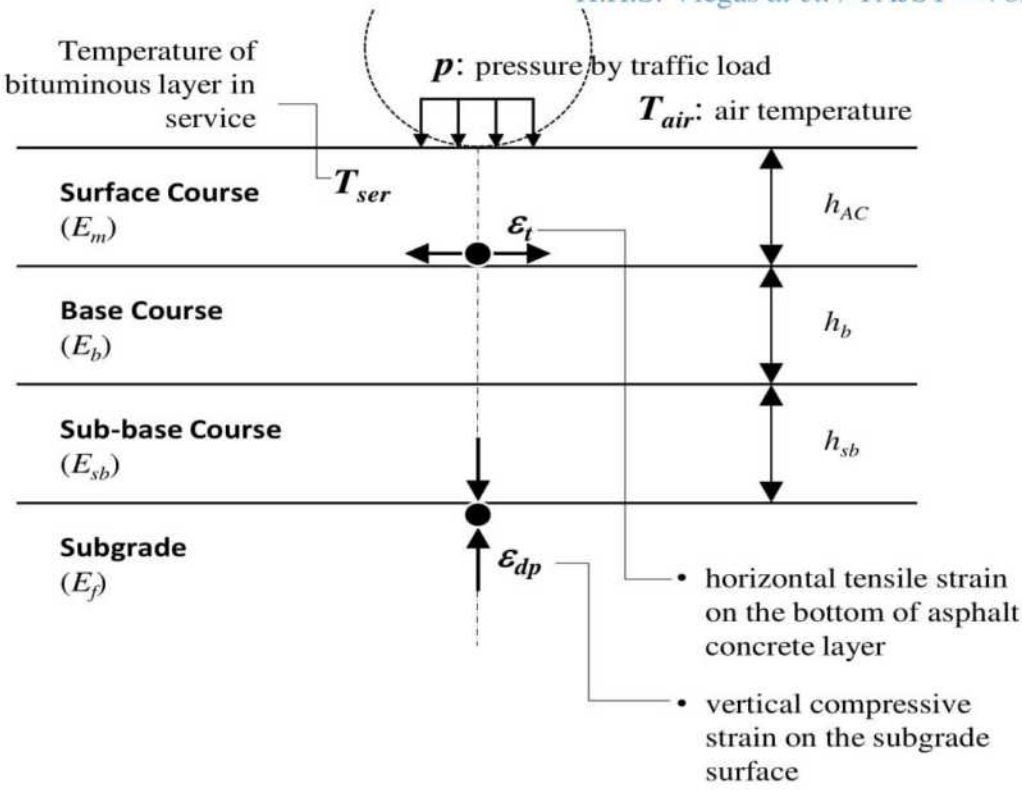

Fig. 4 Constitution and actions of road pavement

The process of our pavement design is as follows:

(1) Calculation of Axle Loads in the Pavement Design Life

The cumulative number of axle load that the pavement is subjected to over its design period is calculated by the following equation. This study considers the axle load of N_{80}, the number of 80 kN equivalent single axle load (ESAL).

$$N = A_0 \times 365 \times \sum_{i=0}^{n-1} (1+t)^i \times d \times f \qquad (1)$$

where:

N = cumulative number of 80 kN equivalent single axle loads;
A_0 = first year annual average daily traffic (AADT) for total lanes;
t = annual traffic growth;
n = design period in year;
d = lane distribution factor;
f = vehicle damage factor.

(2) Assumption of the Pavement Structure

As an initial condition of structure, material and thickness of each layer is assumed.

(3) Calculation of Elastic Moduli of Granular Layers, E_f, E_{sb} and E_b

Elastic moduli of subgrade (E_f), subbase course (E_{sb}) and base course (E_b) are estimated. E_f [MPa] is determined from the material test result for subgrade soil, namely CBR [%], California Bearing Ratio test, using the following empirical relationship.

$$E_f = 10 \times \mathrm{CBR} \qquad (2)$$

E_{sb} and E_b [MPa] are estimated in order from lower layer to upper layer using the following empirical relationship.

$$E_{sb} = E_f \times 0.2h_{sb}{}^{0.45} \quad (3)$$

$$E_b = E_{sb} \times 0.2h_b{}^{0.45} \quad (4)$$

Where: h_{sb} and h_b are thicknesses of sub-base course and base course in millimeters, respectively.

(4) Calculation of Elastic Modulus of Asphalt Concrete, E_m

Elastic modulus of surface course (E_m), namely elastic modulus of asphalt concrete layer, is calculated from bitumen stiffness (S_b) and voids in mineral aggregates (VMA) using the following Nottingham method [4].

$$E_m = S_b \left[1 + \frac{257.5 - 2.5VMA}{n\,(VMA - 3)}\right]^n \quad (5)$$

$$n = 0.83 \log \frac{4 \times 10^4}{S_b}$$

where:

E_m = elastic modulus of asphalt concrete [MPa]

S_b = bitumen stiffness [MPa]

VMA = voids in mineral aggregate [%]

The bitumen stiffness (S_b), under a given loading time (t_c), at a temperature in service (T_{ser}), can be determined from Fig. 5, a well-known nomogram by Van der Poel [5], using the material test result of bitumen, namely, softening point (T_{ab}) and penetration index (I_{pen}) of bitumen.

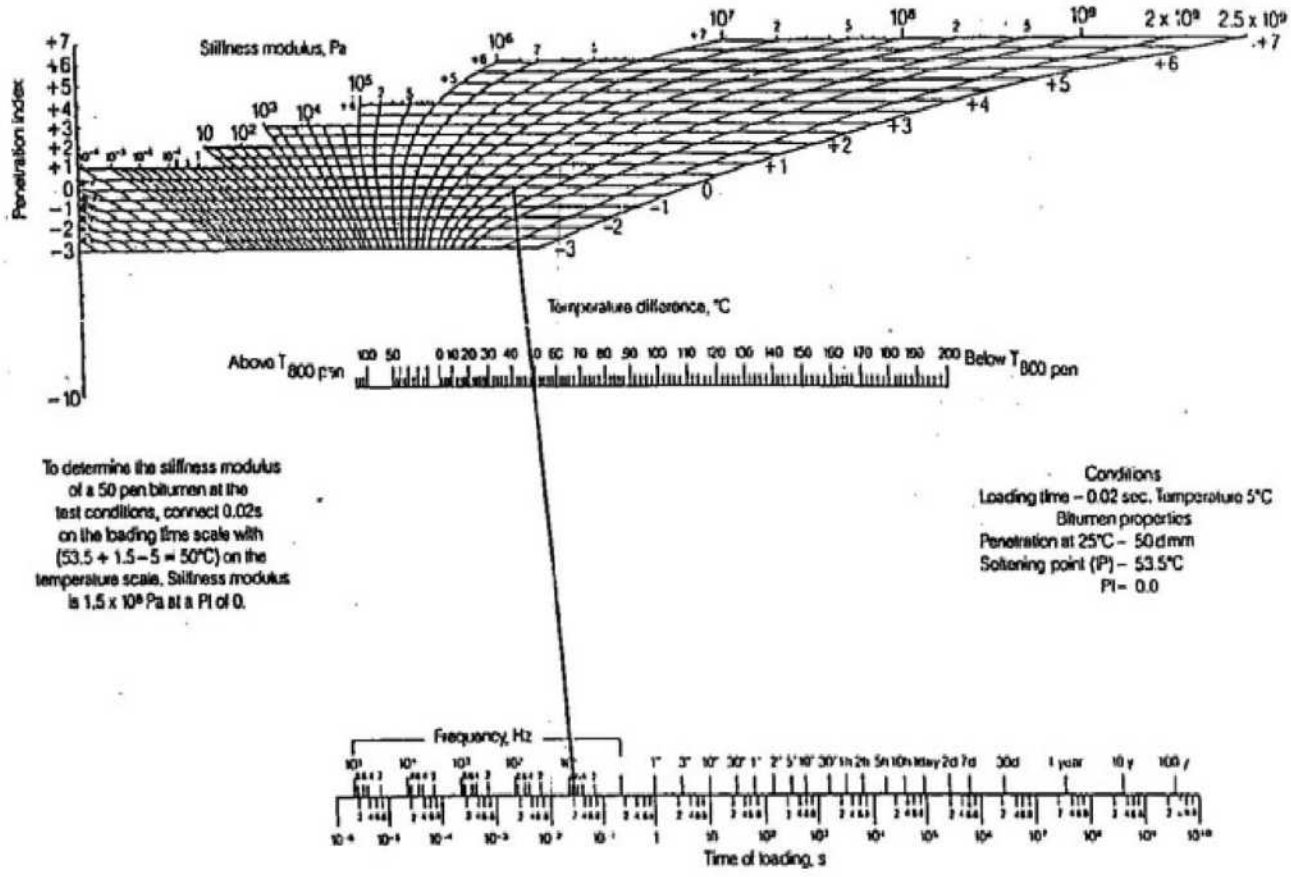

Fig. 5 Nomogram by Van Der Poel for determination of bitumen stiffness, S_b [5].

However, this study estimates S_b using the following simplified equation [6], which was derived from Fig. 5.

$$S_b = 1.157 \times 10^{-7} t_c^{-0.368} \times 2.718^{I_{penr}} \times (T_{abr} - T_{ser})^5 \quad (6)$$

provided that 0.01s < t_c < 0.1s, -1.0 < I_{penr} < 1.0, and 20 °C < T_{abr} - T_{ser} < 60 °C.

The input parameters in Eq. (6) are obtained from the followings:

$$t_c = 2r/V \quad (7)$$

$$I_{penr} = \frac{27 \log(pen25) - 21.65}{76.35 \log(pen25) - 232.82} \quad (8)$$

$$T_{abr} = 99.13 - 26.35 \log(0.65\, pen25) \quad (9)$$

Where:

t_c = loading time [sec];

r = loading radius [m];

V = average speed of traffic [km/h];

I_{penr} and T_{abr} = penetration index and softening point of bitumen modified in consideration of hardening in the manufacturing and construction process;

$pen25$ = penetration of bitumen at 25 °C.

The temperature of asphalt concrete in service (T_{ser}) in Eq. (6) is determined by Fig. 6 using the monthly averaged atmospheric temperature (T_{MMA}).

(5) Multi-layer Pavement Structural Analysis

Using the assumed thicknesses in Section (2) and the determined elastic moduli in Sections (3) and (4), the multi-layer pavement structural analysis is carried out.

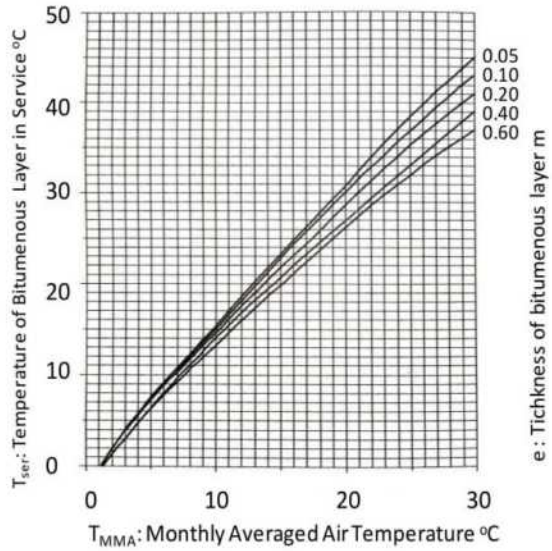

Fig. 6 Temperature of the bituminous layers in service (T_{ser}) [2]

This study used commercial software, Alize-LCPC (www.alize-lcpc.com) for the analysis. From the calculation results, horizontal tensile strain on the bottom of asphalt concrete layer (ε_t) and vertical compressive strain on the subgrade surface (ε_{dp}) are extracted, because these two strains represents mechanical performance of the pavement against fatigue cracking and rutting, respectively. The admissible number of cumulative standard single axle loads in respect to fatigue cracking and rutting, N_c and N_{dp}, respectively, can be estimated using the following Shell empirical equations.

$$N_c = (K/\varepsilon_t)^{0.2} \quad (10)$$

$$N_{dp} = \left(k_s/\varepsilon_{dp}\right)^{0.25} \quad (11)$$

Where:

N_c = admissible number of cumulative standard single axle load [millions];

K = coefficient depending on volumetric percentage of bitumen in asphalt concrete (V_b [%]) and elastic modulus of asphalt concrete (E_m [MPa]), as $K = (0.856\, V_b + 1.08)\, E_m^{-0.36}$;

ε_t = computed horizontal tensile strain on the bottom of asphalt concrete layer;

N_{dp} = admissible number of cumulative standard single axle load [millions];

k_s = coefficient depending on the probability of survival ($k_s = 1.8\times10^{-2}$ for 95 % survival was used in this study).

(6) Comparison of N_c and N_{dp} with N

Finally, N_c or N_{dp}, whichever is smaller, is employed as the mechanical performance of the assumed pavement structure (N' = min (N_c, N_{dp})), and it is checked whether N' satisfies the following range in relation to the requested traffic loads, N, which is estimated in the Section (1).

$$N = (80\%\sim100\%) \times N' \quad (12)$$

If N is less than 80% of N', the assumed pavement structure, namely pavement materials and/or thickness, is judged as oversize. On the other hand if N is larger than 100% of N', the design is judged as undersized.

4. Calculation Conditions

Considering several cases, this study analyzed the structure of asphalt pavement. The basic structure is illustrated in Table 1. For multi-layer pavement structural analysis, Alize-LCPC was used.

5. Calculation Results and Discussion

This study chose bitumen of 60/70 as the basis, because it is customary and usual application in hot countries like Timor-Leste.

Table 1 Design parameters

Climatic condition	
Air temperature, T_{MMA}	29.0 °C
Loading condition	
Standard axle load	80 kN
Loading radius, r	0.105 m
Traffic speed, V	50 km/h
Subgrade	
CBR	8 %
Poisson's ratio	0.45
Sub-base course	
Thickness, h_{sb}	20 cm
Poisson's ratio	0.35
Base course	
Thickness, h_b	20 cm
Poisson's ratio	0.35
Asphalt concrete	
Thickness, h_{AC}	10, 15 cm
Poisson's ratio	0.40
Bitumen class	60/70, 20/30, 10/20
Fatigue parameter, K	3.2×10^{-3}, 3.6×10^{-3}
Rutting parameter, k_s	1.8×10^{-2}
Voids in mineral aggregate, *VMA*	?? %

(1) Mecanical Characteristics of Pavement Materials

The elastic moduli of subgrade, sub-base course and base course are determined as E_f = 80 MPa E_{sb} = 170 MPa and E_b = 375 MPa, respectively, based on the Eqs. (3) to (5).

As for bitumen stiffness, this study considers the annual average daily temperature at Dili drawn in the Section 2, namely T_{MMA} = 29.0 °C. The stiffness values for three kinds of bitumen are indicated in Table 2. For the calculation of S_b, a loading time of t_c = 0.02s was chosen, considering value rounded by excess (at th side of safety) of 0.015, which corresponds to the speed of V = 50 km/h.

Table 2 Stiffness of the bitumen 10/20, 20/30, and 60/70, Dili (T_{MMA} = 29°C)

Bitumen class	10/20	20/30	60/70
T_{ser} (°C)	40	40	40
t_c (s)	0.02	0.02	0.02
*Pen*25 (dmm)	15	25	65 [7]
$Pen25_r$ (dmm)	9.75	16.3	42.3
T_{ab} (°C)	69.5	59	48 [7]
T_{abr} (°C)	73.1	67.2	56.3
I_{pen}	0.17	0.7	-1.15
I_{penr}	-0.07	-0.128	-0.289
S_b (MPa)	38	32	20

Table 2 shows the results of bitumen stiffness S_b of the classes 10/20, 20/30 and 60/70, using Eq.(6). S_b for bitumen 10/20 is greater than that for 60/70 at the same temperature. The elastic modulus of asphalt concrete E_m, results in 4400 MPa for bitumen 60/70 from Table 2 and Eq. (5).

(2) Result and Discussion

Based on the calculation results, influence of temperature and elastic modulus of asphalt concrete on pavement behaviour is discussed.

Fig. 7 shows the admissible number of standard axle load for fatigue cracking and rutting criteria, N_c and N_{dp} against elastic modulus of asphalt concrete, E_m. From this figure, it is confirmed that the admissible axle number for fatigue cracking criterion, N_c, is less than that for rutting criterion, N_{dp}. This means that the fatigue cracking at the bottom of the asphalt concrete layer is dominant under this calculation condition ($N' = N_c$).

Fig. 8 shows the admissible number of axle load in respect to fatigue cracking, N_c for different K value. It is noted from this figure that the larger K is, the larger number of axle load is admissible, for the same E_m.

Fig. 9 shows the admissible number of axle load, N', for different thickness of asphalt concrete, h_{AC}.

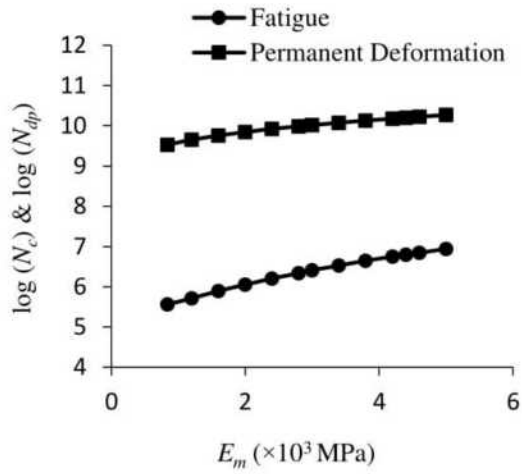

Fig. 7 Relation of elastic modulus of asphalt concrete, E_m vs admissible number of axle load, N_c and N_{dp} ($K = 3.2\times10^{-3}$).

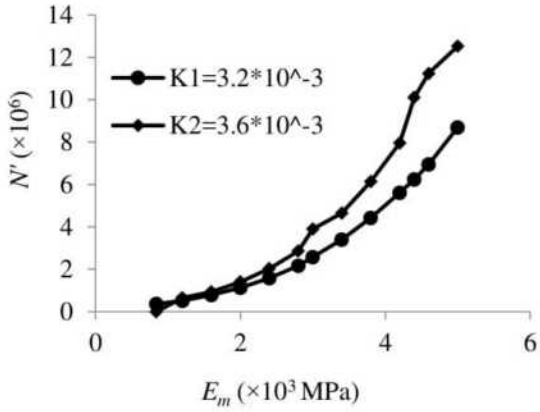

Fig. 8 Relation of elastic modulus of asphalt concrete, E_m vs admissible number of axle load N' (influence of different K).

Fatigue is dominant criterion for the both cases ($N' = N_c$). This graph means that 5-cm increase in pavement thickness gives remarkable influence on long-life of pavements. It is also stated that slight increase in pavement stiffness gives large influence when pavement is thicker.

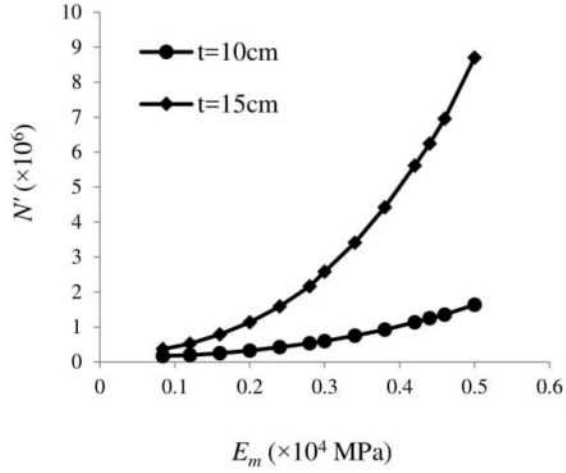

Fig. 9 Relation of elastic modulus of asphalt concrete, E_m vs admissible number of axle load N' (influence of pavement thickness) (K = 3,2×10^{-3})

Fig. 10 shows relationship between admissible axle load number, N' and the temperature in service, T_{sr}. It can be seen in this figure that softer bitumen (60/70) is less susceptible to temperature and that harder bitumen (10/20) makes the pavement durable in the case of lower temperature (20 °C).

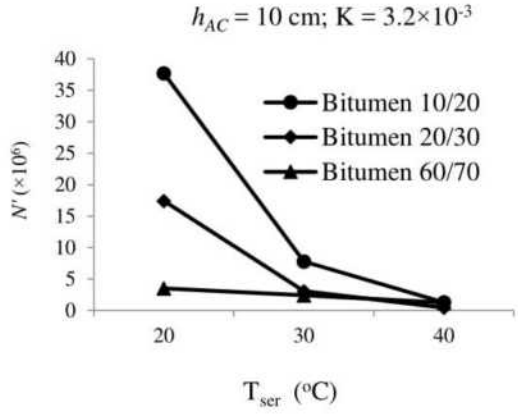

Fig. 10 Relationship of admissible axle load, N' vs temperature in service, T_{ser}

Figure 11 shows variation of the admissible number of axle load with elastic modulus of asphalt concrete for bittumen 60/70, 20/30 and 10/20. From this figure, it is verified

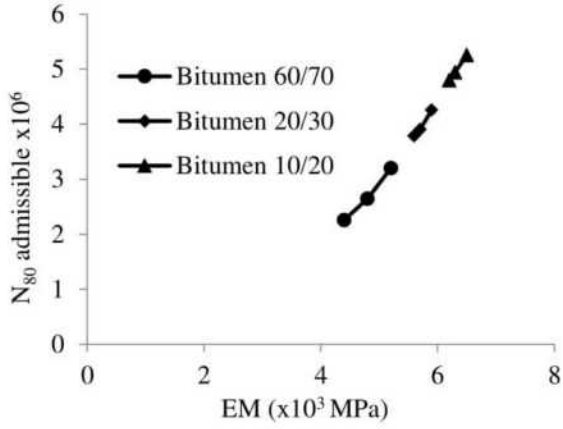

Fig. 11 Variation the allowable number of axle load with elastic modulus of asphalt concrete, for bitumen 60/70, 20/30, and 10/20, T_{ser} = 40 °C

that the modulus of deformability of the mixture is higher in the bitumen 10/20 than in the bitumen 60/70 and 20/30, for the same operating temperature.

6. Conclusions

The main conclusions of the parametric study are presented below:

1) The higher the average annual temperature, the higher the temperature in service the bituminous layer of the pavement and the smaller the stiffness modulus of the bitumen and the deformability of the bituminous mixture.
2) The lower the deformability modulus of the bituminous layer, the greater the allowable tensile and compressive extension.
   With increasing thickness and modulus of deformability, there is increase in N_{80} number permissible.
3) For the variation of parameter K (K = 3.2 × 10^{-3}; K = 3.6 × 10^{-3}), the larger K, the greater the permissible number of N_{80}. With respect to the various types of bitumen, 10/20, 20/30 and 60/70, it has been found that the harder bitumen corresponds to generally higher

deformability modules at the same temperature.

References

[1] Branco, F., Pereira, P. and Santos, L.P., "Pavimentos Rodoviários", Almedina, 2011.

[2] Goverment of Timor-Leste. April 2016, [Online] Available URL: http://timor-leste.gov.tl/.

[3] Claessen, A.I.M., Edwards, J.M., Sommer, P. and Uge, P., "Asphalt pavement design - The Shell method", in Proc. the 4th International Conference on the Structural Design of Asphalt Pavements, pp. 39-74, 1977.

[4] Brown, S., "Material characteristics for analytical pavement design, Developments in Highway Pavement Engineering", Vol. 1, pp. 41-92, 1978.

[5] Van der Poel, C., "A general system describing the visco-elastic properties of bitumens and its relation to routine test data", Journal of Applied Chemistry, Vol. 4, pp. 221-236, 1954.

[6] Ullidtz, P., "A fundamental method for the prediction of roughness, rutting and cracking in asphalt pavements", in Proc. Association of Asphalt Paving Technologists, 48, 1979.

[7] Palha Carlos., "Misturas Betuminosas, Betumes", Civil Uminho, 2008.

Simple Numerical Analysis on Road Pavement Condition Assessment (RPCA) as Maintenance Strategy

Hugo Ximenes

Road and Transportation Laboratory, Department of Civil Engineering, Faculty of Engineering, Science, and Technology, Universidade Nacional Timor Lorosa'e, Avenida Hera Cristo-Rei, Dili Timor Leste

E-mail: hugo.ximenes@untl.edu.tl

Abstract: The establishment of a vast network of infrastructure by the government of Timor-Leste is urgent issue to facilitate the growing economy. The network of infrastructure includes a well-established, large and complex road network under construction. This study is to formulate a manual road condition assessment for evaluating the condition of a pavement whether a road pavement needs repairs/and maintenance.

Keywords: road maintenance, Timor-Leste road network, manual road maintenance

1. Introduction

Timor-Leste is one of the least developed countries in the region. The poor condition of basic road network, in particular, remains a key constraint. In a transport sector study commissioned by the Asian Development Bank in 2014, the poor condition of the roads was cited by the interviewed households as the major cause of poverty and the largest constraint to local economic development.

The government of Timor-Leste has committed to the development and improvement of a well-connected and coherent road network [1]. On the other hand, the design service life of the existing roads soon will be elapsed, hence the large number of roads in the network have started to deteriorate due to over loading and weathering [2]. Therefore, maintenance and repair of these roads should be a great and urgent. There is a high demand for a systematic and, cost-effective road maintenance [3]. The most important and first step to meet such a demand is an effective and efficient road condition assessment whether a road needs repairs/and maintenance. It needs a special skill to formulate a reasonable system. This study is to acquire knowledge that should be used to formulate a basic understanding as to the manual measurement for a road pavement condition assessment.

2. Terminologies and Fundamental of RPCA

2.1 Terminologies

The Manual RPCA parameterizes on the three road damages phenomenom, which are crack rate (%), rut depth [mm] and longitudinal roughness [mm], and evaluates the condition of the maintenance or repairs of the road [4]. Crack rate is a measure of road cracking, rut depth is a measure of road rutting and logitudinal roughness is the

measure of the longitudinal vertical displacement of the road profile from the reference line. Figure 1 shows an example of road cracking.

Fig.1 Line cracking

2.2 Fundamental

The manual RPCA calculated using equations that were developed using Regression anylsis from microsoft Excel. In order to understand the development of the equations, 1000 data of road evaluation value are extracted of one of the progress reports made during the manual measurement. The three road damages were measured; cracking was measured as crack rate (%), rutting is measured as rut depth (measured in mm) and longitudinal roughness is measured as standard deviation of the longitudinal deviations (measured in mm) of the road profile from a reference line.

The road engineer made subjective evaluation and correlated with the objective measurements of the three road damages phenomenon (crack ratio, rut depth and longitudinal roughness) on a selected road.

3. Numerical Analysis Application on Manual RPCA

The numerical analysis will apply to each road damages phenomenon (crack ratio, rut depth and longitudinal roughness) in order to devise a basic formula [4, 5]. This stage also will define a type of damage and how to get the judgment of an engineer from a manual road measurement and survey in the field.

3.1 Cracking and Measurement of Crack Rate (%)

There are three main types of cracking, fatigue cracking, line cracking and patched-area cracking [4, 5].

The lines cracking is cracking one in the direction flow of traffic, which is caused by pressure exerted on the road by the car tires. Figure 1 shows the line cracking. On the other hand, the fatigue cracking is an interconnected cracking with a net-like pattern. Fatigue cracking is mainly caused by heavy traffic flow, repeated traffic flow, and an unstable base of the road profile due to poor construction. Figure 2 shows fatigue cracking.

Fig. 2 Fatigue cracking

Patched-area cracking, on the other hand, is caused by road repairs which are usually carried by patching holes that have developed or yet to develop in the road structure. This involves filling the holes with a mixture of bitumen and stone. Figure 3 shows patched-area cracking.

3.2 Measurement of Crack Rate

Crack rate is measured in percentage and represented by symbol *C*. The measurement can be obtained manually by grid method. In

this research, the grid method is illustrated using on Figure 4.

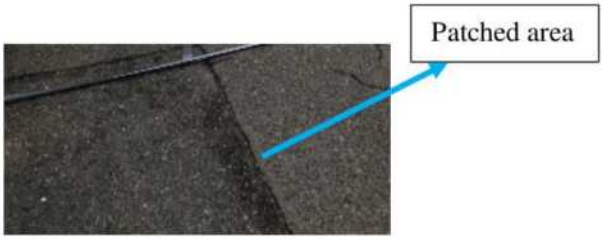

Fig. 3 Patched-area cracking

The road section is divided into imaginary 0.5m square grids, and the line cracking covers 6 grids, fatigue cracking covers 9 grids and patched-area cracking covers 4 grids [4, 5]. Hence the total cracking area was obtained as;

Therefore, the Total cracking area (m^2) = line cracking area (m^2) + fatigue cracking area (m^2) + patched cracking area (m^2)

Hence, the Eq. (1) is used to determine the crack rate.

$$C = \frac{\text{Total cracking area}(m^2)}{\text{area of road section}(m^2)} \times 100\% \qquad (1)$$

where C is crack rate in percentage.

3.3 Rutting and Measurement of Rut Depth

Rutting is the transverse vertical displacement of the road profile from a reference line. The displacement is caused by the wheel of the vehicle due to repeated flow of traffic. There are two basic types of rutting; mix rutting and subgrade rutting. Mix rutting occurs when subgrade does not rut yet the road surface exhibits wheel-path displacements due to improper compaction of

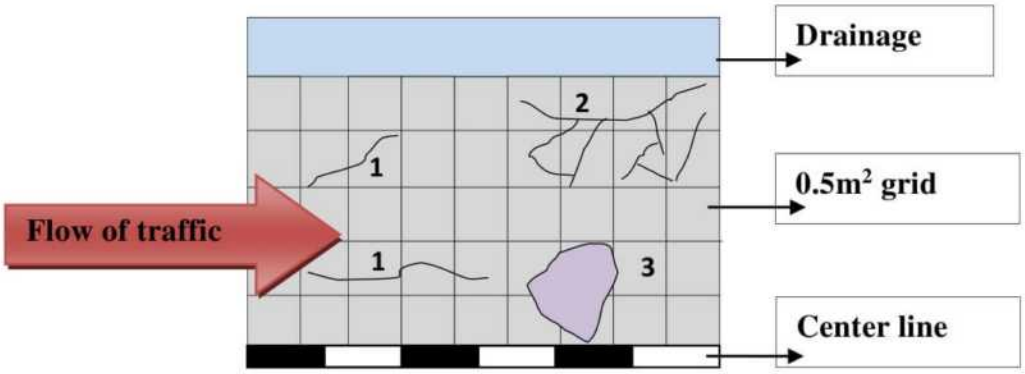

Fig. 4 Illustration of road section with imaginary grids

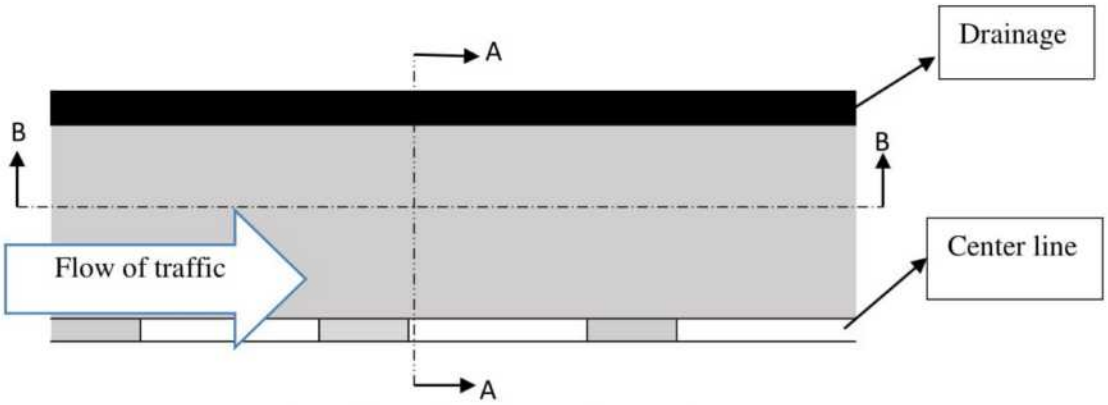

Fig. 5 illustration of a one-lane road

1) Line cracking area: 6 x 0.15m^2

2) Fatigue cracking area: 9 x 0.25m^2

3) Patched cracking area: 4 x 0.25m^2

Fig. 6 Transverse cross section A-A of the road

road profile layers during construction. Subgrade rutting occurs when the subgrade of the road profile is displaced by loading from the wheel of the repeated traffic flow.

3.4 Measurement of Rut Depth

Rut depth is measured in mm and represented by symbol D (mm) [4, 5].

The measurement is obtained manually by measuring the vertical displacement of the road profile based on the transverse cross section of the road profile [4, 5].

In this report the manual method was illustrated in Figure 5. Under the manual method there are two methods of measurement; the maximum method and the average method. Figure 6 is an illustration of a one-lane road.

The maximum method is normally applied to highway roads. The rut depth D is obtained as the maximum value amongst the vertical displacements (d_1, d_2, d_3, d_4, d_5, d_6) of the road profile from the reference line, where d is the Transverse vertical displacement of road profile measured in (mm).

On the other hand, the average is normally applied to non-highway roads. The rut depth D is obtained by calculating the average of the vertical displacements (d_1, d_2, d_3, d_4, d_5, d_6) of the road profile from the reference line.

On the other hand, the average is normally applied to non-highway roads. The rut depth D is obtained by calculating the average of the vertical displacements (d_1, d_2, d_3, d_4, d_5, d_6) of the road profile from the reference line.

The Eq. (2) is the rut depth D.

$$\boldsymbol{D = \frac{d_1+d_2+d_3+d_4+d_5+d_6}{6}} \qquad \textbf{(2)}$$

3.5 Longitudinal Roughness and Measurement

Longitudinal roughness is the longitudinal vertical displacement of the road profile from the reference line, which is measured in (mm) and represented by symbol σ (mm) [4, 5]. The measurement is performed automatically by a profile-meter that measures the vertical displacement of the road profile.

This measurement divides into 500 m in each section, thus it splits into 100 m to get the roughness data. It requires a minimum of 100 data for representing a roughness condition in each section.

Figure 7 is a longitudinal cross- section B-B shown in Figure 5,

Hence, the longitudinal roughness can be calculated as

$$\boldsymbol{\sigma = \sqrt{\frac{\left[\sum_{i=1}^{n} (d_i')^2 - \frac{(\sum_{i=1}^{n} d_i')}{n}\right]}{n-1}}} \qquad \textbf{(3)}$$

where; $\boldsymbol{i = 1, 2, \ldots n}$, n : Number of data, d' : Longitudinal vertical displacement of road profile, and σ: Longitudinal roughness (mm).

4) Practical Application and Data Analysis of Manual RPCA

This research was conducted on Akanunu-Dili road located in Fatuahi as shown in Fig. 8. The targeted road categorizes Arterial type connecting Dili center to the Dili suburb areas with the total distance 4.5 km. This research was conducted in a day with the finalist student, starts from 9am – 5pm as shown in Fig. 9.

The objective is to apply the numerical analysis on RPCA for evaluating its effectiveness.

Fig. 8 Targeted route map

4.1 Condition Assessment Process

The data collection was conducted manually by using a 50m tape measuring, a 0.3m ruler for measuring the rut depth and a digital camera for taking the picture of each point. The measurement starts from Dili (Becora) as start point and it ends in Akanunu. The total distance of targeted road was divided longitudinally in every 100m. Meanwhile, the identification of damage parameters such as cracking, rutting and surface roughness classified transversally in both left and right side of the road lane.

4.2 Numerical Analysis of RPCA on Targeted Road

The route was divided into nine divisions, with the length 500 meters each. This is to facilitate the road engineer to identify the phenomenon of damages in each division easily.

Table 1 summarized the numerical analysis of RPCA for cracking damages occurred on the targeted route, which were calculated by using Eq. (1).

It shows the percentages of total crack rate of each section. The rutting condition also can be seen in Table 2. The Eq. (2) was applied for calculating the data. The data indicate that the rutting phenomenon is occurring. However, the average value is still in moderate condition. On the other hand, the evaluation result for surface roughness was also calculated by using Eq. (3) the result of data analysis is in Table 3. The outcome of the data indicates longitudinally distorted on the pavement surface. Nevertheless, the condition of targeted route is fairly safe.

Fig. 9 Measurement on targeted route

Table 1. Numerical analysis of cracking data

No	Distance (m)	Damages penomenon	Section		Coefficient	Cracking %)
			Left	Right		
1	500	Cracking (line)		R	0.15	8.50
			L			
2	500	Cracking (line)		R	0.15	8.63
			L			
3	500	Cracking (Fatigue)		R	0.25	18.98
			L			
4	500	Cracking (Fatigue)		R	0.25	8.50
			L			
5	500	Cracking (Fatigue)		R	0.25	7.86
			L			
6	500	Cracking (patched)		R	0.25	15.93
			L			
7	500	Cracking (patched)		R	0.25	13.31
			L			
8	500	Cracking (line)		R	0.15	9.13
			L			
9	500	Cracking (line)		R	0.15	9.17
			L			
Total Cracking (%)						100.00

Table 2. Numerical analysis of rutting data

No	Distance (m)	Damages phenomenon	Section		Total Area (m^2)		Depth (mm)				Rutting (mm)
			Left	Right	Length (m)	Width (m)	d_1	d_2	d_3	d_4	
1	500	Ruting		R	0.5	0.1	1	2	2	2	1.75
			L		3.2	0.08	6	5	5	6	5.50
2	500	Ruting		R	1	0.5	7	8	7	7	7.25
			L		0.8	0.3	7	8	7	7	7.25
3	500	Ruting		R	3.5	0.05	5	8	5	5	5.75
			L		3.6	0.1	2	1	2	2	1.75
4	500	Ruting		R	0.4	0.1	2	1	1	2	1.50
			L		1.1	0.3	4	5	5	4	4.50
5	500	Ruting		R	0.2	0.8	7	6	7	7	6.75
			L		6	0.4	7	5	6	7	6.25
6	500	Ruting		R	0.4	0.08	3	4	5	3	3.75
			L		1.9	0.8	5	4	5	5	4.75
7	500	Ruting		R	1.5	0.6	2	5	2	2	2.75
			L		0.7	0.3	2	2	2	2	2.00
8	500	Ruting		R	0.6	0.2	1	1	1	1	1.00
			L		0.5	0.5	6	6	6	6	6.00
9	500	Ruting		R	3	0.2	3	3	3	3	3.00
			L		0.9	0.2	5	5	5	5	5.00

4.3 Discussion

The Numerical analysis of RPCA application to Dili-Hera road was conducted to justify its effectiveness, particularly the maintenance work with a limited budget. It was used three phenomena of road damages *cracking, rutting and surface roughness*. However, the alternatives included *water runoff management and slope stability* needs to be considered in order to provide a long life entirely service of a road. Furthermore,

Table 3. Numerical analysis of surface roughness data

No.	Distance (m)	Damages phenomenon	Section		Total area (m²)		σ (mm)
			left	right	length (m)	width (m)	
1	500	Roughness		R	7		0.966068
			L		8.5		
2	500	Roughness		R	5		1.030568
			L		0.9	0.08	
3	500	Roughness		R	2.3	0.05	1.173669
			L		8.6	0.1	
4	500	Roughness		R	2.5	0.09	0.996339
			L		6.9	0.07	
5	500	Roughness		R	1.2	0.08	0.958919
			L		1.2	0.06	
6	500	Roughness		R	1.3	0.07	0.896092
			L				
7	500	Roughness		R	3.2	0.05	0.95639
			L		2.5	0.06	
8	500	Roughness		R	6.3	0.04	1.002771
			L		2.1	0.05	
9	400	Roughness		R			1.090399
			L				

this application can be easily implemented as it used a basic mathematical calculation. Regardless of its efficiency and effectiveness, it should be used as an alternative method compared an advance method that using a new technology.

5) Conclusions

The results of the present research are summarised as follows;

1. The simple numerical analysis on road pavement condition assessment as maintenance strategy is considered as an option to be used by the road engineers in least developing country like Timor-Leste.
2. This method is considered as a simple and rational method because it is relatively low cost. Therefore, it can be used a maintenance strategy for Timor-Leste road network.
3. This method may support the complex sustainability issues and also to recognize and define a problem in detail such as land slide, potholes, water runoff problem and debris.
4. The present method could help to identify subjective and objective evaluation.

References

[1] Government of Timor-Leste, Timor-Leste Strategic Development Plan 2011–2030, pp. 72-78, 2011.

[2] JICA Timor-Leste, Annual report, 2013.

[3] Road for Development (R4D) "Building a sustainable Rural Road Network in Timor- Leste" AusAID Timor-Leste, 2011.

[4] H. Ximenes, Practical Application of Road Condition Assessment System to Road Network in Timor-Leste, Japan, 2015

[5] S. KIKUKAWA, and Y. Anzaki, Present Situation and Prospects of Pavement Maintenance Management System in Japan, 2nd North American Pavement Management Conference 1987, 1987.

Initial Studies of Physical Properties of Fine Aggregates and Its Application to Concrete in East Timor

Leandro Madeira Branco

Faculty of Engineering, Science and Technology, Universidade Nacional Timor Lorosa'e, Avenida Hera, Cristo-Rei, Dili Timor Leste

Email: leandro.branco@untl.edu.tl

Abstract: River sand and limestone fine aggregates are used as a fine aggregate in the concrete and mortar mix. Material testing is carried out using the ASTM specification. Mix proportion use several variables as measurement such as several water cement ratio and ratio of limestone to river sands. The results show of physical properties of fine aggregate subsequent to ASTM standards, however, fineness modulus for river aggregate shows quite high from ASTM specification and Limestone sand has a lot of fine particles compering to river sand. The results during production concrete show some cases with high segregation, including the difference of slump however not significant. The compressive and flexural strength of rivers and limestone aggregates satisfy for concrete purpose, however by the visual view for fine aggregates which was taken from rivers directly during raining season including in the dry season, washing is required before using for concrete production purpose.

Keywords: rivers sand, limestone sand, flexural strength, compressive strength.

1. Introduction

The community in the flat area utilized river aggregate as fine construction materials such as landfill, mortar production, and concrete production etc. For the people who live in mountain side, it is difficult to access river aggregates and therefore granite stone, limestone aggregates, or clay soil are used for aggregate in concrete production and mortar purpose.

The main purpose of this research is to understand and verify the ideal combination utilization of local material such as river aggregate and limestone sand as fine aggregate in the mortar and concrete production.

2. Material and Method of Research

2.1 Material of Research

The shape of aggregate particles affects the water demand and workability, mobility, bleeding, finish ability, and strength of the rivers aggregates mostly rounded irregular, otherwise limestone fine aggregate too soft and finer. Loose bulk density reflects the grading and shape of aggregate, since it measures the proportions of voids in a given volume of aggregate. Normal-weight aggregates should meet the requirements of ASTM C 33 [1]. The Results of physical characteristic of fine aggregate experiments based on the ASTM

standard are presented in Table 1.

The results shown for rivers aggregates from Mud content, density, and compacted unit weight are following the specification of ASTM. However, the results of fineness modulus are significantly high. It shows the content of passing sieve 600 μ less than 60 percent for rivers aggregates as shown in Fig. 1, including the results for Limestone fine aggregate it shows the content of finer particle. In Table 2 physical properties of coarse aggregate are presented and those may follow the ASTM C 33. The coarse aggregates were provided from crushing stone aggregates company such as RMS Company and Montana Diak Company.

Table 1. Results of physical properties of fine aggregates

Type Experiment	Metinaro River (Me)	Liquiça Rivers (Li)	Laleia River (La)	Hauba Limestone (H)	Atsabe Limestone (A)
Mud content	2.06	3.04	2.06		
Specific gravity	2.74	2.52	2.68	2.77	2.8
Absorption	1.34	2.23	2.10	1.12	1
Fineness Modulus	3.73	3.44	3.60	2.76	1.43
Original water	1.03	0.82	0.37		
Loose Unit	1535.51	1619.80	1650.57		
Compacted Unit	1622.47	1704.08	1737.53		

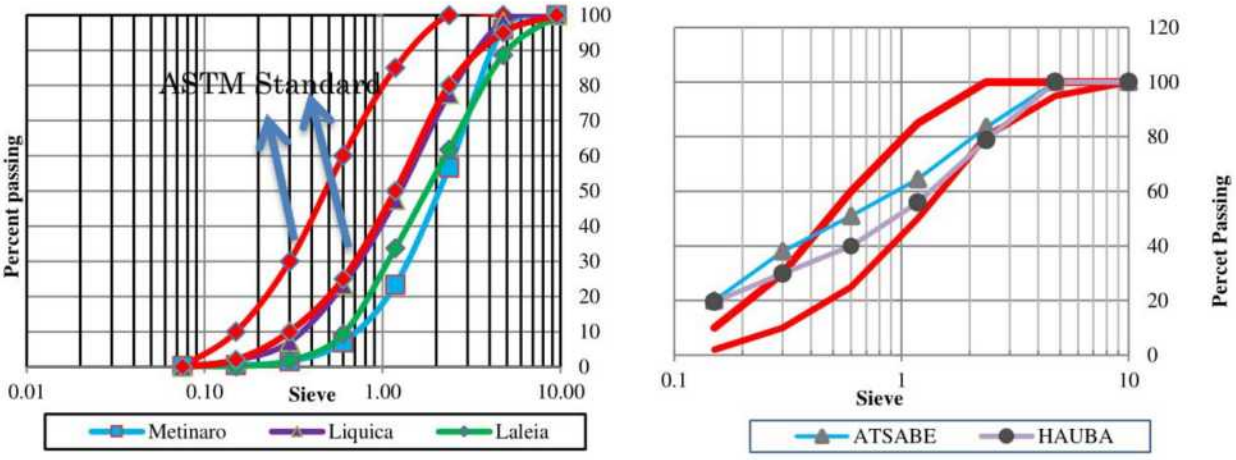

Figure 1. Gradation of fine aggregates and coarse aggregates

Table 2. Results of physical properties of coarse aggregates

Experiment method	RMS Course Aggregate (rivers sand)	Montana Diak coarse aggregate (limestone)
Abrasion (%)	27.6	
Bulk S Gravity (g/cm^3)	2.92	2.74
Bulk SSSD (g/cm^3)	2.95	
Apparent Specific Gravity (g/cm^3)	3.00	
Absorption (%)	0.95	1.34
Fines modulus	4.25	3.15
Moisture Content (%)	0.41	1.03 %
Loose Unit Wt (Kg/m^3)	1488.69	1535.51
Compacted Unit W (Kg/m^3)	1678.66	1622.47
Mud content (%)		2.06

2.2 Method of Research

Ordinary Portland cement (Tonasa) was used for this research, the mix proportion was designed based on the content water to cement ratio, within defining by the variety from 50 to 60 % water cement ratio. The coarse aggregates with basaltic origin for both of course aggregates with maximum size 20 mm it take from local stone crusher (RMS and Montana diak). The compositions of the concrete mix proportion shown in Table 3, the mix proportion for river aggregate, limestone concrete are used for investigation. The mix proportion was designed use terms of the ACI Mix (Absolut volume method) [2].

3. Result and Discussion

3.1 Fresh Concrete Testing

Workability of concrete is significantly influenced by various mixing properties such as the water-cement ratio, fine aggregate–total aggregate ratio, and total volume of aggregate [3]. Figure 2 shows the result of slump for all variation concrete specimens. The result of slump test of rivers fine aggregate is significantly low. However, the total water for the concrete mix (water consumption) was higher comparing with JIS standard (175 kg/m^3), and ASTM standard (180-190 kg/cm^3), it showing during casting of concrete, the high volume of segregation was occurred. The temperature during casting concrete itself influences the workability of slump [4].

The result of slump of The Limestone fine aggregates concrete are significantly influenced by the amount total limestone fine aggregates inside concrete. It also shows the limestone when combined with rivers aggregate, the workability will increase as shown in the Fig. 2.

3.2 Compressive Strength of Concrete

Compressive strength of concrete is significantly influenced by various mixing properties such as the water-cement ratio, fine aggregate–total aggregate ratio, and total volume of aggregate [5, 6]. The results of compressive strength are shown in Figure 3 for the river fine aggregate concrete within variety composition of concrete mix. The result shown for the specimen from Metinaro River (Me) is quite higher compared to Liquisa River (Li) and Laleia River (La). The results compressive strength of limestone fine aggregates as shows in the figure 4 and figure 5 for the results of limestone and river fine aggregates combined, and fully (100 %) limestone in the concrete. The results show the compressive strength for specimens contain 100 % limestone fine aggregates no significate higher compare to the others (25 %, 50%, and 75 %).

Table 3. Mix proportion of concrete

No.	Code	W/C	Water kg/m^3	Cement kg/m^3	Coarse Aggregate kg/m^3	Fine Aggregate kg/m^3	Limestone (Kg/m^3)
1	Li-2	58%	207.9	358	1109.6	796.3	
2	Me-2	58%	207.9	358	1116.3	860.4	
3	La – 2	58%	207.9	358	1112.9	844.2	
4	Li – 1	52%	207.9	397.8	1109.6	766.1	
5	Me -1	52 %	2079	397.8	1116.3	827.5	
6	La - 1	52%	207.9	397.8	1112.9	812	
7	A- 25	52%	232.7	447.5	1108.7	593.72	200.77
8	A- 50	52%	232.7	447.5	1108.7	395.81	401.55
9	A -75	52%	232.7	447.5	1108.7	197.91	602.32
10	A -100	52%	232.7	447.5	1108.7	0	803.1
11	H- 25	52%	232.7	447.5	1081.6	612.82	205.01
12	H -50	52%	232.7	447.5	1081.6	408.55	410.03
13	H- 75	52%	232.7	447.5	1081.6	204.27	615.04
14	H-100	52%	232.7	447.5	1081.6	0	820.06

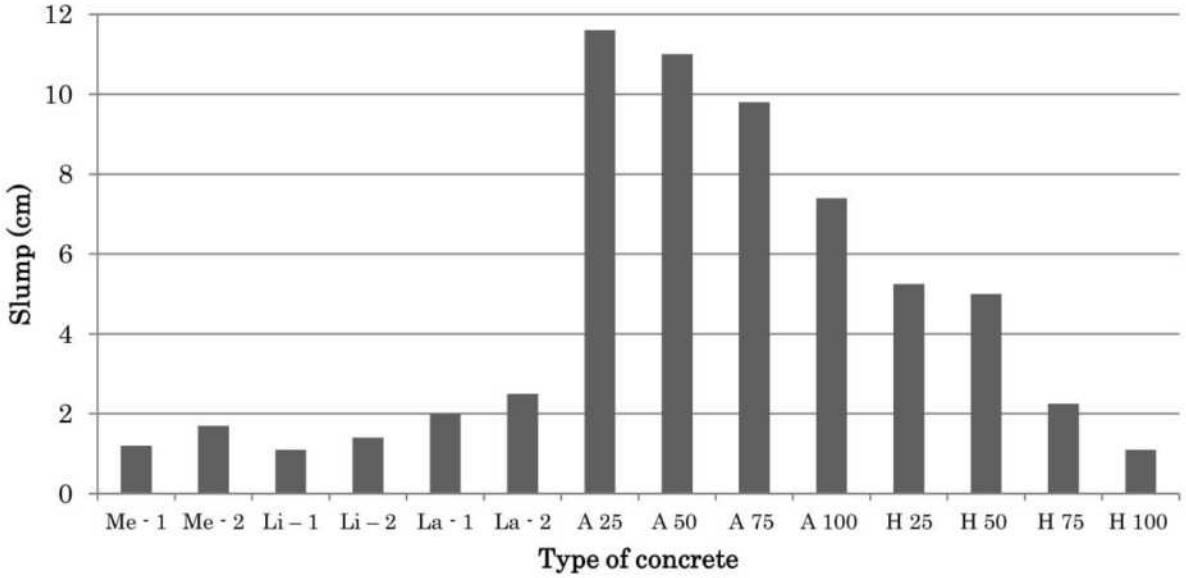

Figure 2 Results of slump testing

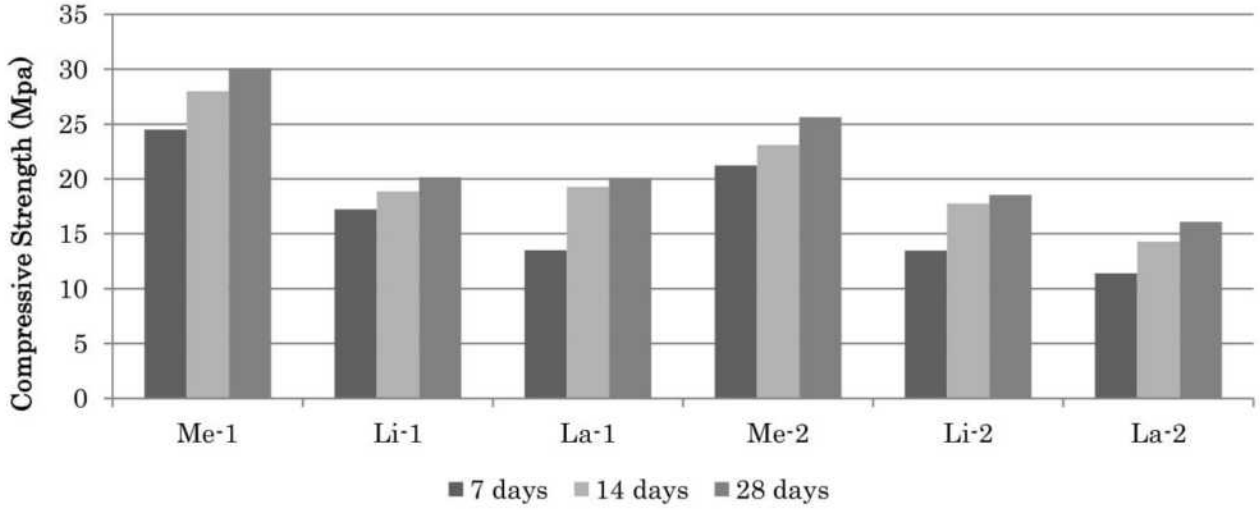

Figure 3 Compressive strength of concrete of rivers aggregates

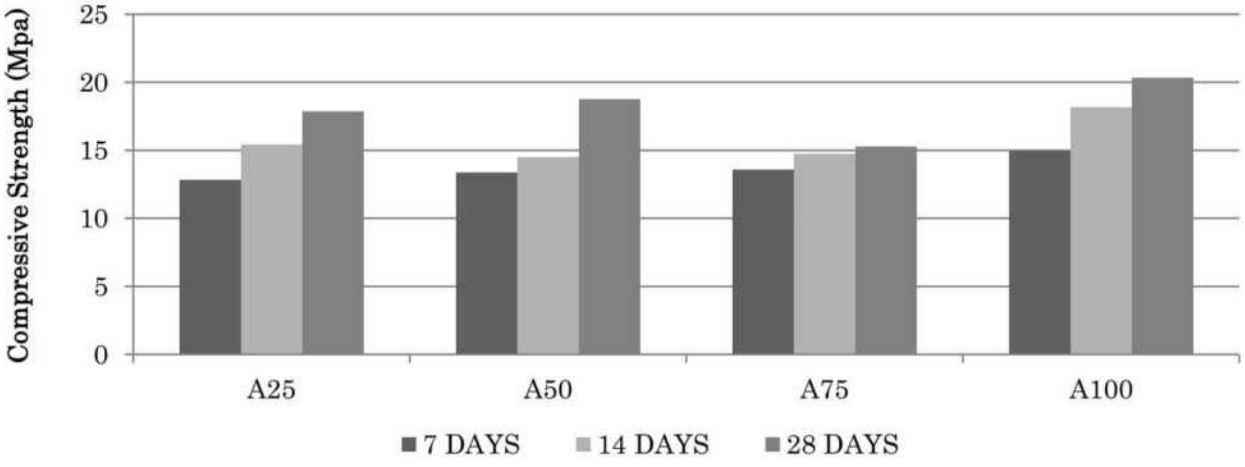

Figure 4 Compressive strength of concrete of limestone concrete at Atsabe

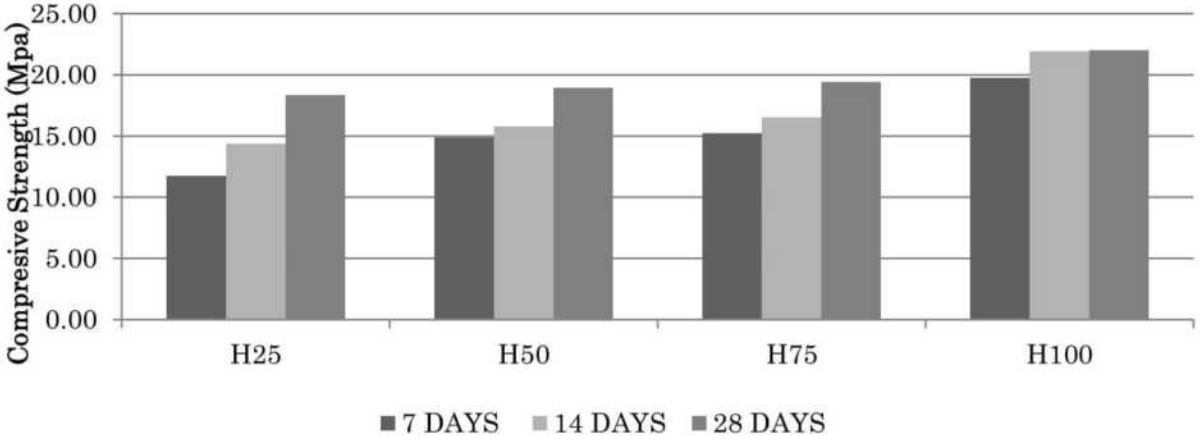

Figure 5 Compressive strength of concrete of limestone concrete at Hauba

4. Conclusion

Following conclusions were obtained:

1. Mechanical properties of several river sands and limestone sands as fine aggregate were clarified, according to the ASTM specification.
2. Fineness modulus for the river aggregate showed quite high in the ASTM standards
3. Limestone sand had a lot of fine particles compering to river sand.
4. The slump test showed that the volume of the limestone affects the rate of workability, it's suggested that limestone fine aggregates need more water compare to river aggregate.
5. Compressive strength with the various percentages of limestone showed that an increase of the volume of limestone increases its strength.
6. Improve the gradation of fine aggregates to meet ASTM standard, its necessary to increase the strength of concrete itself.

Acknowledgement

The author acknowledges Joel Martins de Fatima, Nazario Barros Martins, Fransisco Inacio F. dos R. Corsino, Andre Salem and Domingos Auni for their support of the present work.

Reference

[1] P.Kumar Metha, Paulo J.M.Monteiro 2006.Concrete Microstructures, Properties and Materials, Third Edition. McGram-Hill-USA.

[2] Kett, Irving, 2010, Engineered concrete: mix design and test method 2nd ed ISBN 978-1-4200-9101-4, USA

[3] A.M.Neville, J.J.Brooks. (2010) Concrete Technology second edition. ISBN 978-0-273-73219-8. Prentice hall (PEARSONS) printed in Malaysia.

[4] Anonym 2004, concrete basics "A guide to concrete practice" Cement Concrete and Aggregates Australia

[5] B Balapgol, S A Kulkarni, K M Bajoria (2002) Strength And Durability Of Concrete With Crushed Sand 27th Conference On OUR WORLD IN

CONCRETE & STRUCTURES: 29 - 30 August 2002 Singapore

[6] B. Menadi a, S. Kenai a, J. Khatib b, A. Al t-Mokhtar, "Strength and durability of concrete incorporating crushed limestone sand". Construction and Building Materials published by Science direct, Vol 23 (2009 pp. 625–633.

Pothole size calculation system using reference object based on image processing

Olga Maria de Sousa

Department of Electronic and Electrical Engineering, Faculty of Engineering, Science and Technology, Universidade Nacional Timor Lorosa'e, Avenida Hera, Cristo-Rei, Dili, Timor Lorosa'e

E-Mail: sousa.olgamaria@gmail.com

Abstract – Measurement of pothole is very important in order to know the damage of the road. In East Timor, the manual measurement is still the only way to know the pothole size. In this research, measurement based on image processing technique is proposed. A simple GUI is designed using MATLAB for measurement purpose. Selection of ROI, Binary image and Region props are combined in this system. The system is experimented on samples of pothole images and A4 paper is used as reference object. This simple method is effectively performed good for top view camera position Image.

Keywords: pothole, region of interest, reference object, GUI design.

1. Introduction

Pothole is one of the big issues in road maintenance system of Timor Leste. This pothole should be mostly caused by heavy rainfall and the structure of the road itself. Most of the roads in East Timor are still under constructing. Some of new roads are already constructed with all the surface marking. The road maintenance in East Timor is still performed using manual system. Damage of road surface is still done by hand on the spot. Thus, this research aims to develop an image processing system for measuring pothole.

Related to pothole detection and size estimation, many works have done in recent years. Many researchers have proposed some methods related to these kind of works [1-4]. Most of them proposed good image processing technique that perform good on pothole detection. Some of recent works are only dealing with detection of pothole in a road without estimating its size. The review of pothole detection has done by Taehyeong Kim and Seung-Ki Ryu [5]. They presented that pothole detection method can be divided into vibration-based methods, 3D reconstruction-based method and vision-based methods. However, simple yet good method is still an interesting task to be done.

The contribution of this work is to design a simple user-friendly interface that is easier in operating. The selection of region of interest makes this method work well on low quality images [6,7]. Unnecessary filtering technique is

main advantage of this work. This system can be used to estimate any pothole as long as the reference object exists in same frame with pothole. However, this system performs effectively only on top view camera position image.

The image used in this simulation is samples images that are not taken on actual road. These images are taken for preliminary experiment purpose only. The implementation for real pothole size estimation will be done in near future.

The rest of the paper is organized as follow. Section 2 describes the methodology of the research. The process of ROI (Region of Interest) selection, binaries image and calculation of width and length of pothole are explained in this section. Section 3 shows the experimental results that obtained in this work. The paper is concluded in Section 4.

2. Approach

A simple extraction method, such as selection of region of interest (ROI), binary image conversion and region props, are used to extract and estimate the pothole size. All the processes are combined into a simple graphical user interface (GUI) in order to develop a friendly user system. The extraction process is shown in Fig. 1.

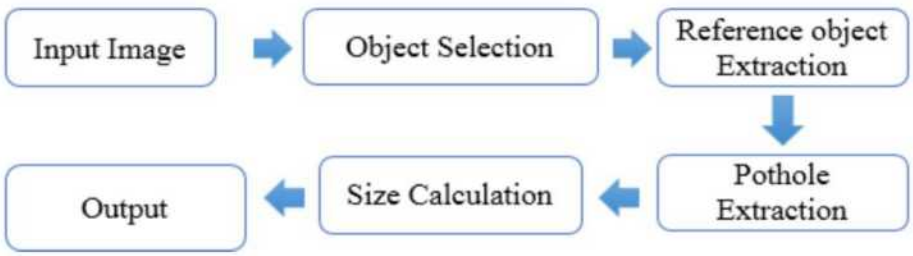

Fig. 1 The block diagram of pothole size estimation

a. Selection of ROI

Selection of region of interest is very important for measurement purpose in this research. Firstly, we define the ROI of reference object. It is simply done by giving the coordinate points and link it around the selected object. The shape of selected ROI depends on how the coordinate points are chosen. In this preliminary experiment, the shape of selected ROI is rectangle shaped.

Next, the same selection process is done to select the ROI of pothole part in image. After selection, masking is applied to extract the selected region by setting all unnecessary region into black pixels. Figure 2 shows the input image with pothole. Fig. 3 and Fig. 4 shows the result of ROI selection of reference object and pothole respectively.

b. Binary Image

As the continuation of extraction selected ROI, the image will change into binary image which only consist of black and white pixels. The formula of binary image is given in Eq. (1).

$$f_o(x,y) = \begin{cases} 0 \; if \; f_1(x,y) < T \\ 1 \; if \; f_1(x,y) \geq T \end{cases} \quad (1)$$

Where T is the threshold value, f1 and f0 represent the original and binary image respectively.

Threshold value in this experiment is used 128-pixel intensities. Pixel position is indicated as x and y. The result of binary image is shown in Figs. 5 and 6.

Fig. 2 Input Image

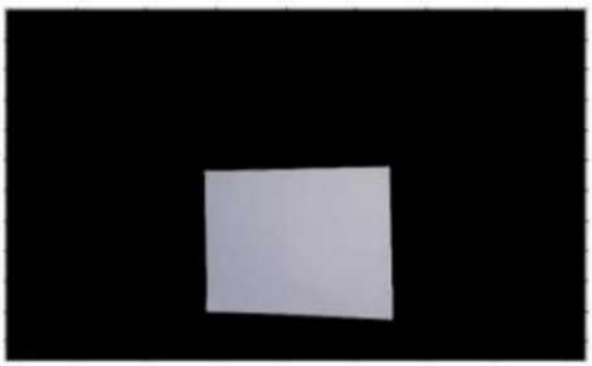

Fig. 3 Reference Object Extraction

Fig. 4 Pothole Extraction

c. Region Props

Region props can be a very important function in measuring properties of image. In this research, region props are used to generate the rectangle around the selected region. Based on the height and width of the rectangle, the real size of object will be calculated. The result of region props is shown in Fig. 7.

Fig. 5 Binary image of reference

Fig. 6 Binary image of pothole region

d. Pothole Calculation

This research aims to calculate the length (L) and the width (W) of the pothole size. The real size of reference object plays very important role in this calculation. Three parameters, such as real width and length of reference object, pixel width and pixel length of reference object, pixel width and pixel length of pothole are used to calculate the real size (width and length) of pothole. The reference object used in this research is A4 paper that highlighted in red rectangle shown in Fig. 8. The real length of A4 Paper is 29.7cm and 21cm for its width.

The pixel length and width are the length and width of the red rectangle itself. The pixel of

sample images of reference object and pothole that are shown in figure 6 and figure 7 can be seen in Table 1.

Table 1. The pixel size of reference object and pothole

	Length	Width
Real Size of HVS	29.7	21
Pixel Size of HVS	1344	1002
Pixel Size of Pothole	3558	864

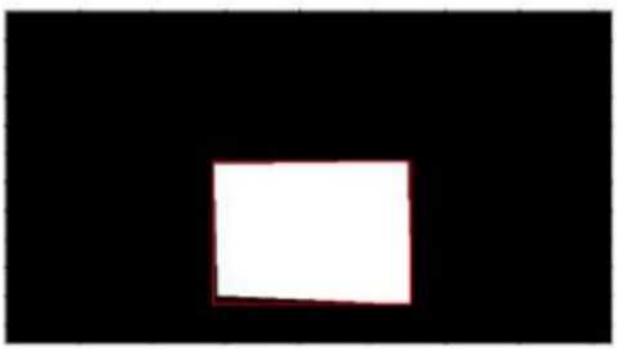

a. Reference object

b. Pothole

Fig. 7 Binary image of pothole region

Fig. 8 Reference object indicated in red

The calculation is done based on formula shown in equation 2 and 3.

$$\text{Real Pothole W} = \frac{Pothole\ pixel\ W}{Ref.pixel\ W * Real\ Ref.W} \quad (2)$$

$$\text{Real Pothole L} = \frac{Pothole\ pixel\ L}{Ref.pixel\ L * Real\ Ref.L} \quad (3)$$

3. Experimental Result

a. GUI Look

A simple GUI is developed using MATLAB to create a friendly user interface. The designed GUI can be seen in Fig. 9. For each estimated result that obtained can be considered as ±2cm correct.

The step of using this developed GUI:

1. **Input Image**: allow us to choose the desired image of pothole. Click browse to search for folder where the desired image is saved. After selected, the image will appear on space of original image.
2. **Select reference object from original image**: allow us to select the reference object location in original image. It is simply done by drugging the cursor between the corners of reference object. After selection, the result will extract out only the position of reference object in image, however the rest of the pixels are set to black or zero intensities. The result

of selection will be appeared on white space of number 2.

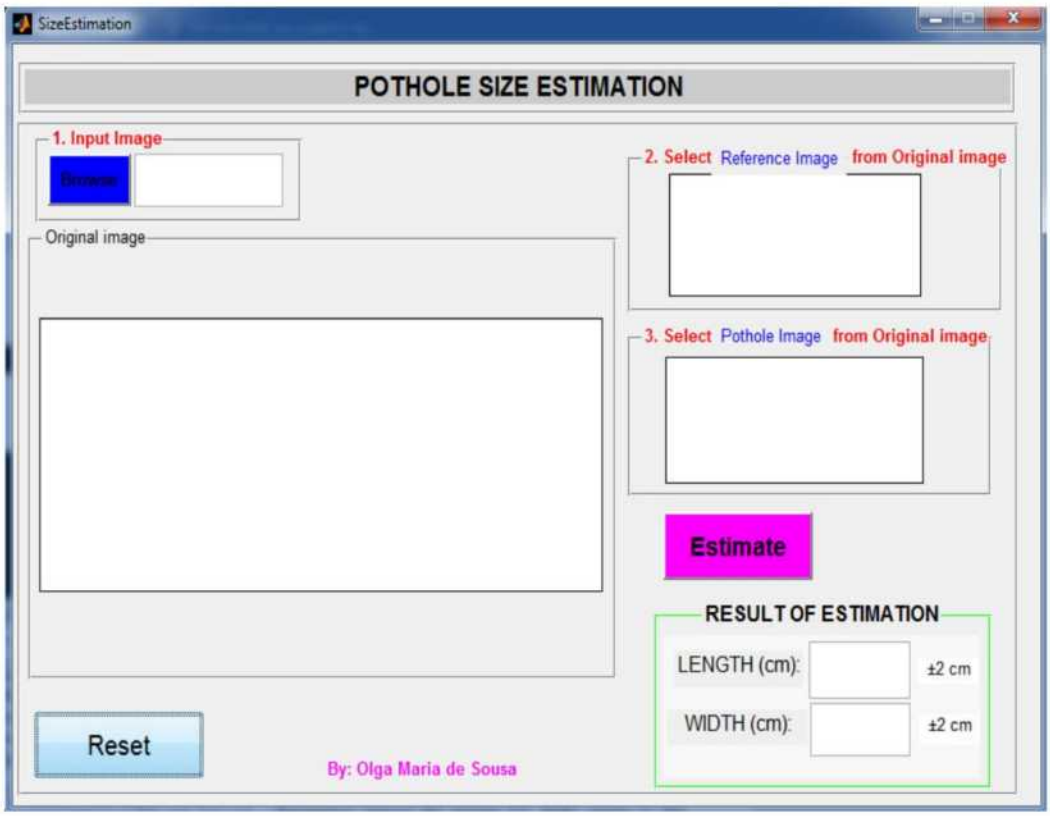

Fig. 9 GUI Layout

3. **Select pothole object from original image**: allow us to select the pothole object location in original image. The selection process is same as selection of reference object. Same process as previous step, the result will extract out only the position of pothole in image, and the rest of the pixels are set to black or zero intensities. The result of selection will appear on white space of number 3.
4. **Estimate:** is a push button that will show us the result after it is clicked. The result will be appeared in white boxes of length and width.

b. Experimental Result

In Fig. 10 bellow shows result of experiment using developed GUI. Each image contains of pothole and we placed one A4 paper as a Reference object. The required parameter to be used in estimation process are, the real length and width of reference object, pixel length and width of reference object, and pixel length and width of pothole that obtained in simulation.

The experimental is done for pothole images and the result is shown in Table 2 includes the error rate. The error is simply done by subtracting the real size with the calculated value.

Fig. 10 Experimental result using GUI

This experimental is done using five sample images of pothole where in each image we place A4 paper.

Table 2. Experimental result

Pothole		Real Size (cm)	Calculated (cm)	Error (cm)
1	Width	20	18.1	1.9
	Length	80	78.5	1.5
2	Width	18	18.5	0.5
	Length	20	19	1
3	Width	20	19.9	0.1
	Length	24	22.4	1.6
4	Width	95	93.7	1.3
	Length	150	148.2	1.8
5	Width	74	75.9	1.9
	Length	84	83.3	0.7

The method of calculation is based on pixel width and pixel length of the object in image. Thus, selection of ROI becomes the determinant key of obtained result. In Table 2 described the error rate that is not more than 2cm. The error is mostly caused by the pixel selection of ROI.

However, the error rate is acceptable hence it is less than 2cm. The component ±2cm shown in GUI basically designed to represent the error rate.

4. Discussion

Although the results show the low error rate, this system is still far to be used for real implementation. Hence this system is experimented on top view camera position images only. It is highly recommended to be experimented on images with different angle of camera position images. In order to obtain a good performance, camera parameter, such as distance, angle of view, height, field of view, must be considered to be included in estimation.

5. Conclusion

The system built in this research is simple and friendly user. It performed good on measuring the pothole, and the results showed low error rate. However, the experiments in this research are still done using still image. Thus, in future, this system should be improved for real time application.

References

[1] T. Ptathiba, Thamaraiselvi, Mohanasundari M3., and Veerelakshmi R4., "Pothole Detection in Road Using Image Processing," BEST: International Journal of Management, Information Technology and Engineering (BEST: IJMITE), vol. 3, issue 4, pp. 13-20, April 2015.

[2] Satyavratan G., Neelamegam P. and Rubalya Valantina S., "Image-Based Surface Crack Inspection and Pothole Depth Estimation.," Research Journal of Pharmaceutical, Biological and Chemical Sciences, pp. 611, July-August 2015.

[3] Lokeshwor Huidroma, Lalit Kumar Das and S. K. Sud, "Method for Automated Assessment of Potholes, Cracks and Patches from Road Surface Video Clips," Procedia - Social and Behavioral Sciences, vol. 104, pp. 312-321, December 2013.

[4] S. Nienaber, M. Booysen and R. Kroon, "Detecting Potholes Using Simple Image Processing Tehniques and Real-World Footage," Proceedings of the 34th Southern African Transport Conference (SATC 2015), 2015.

[5] Taehyeong Kim and Seung-Ki Ryu, "Review and Analysis of Pothole Detection Methods", Journal of Emerging Trends in Computing and Information Sciences, Vol. 5, no. 8, pp. 603-608, August 2014.

[6] Yongquan Xia, Lihui Cheng, Weili Li and Shaohui Ning, "A Region of Interest Extraction Approach Based on Adaptive Threshold in Intelligent Transportation System," Asia-Pacific Conference on Information Processing, 2009.

[7] Warinthorn Kiadtikornthaweeyot and Adrian R. L. Tatnall, "Region of Interest Detection Based on Histogram Segmentation for Satellite Image," The International Archives of the Photogrammetry, Remote Sensing and Spatial Information Sciences, 2016.

Machine Learning Based System for Motorbike Mode Detection Using a Smartphone Sensor

José Elias Pereira Tilman, Quintino Soares, Lúcia Jorge Pereira, Ferdinando da Conceição Soares, Nicolau Castro Ximenes, Abreu André Boavida and Frederico Soares Cabral

Faculty of Engineering, Science and Technology, Universidade Nacional Timor Lorosa'e, FEST-UNTL, Avenida Hera Cristo Rei, Dili, Timor Leste.

E-Mail: jose.ptilman@untl.edu.tl, nau_tul@yahoo.com

Abstract: As the exponential grow of smartphone users in every year, a development of mode detection system using smartphone sensors with machine learning techniques has become an important research field in informatics. This paper describes a use of Android OS based smartphone to detect the mode of motorbike by collecting data from two types of smartphone sensors such as accelerometer and gyroscope. In this study, we propose two approaches for motorbike mode detection. One is by using high dimensional features and another is by applying machine learning techniques. We evaluate the performance and the accuracy of these approaches.

Keywords: smartphone sensor, machine learning, mode detection

1. Introduction

The increasing number of smartphone device users in every year is an unavoidable issue. In fact, there are many applications developed to provide services and resources for users need. Besides integrated with a lot of applications, the smartphones are affordable to get because of low cost. In fact, the ratio of populations that owns smartphones has reached up to 98% of the nation [1].

Nowadays the smartphones are used not only for communication purposes but also for research activity. The data collection using smartphones has gained a lot of researchers' attention in the last several years [1,2]. The smartphones equipped with many sensors which enables us to track and obtain information such as Global Positioning System (GPS), compass, accelerometer, and gyroscope sensors. These data can be used to detect and recognize the user's transportation mode. In this paper, we try to use such the sensors to collect data in order to detect motorbike mode. There are several types of motorbike mode to be considered, such as engine-off, engine-on in stop position, and moving mode.

Many studies have conducted by collecting data from smartphone accelerometer and gyroscope sensors embedded in mobile device to classify paved and unpaved road condition and detect anomaly on the paved road, such as pothole and bumps [1,3]. Stenneth et al proposed a method which uses mobile phone and GIS information to detect user

transportation mode [4]. However, the collecting data extracted from GPS sensor suffered several limitations such as GPS information is not available in shielded areas, coverage of GPS signals may be lost especially in high dense locations, which results in inaccurate position information [5]. Moreover, a GPS sensor consumes a significant amount of energy and may rapidly deplete the battery of a mobile device [5,7]. Nevertheless, to reduce the energy consumption [8], Inertial Measurement Unit (IMU) sensors including accelerometer, gyroscope and magnetometer were applied. In [9] user controls the whole system using mobile application sensor such as Global System for Mobile Communication (GSM), GPS technology and camera to locate the motorcycle and image-capturing technology to help ease stolen motorcycle search and recovery. Thus, the innovation of a vehicle security system has the ability to turn off the vehicle engine and send real-time alerts to the vehicle owner. In [10] using accelerometer smartphone's sensor to health monitoring by assessing individual carbon footprint in footprint calculators application on smartphone devices, [11] is focused on reducing the footprint of a big data classifier to detect transportation modes(such as still, walking, running, biking and on a vehicle), [12] monitoring of road and traffic condition using mobile smartphones, which used the accelerometer, microphone, GSM radio, and/or GPS sensor in these phones to detect potholes, bumps, braking and honking.

Researchers have implemented several approaches to discriminate between transportation mode effectively using mobile phones [2]. We have taken into account some of drawbacks literature review of machine learning and deep learning techniques for classification tasks are applied such as Decision Tree (DT) [2,5,7,10,11,13,14], Support Vector Machine (SVM) [2,3,5,7,11,13,16], Random Forests (RFs) [2,5,7,14], K-Nearest Neighbor (KNN) [2,5,7,13,14], Convolutional Neural Network (CNN) [7,17], Adaptive Boosting (AdaBoost) [7,11,13], Deep Neural Network (DNN) [6,7,18], Hidden Markov Model (HHM) [1,14], Residual Network (ResNet) [1] and Dynamic Time Warping(DTW) [1].

The results of these studies have obtained different classifying accuracy. There are several factors that affect the accuracy of detecting transportation modes, such as the monitoring period, number of modes, data sources, motorized classes, sensor position and overall one of the critical affects the accuracy of the mode detection is the machine learning framework classified [2,5].

In this this paper, we investigated the possibility of improving the overall accuracy of motorbike mode detections by arranging a new framework classifier and a new feature set. However, in this case we used high dimensional features and state of the art machine learning techniques to make the system robust [1]. We applied simple conventional Machine learning techniques for classification, namely K-Nearest Neighbor (KNN). Furthermore, we found 100 % high accuracy applying for this classification to detect motorbike mode.

2. Data Acquisition

The system we proposed in this paper can be implemented on any smartphone devices with accelerometer and gyroscope sensors. In this case we required only these both sensors to detect motorbike mode by ignoring a GPS vector location and internet connection for the

computation of the motorbike travelled distance.

The recording data were divided into two sets, i.e., training and testing. In this experiment, 70% of the data were selected for training and the remaining 30% for testing.

The data was recorded in sampling rate of 100 Hz result totally in eleven variable, i.e., timestamps, three axes of accelerometers (x ,y, z), three axes of gyroscope (x, y, z), three points of GPS (latitude, longitude, altitude) and compass [1]. Fig. 1 shows the GUI of the android application developed on smartphone.

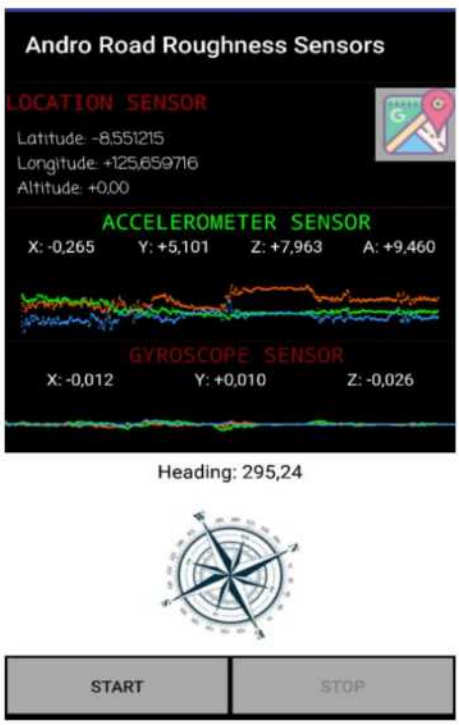

Fig. 2 An android application developed for data collection.

3. Data Pre-Processing and Feature Extractions

The preprocessing process require triaxial (x, y, z) acceleration signal at a sampling rate of 100 Hz. These signals are processed in four steps as follow, posture re-orientation, smoothing, segmentation and features extraction [1].

A. Posture Re-orientation

We propose the smartphone must be installed in the position as shown in Fig. 2, in which the accelerometer axis (x, y, z) are corresponded to angle of that position. Moreover, the triaxial x, y and z of the accelerometer sensors represent the directions of left to right, top to bottom of vertical acceleration and front to rear of the vehicle, respectively [3].

Fig. 1 Smartphone and Motorbike axes.

Therefore, Euler angel and rotation matrix are used to re-orient the angle of smartphone virtually [1,12]. As shown in Fig. 3,

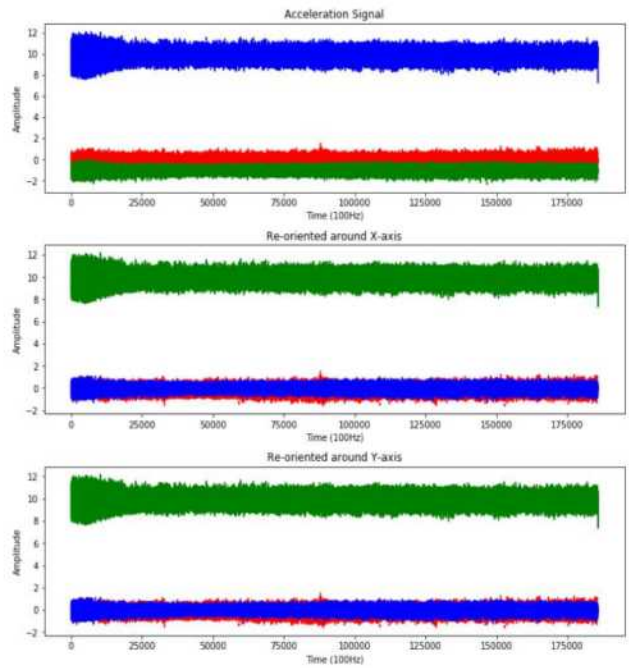

Fig. 3 Reorientation direction of accelerometer signals.

reorientation acceleration signal from the angel around of X-axis and Y-axis.

B. Smoothing

After the signals of the acceleration sensor have been reoriented, the next step is followed by maintaining the consistency of the data to avoid noise. The data are smoothed by applying the central moving average algorithm [7]. As shown in Fig. 4.

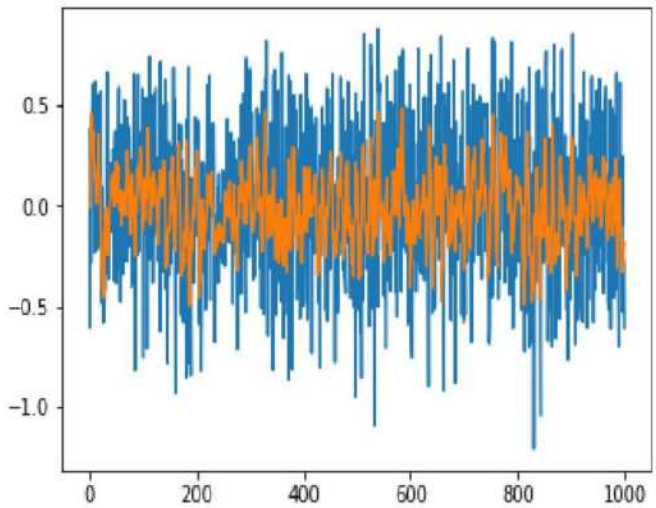

Fig. 4 Normalizing signals by applying smoothing technique.

C. Segmentation

The Acceleration signals data are segmented according to the fixed-width sliding window of 2 seconds and 20% overlaps between them [1].

D. Features extraction

A vector of features for each sampled window or both time domain and frequency domain obtained [1]. In some studies [1,2,13,16], the extracted features were considered to have a meaningful relationship with different transportation modes [2]. The Feature extraction techniques based on different mathematical and statistical procedures and relevant for the learning task [14]. Therefore, these features are used in this study to compare mean, variance, standard deviation, mean absolute deviation, maximum, minimum, root mean square, signal magnitude area, interquartile range, correlation coefficient, energy and skewness [1]. As a result, totally 34 features are extracted to describe each road window. Table 1 shows the list of computing feature vector for time domain signals.

Table 1. List of features extraction vector.

Features	Time
Mean	3
Variance	3
Standard deviation	3
Mean absolute deviation	3
Maximum	3
Minimum	3
Root mean square	3
Signal magnitude area	1
Interquartile range	3
Correlation coefficient	3
Energy	3
Skewness	3

4. Classification Method and Performance Evaluation

4.1. K- Nearest Neighbor (KNN)

KNN is one of the conventional algorithms and simplest supervised learning used for classification or regression in machine learning algorithm [1,2,13]. For the output in classification an object is usually classified by the majority of the votes received by its neighbor and the output of the regression the object is based on the property value [13]. The typical k-NN algorithm uses a Euclidean distance to define nearest neighbor [1]. The distance can be computed using this following formula:

$$D(x,y) = \{\sqrt{\sum_i (xi - yi)^2}\}, \quad (1)$$

where D (x, y) is the shortest distance between any two samples [13]. In this study we applied KNN technique to detect motorbike mode.

4.2. Performance Evaluation

In this study, the KNN was used to identify motorbike mode performance. To measure the performance of our model for its classification, we evaluated the model for both training and forecasting data according to the accuracy, precision, recall, f1-score, which are widely used for performance evaluation the result of predictions [1]. These features performance evaluation are defined as:

$$\text{Accuracy} = \frac{TP+TN}{TP+FP+FN+TN} \quad (2)$$

$$\text{Precision} = \frac{TP}{TP+FP} \quad (3)$$

$$\text{Recall} = \frac{TP}{TP+FN} \quad (4)$$

$$\text{F1-score} = \frac{2\ x\ (Recall\ x\ Precision)}{Recall+Precision} \quad (5)$$

In the equation above, *tp, tn, fp* and *fn* stand for true positive, true negative, false positive and false negative. In which *tp* is the correctly predicted positive values which means that the value of actual class is yes and the value of predicted class is also yes. A *tn* is the correctly predicted negative values which means that the value of actual class is no and value of predicted class is also no. Otherwise *fp* and *fn* are the values occur when the actual class contradicts with the predicted class. It can be explained as: *fp* is when actual class is no and predicted class is yes, and *fn* is when actual class is yes but predicted class in no [19]. Thus, the four parameters as explained before can be used to calculate performance evaluation namely: the accuracy is to assess the overall effectiveness of the algorithm, precision is to assess the predictive power of the algorithm, recall is to assess the effectiveness of the algorithm on a single class and f1-score is the weighted average of precision and recall [19] [20].

5. Experiments and Result

A. Data Recording

A smartphone application was developed for the purpose of data collection [5]. In this work, the smartphone used for the data acquisition was a OPPO A57, running android OS version 6.0. This phone has been chosen, given its programing capacities based on the Java Programing Language and it embedded accelerometer, gyroscope and GPS sensor's applications. For the transportation mode experiments we used Yamaha Vixion motorbike. The recordings data were carried out in the Timor-Leste road, in which a smartphone was located on top of motorbike tank. As shown in Fig. 2.

The data collection was conducted in two different ways, firstly we recorded 30 minutes of data when motorbike engine-on on stop position and secondly, we recorded the remaining 30 minutes of data by considering motorbike on moving position. The data were collected on different type of paved road condition with different speed limits by ignoring traffic jam conditions occurring on real-world conditions.

B. System Design

The data extracted from both signals of acceleration and gyroscope sensors considering as a raw data. Initially these raw data were normalized to reduce the smartphone orientation variability. After the angel of smartphone oriented virtually in the fix position, the data were smoothed to maintain

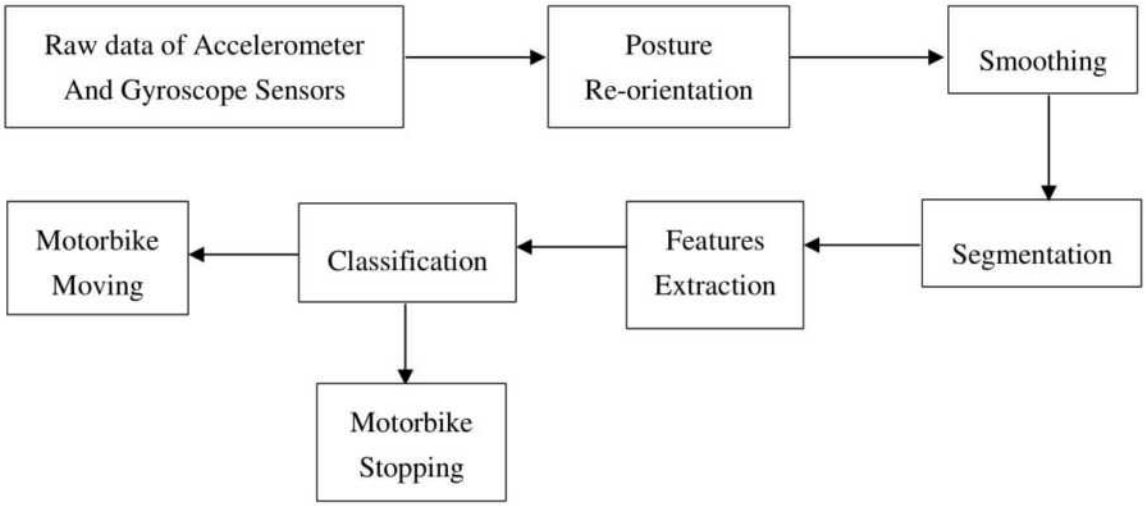

Fig. 3 The architecture design procedure for classification and motorbike detection mode.

consistency of signals. The signals were then sampled in the fixed-size sliding window of 2 seconds with 20% overlaps before extract the features [1]. The computation of these features was used as an input for classification model such as KNN to detect motorbike mode. The architecture of this experiment is shown in Fig. 5.

C. Motorbike Mode Classification and Result

To evaluate the model, different steps of procedure have been taken in consideration. Before learning the model, the data must be preprocessed in several steps as previous mentioned: posture reorientation, smoothing, segmentation and feature extraction. The learning model should be trained before classifying. In the performance evaluation, the scores of accuracies, precision, recall and f1-score were used.

The score of model performance evaluation applied for algorithm KNN with Euclidean Distance achieved 100% for all criteria. Table 2. shows the KNN achieved higher score of the classification such as accuracy, precision, recall and f1-score.

Table 2. The classification results (accuracy, precision, recall and f1-score).

Class	KNN Classifier			
	Precision	**Recall**	**F1-score**	**Data support**
stop	100%	100%	100%	361
move	100%	100%	100%	335

The confusion matrix contains information about actual and predicted classification performed by a system [16]. Thus, labeling is an important task of the data collection process. We labeled motorbike mode in two classes such as motorbike on stop and on move position. The prediction in the confusion matrix, the header columns are the actual label, and the header rows are the prediction label. For instance, if a prediction result is the stop mode, and its actual label also is stop label, then this prediction is correct. Otherwise if a prediction result is in the move mode, and its actual class label also is move label, then this prediction result is correct as well. The correctly classified sample for motorbike mode for both labels namely motorbike stop or move mode achieved 100% of accuracy. As shown in Table. 3.

Table 3. Confusion Matrix of the prediction class for motorbike mode classification (K-NN).

		Predicted class	
		KNN	
		stop	move
True class	stop	361	0
	move	0	335

6. Conclusion and Future Work

In this work we propose only KNN classification model for learning task. The experimental result show that the overall accuracy, precision, recall and f1-score obtained by using this model is higher. The future work includes experiments with different combinations of algorithm of machine learning in order to compare their accuracy. The use of smartphone for data collection is efficient for transportation mode detection so in the future we would like to extend the experiments of using motorbike and smartphone device sensors to detect road anomaly namely bumps and potholes.

References

[1] F. S. Cabral, M. Pinto, F. A. L. N. Mouzinho, H. Fukai and S. Tamura, "An Automatic Survey System for Paved and Unpaved Road Classification and Road Anomaly Detection using Smartphone Sensor," 2018 IEEE International Conference on Service Operations and Logistics, and Informatics (SOLI), Singapore, 2018, pp. 65-70. DOI: 10.1109/SOLI.2018.8476788

[2] H. I. Ashqar, M. H. Almannaa, M. Elhenawy, H. A. Rakha, IEEE and L. House, "Smartphone Transportation Mode Recognition using a Hirarchical Machine Learning Classifier and Pooled Features from Time and Frequency Domains", pp.(99):1-9, April 2018, DOI: 10.1109/TITS.2018.2817658

[3] Y. Tai, C. Chan and J. Y. Hsu, "Automatic Road Anomaly Detection using Smart Mobile Device", National Taiwan University, Taipe Taiwan, 2010.

[4] L. Stenneth , O. Wolfson and P. S. Yu, "Transportation Mode Detection using Mobile Phones and GIS Information", University of Illinois at Chicago, pp. 54-63, November 2011, DOI:10.1145/2093973.2093982.

[5] A. Jahangiri and H. Rakha, "Developing a Support Vector Machine (SVM) Classifier for Transportation Mode Identification using Mobile Phone Sensor Data", Virginia Tech Transportation Institute, January 2014.

[6] S. H. Sánchez, R. F. Pozo and L. A. H. Gómez, "Estimating Vehicle Movement Direction from Smartphone Accelerometers using Deep Neural Networks", Sensors 2018, 18, 2624, DOI: 10.3390/s18082624.

[7] X. Liang and G. Wang, "A Conventional Neural Network for Transportation Mode Detection Base on Smartphone Platform", 2017 IEEE 14th International Conference on Mobile Ad Hoc and Sensor Systems (MASS), Orlando, FL, 2017, pp. 338-342, DOI: 10.1109/MASS.2017.81

[8] H. R. Eftekhari and M. Ghatee, "An Inference Engine for Smartphone to Preprocess Data and Detect Stationary and Transportation Mode", Transportation Research Part C Emerging Technologies, August 2016, pp.(69):313–327. 10.1016/j.trc.2016.06.005.

[9] A. O. Pachica, D. S. Barsalote, J. M. P. Geraga, J. M. Ong and M. D. Sajulan, "Motorcycle Theft Prevention and Recovery Security System", pp.850-855, 2017, DOI:10.1109/ECTICon.2017.8096372.

[10] V. Manzoni, D. Maniloff, K. Kloeckl and C. Ratti, "Transportation Mode Identification and Real-Time CO_2 Emission Estimation Using Smartphones", Massachusetts Institute of Technology, Cambridge, Massachusetts, USA, 2010.

[11] M. Yu, T. Yu, S. Wang, C. Lin and E. Y. Chang, "Big Data Small Footprint: The Design of a Low-Power Classifier for Detecting Transportation Modes", Vol. 7 Issue 13, pp. 1429-1440, August 2014, DOI:10.14778/2733004.2733015.

[12] P. Mohan, V. N. Padmanabhan and R. Ramjee, "Nericell: Rich Monitoring of Road and Traffic Conditions using Mobile Smartphones", pp. 323-336, 2008, DOI:10.1145/1460412.1460444.

[13] S. Fang, H. Liao, Y. Fei, K. Chen, J. Huang, Y. Lu and Y. Tsao, "Transportation Modes Classification Sensors on Smartphones", Sensors 16(8):1324 August 2016, DOI: 10.3390/s16081324.

[14] M. Nikolic and M. Bierlaire, "Review of Transportation Mode Detection Approaches Based on Smartphone Data", May 2017, DOI:10.4108/amsys.1.4. e7.

[15] A. Mukhtar, L. Xia, T. T. Boon and K. A. A. Kassim, "On-Road Approaching Motorcycle Detection and Tracking Technique: A Survey", 2013 IEEE International Conference on Control System, Computing and Engineering, Mindeb, pp. 63-68, 2013, DOI: 10.1109/ICCSCE.2013.6719933.

[16] H. Xia, Y. Qiao, J. Jian and Y. Chang, "Using Smartphone Sensors to Detect Transportation Modes", The Institute of Remote Sensing and Digital Earth Beijing, China, Sensors 14(11):20843-20865, 4 November 2014, DOI:10.3390/s141120843.

[17] S. Dabiri and K. Heaslip, "Inferring Transportation Modes from GPS Trajectories using a Convolutional Neural Network", pp. (86) 360-371, November 2017. DOI:10.1016/j.trc.2017.11.021.

[18] S. Fang, Y. Fei, Z. Xu and Y. Tsao, "Learning Transportation Modes from Smartphone Sensors Based on Deep Neural Network", in IEEE Sensors Journal, vol. 17, no. 18, pp. 6111-6118, 2017, DOI: 10.1109/JSEN.2017.2737825.

[19] R. Joshi, "Accuracy, Precision, Recall & F1 Score: Interpretation of Performance Measures", 9th September 2016, [Online] Available URL: https://blog.exsilio.com/all/accuracy-precision-recall-f1-score-interpretation-of-performance-measures/

[20] M. Sokolova, N. Japkowicz, S. Szpakowicz, "Beyond Accuracy, F1-Score ann ROC: a Family of Discriminant measures for Performance Evaluation", AI 2006: Advances in Artificial Intelligence, Lecture Notes in Computer Science. Vol. 4304, pp. 1015-1021, 2006, DOI:10.1007/11941439_114.

Low Power SBSAL 4x4-bits Multiplier LSI Measurement

Cancio Monteiro[a] and Yasuhiro Takahashi[b]

[a] *Department of Electrical and Electronic Engineering, National University of Timor Lorosa'e, Hera-Dili, Timor-Leste.*

[b] *Department of Electrical and Electronic Engineering, Gifu University, Gifu 501-1193, Japan.*

Email: cancio.monteiro@untl.edu.tl

Abstract: Power consumption has become an issue in the recent advances in technologies, such as Internet of Things (IoT) devices. In this context, the author has proposed a low-power source biased semi-adiabatic logic (SBSAL) circuit using 0.18 µm CMOS process technology. The measurement result of 4x4-bits SBSAL multiplier LSI is presented in this paper. The energy dissipation of the proposed circuit is compared with other fundamental logic styles at 10 KHz-100 MHz dynamic frequency ranges for simulation and 1 KHz-10KHz for measurement.

Keywords: SBSAL, adiabatic, low-power, LSI multiplier, IoT device, energy harvesting.

1. Introduction

Power consumption has becoming a critical challenging in present days of VLSI design technology where most of the Internet of Things (IoT) portable devices require autonomous energy [1]. The demand for low-power design is extremely high in wireless sensors, battery powered medical devices, implantable devices, those are potential targets which can be energized from energy harvesting technology. Conceptual diagram of charge-recycling operation that enables the direct use of the harvested signal without rectification and regulation was reported [2] as depicted in Fig.1. The prominent technique of circuit design for this purpose is by employing adiabatic switching principle [3]. The extension works on adiabatic logic technique for power reduction have been reported [4 -13], with various circuit topologies from static CMOS logic, dynamic CMOS logic and dual-rail logic styles. In this work, we proposed a source biased semi-adiabatic logic (SBSAL) [14]. Previously proposed similar logic families, such as 2PASCL [4], sub-Vt 2PC2AL [5] and the conventional static CMOS logic energy dissipation are analyzed and compared with each other. The main objective of this work is to verify the effectiveness of the proposed SBSAL at fundamental logic level and further power investigation in 4x4-bits LSI multiplier circuit.

2. Adiabatic Logic

Adiabatic switching is commonly used for minimizing the energy lost during the charging/discharging period at all nodes of a circuit [3]. The main concept of adiabatic switching is shown in Fig.3, which indicates a transition that is considered sufficiently slow such that heat is not significantly emitted. The adiabatic dissipated energy is expressed as

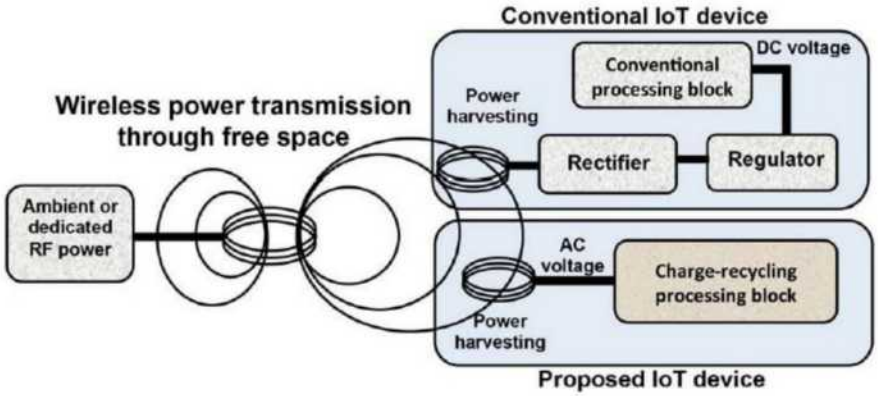

Fig. 1 Conceptual diagram illustrating the primary difference between the existing method and proposed approach [1].

$$E_{Adiabaic} = \xi \left(\frac{RC}{\tau}\right) CV_{dd}{}^2, \quad (1)$$

where ξ in the shape factor which depend on the shape of the clock edge (1 for ramp wave voltage, $\pi^2/8$ for sinusoidal voltage). The R is the effective resistance in the driven device, C is the output node capacitance to be switched, τ is the time over which switching occurs, and V_{dd} is the voltage to be switched across. Ideally, the charging energy of $E_{adiabatic}$ tends to zero by increasing the length of τ.

Conversely, the conventional CMOS logic operation is shown in Fig. 2, with the following equation:

$$E_{cmos} = \frac{1}{2} CV_{dd}{}^2; \quad (2)$$

in this case, it is possible to reduce the charging energy only by reducing V_{dd} or capacitor C. Figure 4 shows a comparison of the peak supply current for the equivalent RC models of the conventional CMOS logic and the adiabatic logic. The comparison result in this figure shows that the instantaneous peak supply current of the adiabatic logic is significantly lower than that of the conventional CMOS logic style. This means, from the energy perspective, adiabatic logic model reduces energy about five times lower than the conventional CMOS logic style.

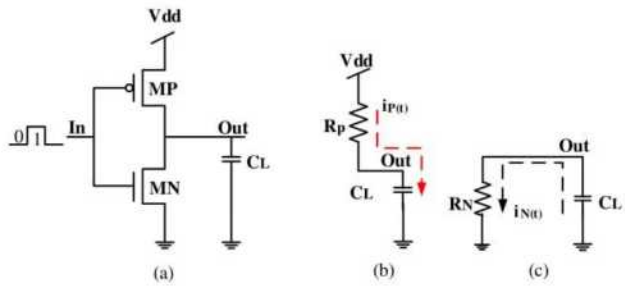

Fig. 2 a) Conventional CMOS inverter logic, b) RC model of Pull-Up-Network (PUN), c) RC model of Pull-Down-Network (PDN).

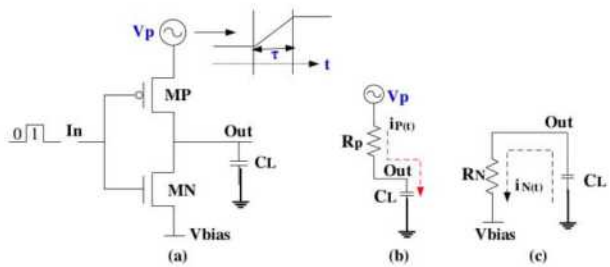

Fig. 3 a) Power clocked adiabatic inverter logic, b) PUN RC model, c) PD NRC model.

3. Proposed Source Biased Semi-Adiabatic Logic (SBSAL)

a. Conventional CMOS Logic vs. Proposed SBSAL

The proposed source biased semi-adiabatic logic (SBSAL) inverter schematic circuit topology is shown in Fig. 5(d).

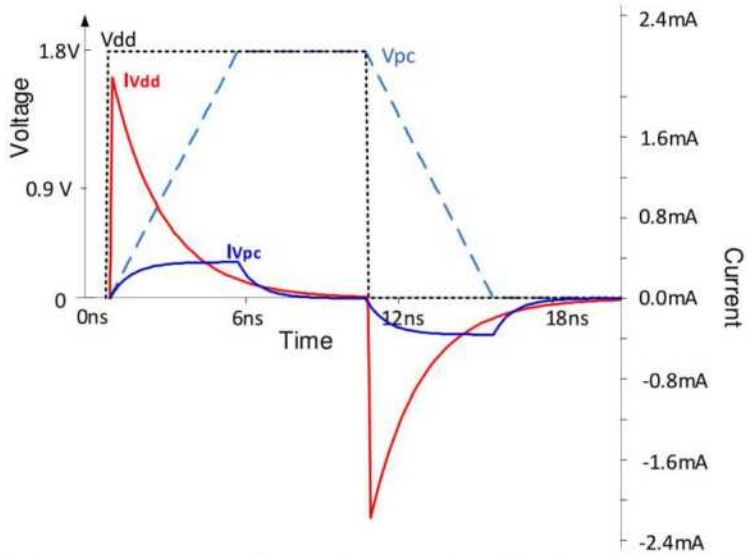

Fig. 4 Peak current comparison of conventional CMOS versus Adiabatic.

Figure 5 depicts all circuit topologies compared in this work, such as conventional CMOS inverter logic style with constant power supply of V_{dd} in Fig. 5(a), previously reported 2PASCL and sub-Vt 2PC2AL inverters in Figs. 5(b), (c), respectively. In Fig. 5, we obviously identify the difference of the four circuit topologies. The PUN of the conventional CMOS inverter in Fig. 5(a) is connected to V_{dd}, and the PDN is connected to GND. In the case of adiabatic logic (2PASCL and sub-Vt 2PC2AL), both PUN and PDN are connected to different V_{pc} and V_{pc}-, in which they require two extra power clock generator circuits to produce sinusoidal power clock supplies in the real circuit implementation.

The difference of the SBSAL circuit among adiabatic logic styles is that PDN in connected to 0.23 Volt bias voltage. Therefore, the SBSAL only needs one circuit to produce V_{pc} power supply. It means that, the overall circuit complexity has low cost compare to the other adiabatic logic family in this work. The input-output signals of each inverter logic style are shown on the bottom of each logic circuit schematic in Fig. 5.

b. Proposed SBSAL Operation

Propose SBASL circuit operation can be seen in Fig. 6. Obviously, this figure shows that the SBSAL circuit is basically operated in two phases as follows:

1) Charging Period: When the SBSAL circuit is in charging operation, the input signal transition from logic 1 to 0 occurs at 0 V level of power clock signal, which make no power loss at input data transition. Once the input signal stable at 0 V level, transistor P1 in Fig. 5(d) is fully ON and the output node is connected to V_{pc} signal. At this period, the supply current of I_{Vpc} slowly flows into output capacitance through PMOS (RP), as shown in Fig. 6(b). Although, there is some amplitude of current measured (18.31 µA) at input transition from 1-to-0, the energy consumed is significantly low because at this point V_{pc} is at approximately zero level as stated before.

2) Discharging Period: Equivalent circuit in discharge period is shown in Fig. 6(a). When the input data transition from 0-to-1, the output capacitance is discharged to V_{bias} level through NMOS (RN). It is similar as PUN operation that even though the current of I_{bias} flows (33 µA),

there is no energy loss because the output voltage maintain zero level same as V_{pc} trace.

Moreover, at previous state, the output voltage is higher that the V_{bias} voltage, hence the energy loss of V_{bias} power supply is compensated by V_{out} as formulated in following equation:

$$E_{SBSAL} = \frac{RC}{\tau} CV_{PC}{}^2 + \frac{1}{2} CV_{bias}{}^2 + \frac{RC}{\tau} C(V_{out} - V_{bias})^2 \quad (3)$$

This means, the energy stored in the load capacitance C_L is recycled to V_{bias} power supply.

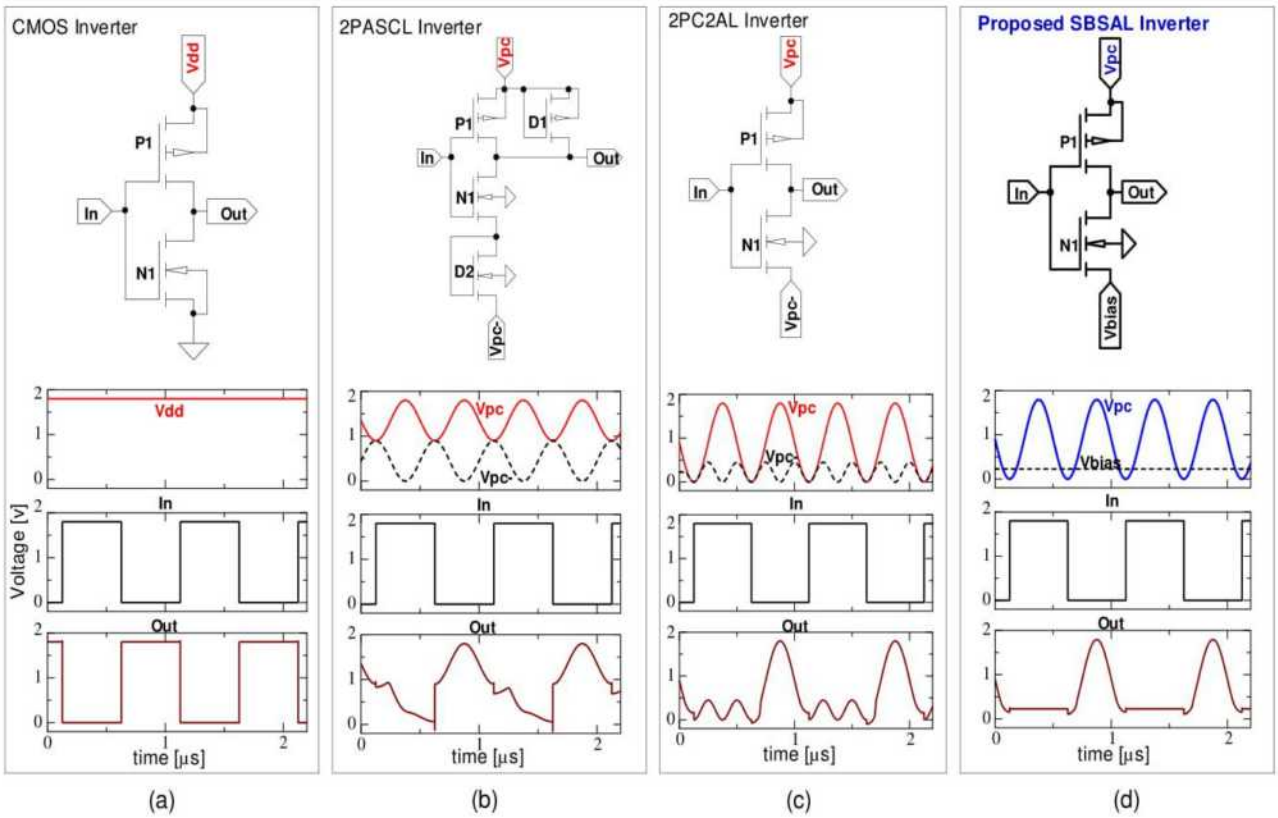

Fig. 5 Inverter logic investigated; a) Conventional CMOS logic, b) Adiabatic 2PASCL logic [4], c) Adiabatic 2PC2AL logic [5], and d) Proposed SBSAL.

4. 4 x 4-bit Array SBSAL Multiplier

The proposed SBSAL logic functional stability is validated by implementing it into an LSI 4 x 4-bit Array Multiplier, as shown in Fig. 7. The 4x4-bit array SBSAL multiplier consists of 16 ANDs, six full-adder logic circuits, and four half-adder logic circuits. In this work, we also conduct energy comparison of SBSAL Multiplier with other conventional static logic families, such as conventional CMOS logic, 2PASCL, and sub-Vt~2PC2AL shown in Fig. 5 by using the same multiplier circuit topology in Fig. 7.

5. Simulation Results

a. Simulation Condition

To evaluate the circuit functionality, stability and the energy consumed by SBSAL, we simulate inverter circuits, NAND/AND circuits, XNOR/XOR circuits, half-adder and full-adder circuits, and the multiplier circuits of each investigated logic using SPICE simulation

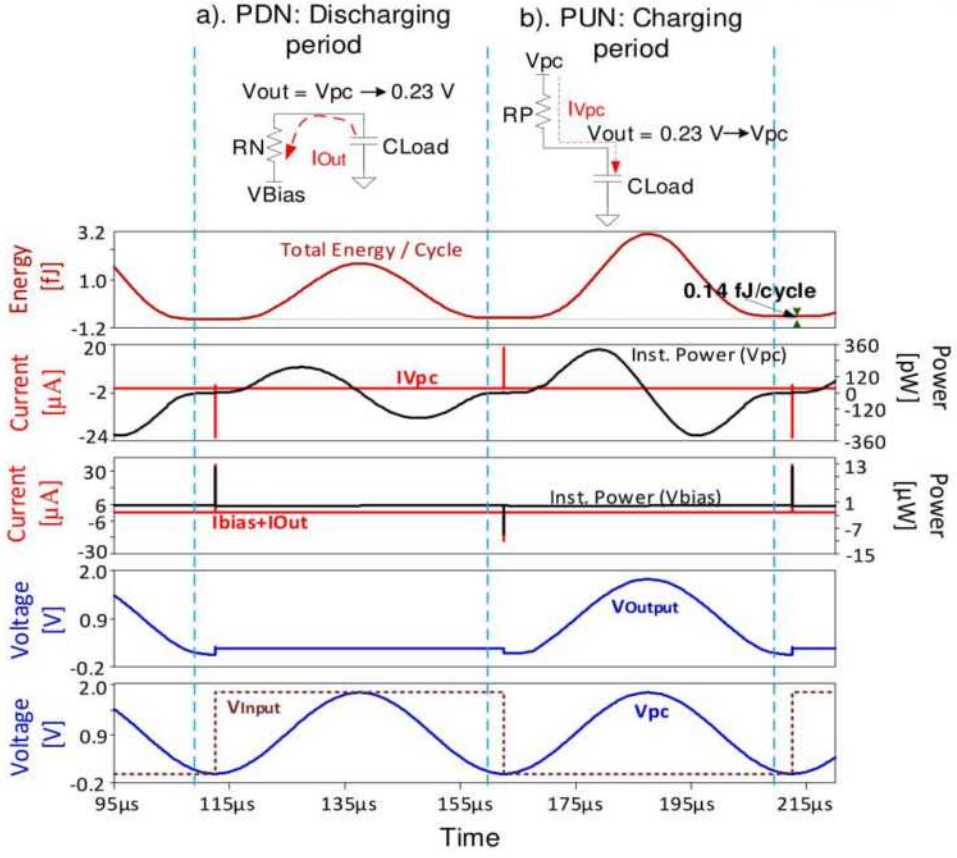

Fig. 6 Proposed SBSAL logic operation; a) Discharging period, b) Charging Period.

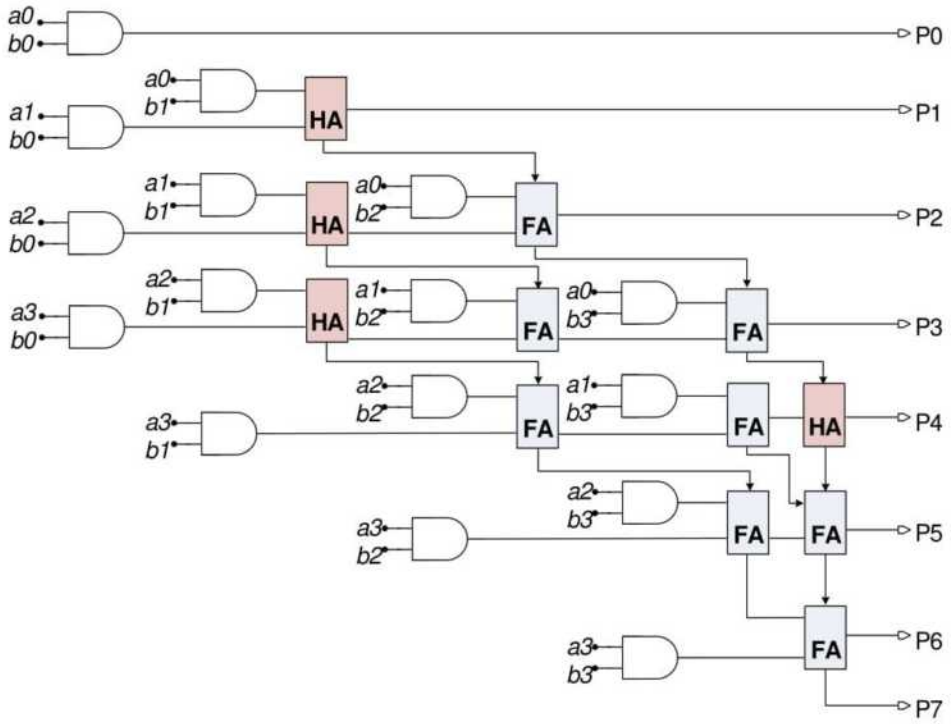

Fig. 7 Circuit diagram of a 4x4-bits array LSI multiplier.

with an 0.18 µm, 1.8~V CMOS standard process technology. The transistor size *W/L* is 0.6 µm/0.18 µm for both of PMOS and NMOS transistors. The voltage supply for conventional

CMOS is constant at 1.8~V, while the adiabatic logic families are supplied using sinusoidal power clock supply, where the supply voltage swing from 0 to 1.8 V. The 4x4-bits Array SBSAL LSI Multiplier is evaluated from frequency range of 10 KHz -100MHz.

Energy dissipated by each logic circuits are obtained from SPICE simulation using the following formula:

$$E_{diss.} = \int_0^T \left(V_{pc(t)} I_{pc(t)} + V_{bias} I_{bias(t)}\right) dt, \quad (4)$$

where T is the time period, V_{pc}, I_{pc}, V_{bias} and I_{bias} are source voltage and source current of the power clock signals and bias signal respectively.

b. Simulation Results

In this research, we first evaluate the energy dissipated by the proposed SBSAL circuit at the fundamental logic level. The comparison results in Fig. 8 shows that the proposed SBSAL has lower energy along the dynamic frequency ranges. The SBSAL inverter circuit reduced energy from the conventional CMOS logic about 99.76% at 1~MHz dynamic operating frequency.

To validate the effectiveness of the proposed logic as low-power SBSAL circuit, we implemented a 4x4-bits Array SBSAL LSI Multiplier. It is verified that the SBSAL multiplier logic function is well operated as shown in Fig. 8. Its energy is checked and compared with other adiabatic static logic families including conventional static CMOS logic as depicted in Fig. 9. As we may observe from this figure that the proposed SBSAL multiplier has reduced energy about 94% from conventional CMOS circuit, 84% from the 2PASCL circuit and 58% from the 2PCAL circuit at 1~MHz operating frequency.

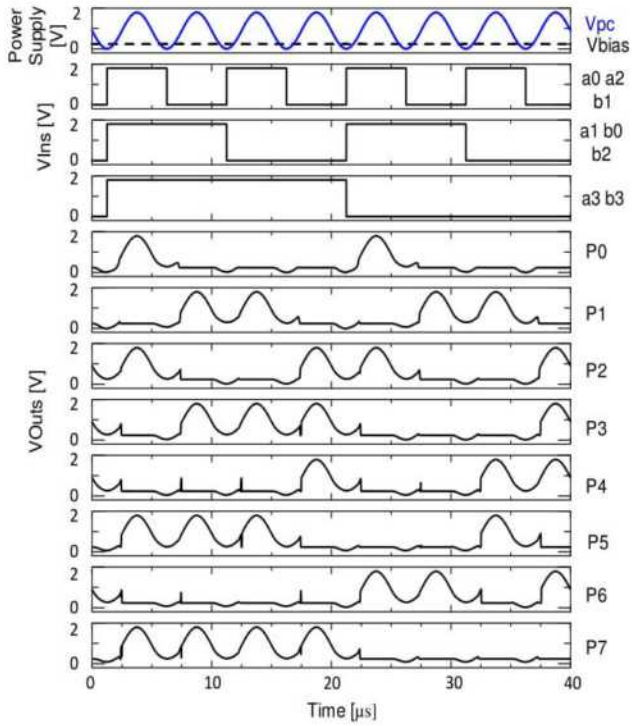

Fig. 8 Input-output signals of SBSAL Multiplier at 25 MHz.

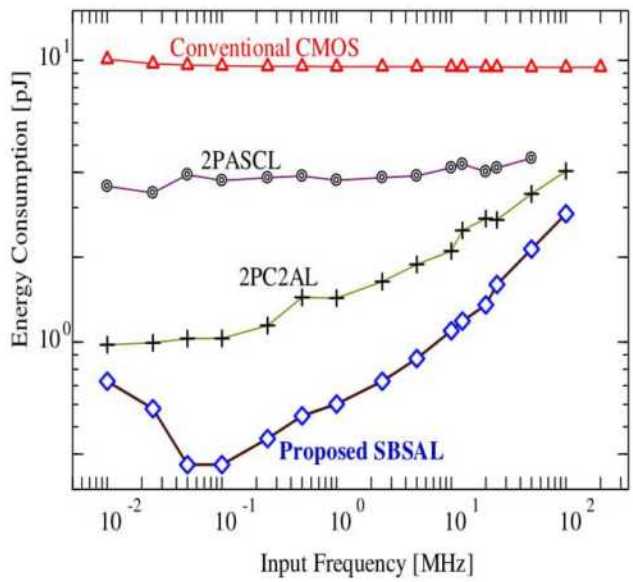

Fig. 9 Simulation results of energy dissipation of the LSI multiplier circuits.

6. LSI Chip Measurement Result

The LSI of 4x4-bits multiplier was designed by Kato et al. [5] in the Analog/Digital System LSI Laboratory of Gifu University, where the chip area is 193 x 123.7 μm^2. Using the same LSI chip, the author of this work conducted a measurement as shown in Fig. 11. The input-

output waveforms at 1 KHz dynamic frequency operation is shown in Fig. 12. It is important to notice that the waveforms in Fig.8 and Fig. 12 has different output traces, it happened because the input patterns adopted are different at simulation and measurement as we can observe the labels of each figure.

Measurement result of energy dissipation of the proposed SBSAL, conventional CMOS and semi-adiabatic CMOS logic are shown in Fig.13. Measurement was conducted with dynamic operating frequency from 1 KHz- 10 KHz, where the proposed SBSAL consume less energy at 5 KHz compare to others. It is obviously shown that energy dissipation of measurement result is severely higher than the one of simulation result. This normally happened because the measurement signals always included with internal and external noises, cable losses and more significant effect is the internal parasitic capacitances.

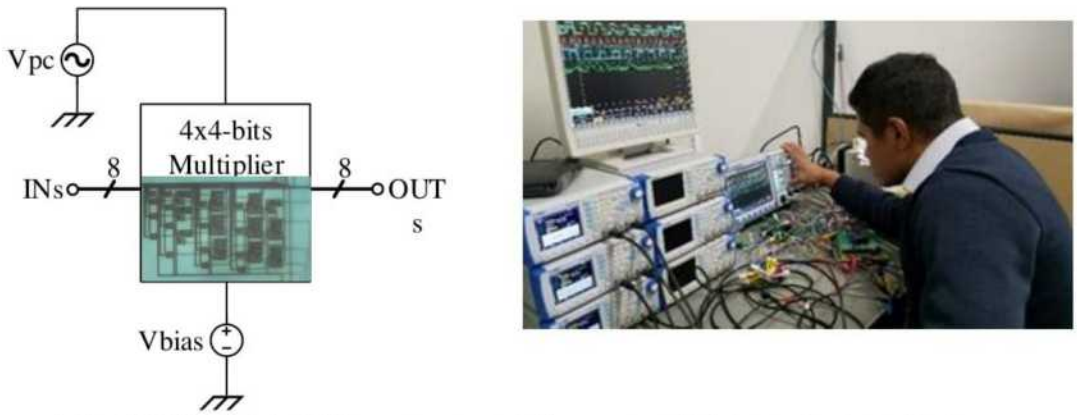

Fig. 10 Microchip LSI measurement diagram and chip under test photo.

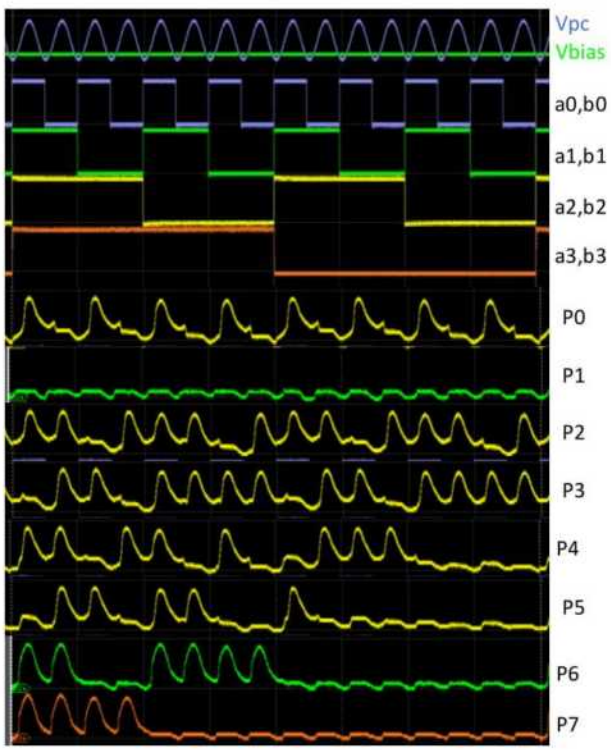

Fig. 11 Measurement result of input-output signals

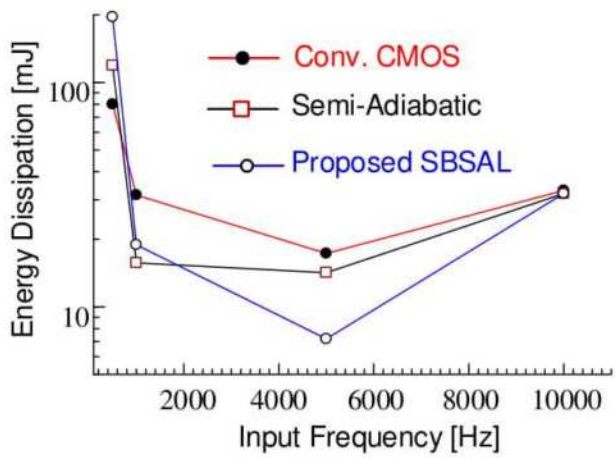

Fig. 13 Measurement result of energy dissipation at 1 KHz- 10 KHz.

7. Conclusion

We have presented the comparison study on energy dissipation of the proposed SBSAL with

other conventional circuit topologies at LTspice simulation and the LSI chip measurement. Simulation results have shown that the proposed SBSAL multiplier has reduced energy about 94% from conventional CMOS circuit, 84% from the 2PASCL circuit and 58% from the 2PCAL circuit at 1~MHz operating frequency. Moreover, the measurement results have also shown that the proposed SBSAL multiplier LSI chip consume less energy at 5 KHz than the others. It is noticeable that the measurement result of Energy dissipation is severely higher than the one of simulation result. This normally happen because the measurement signals always included with internal and external noises, cable losses and more significant effect is the internal parasitic capacitances.

Acknowledgement

The author would like to thank to Dr. Kato and the Analog/Digital System VLSI Laboratory of Gifu University (Sekine-Takhashi LAB) for providing the Multiplier LSI chip and all supporting equipment that made the SBSAL LSI measurement has become possible. Furthermore, the author also would like acknowledge the CADEFEST project for indirect financial support for this research activities.

Reference

[1] H. Jayakumar et al., "Powering the Internet of Things," in Proc. ACM/IEEE Int. Symp. Low Power Electron. Design, La Jolla, CA, USA, Aug. 2014, pp. 375-380.

[2] T. Wan, Y. Karimi, M. Stanacevic, and E. Salman, "Perspective Paper-Can AC Computing Be an Alternative for Wirelessly Powered IoT Devices?", IEEE EMBEDDED SYSTEMS LETTERS, VOL. 9, NO. 1, pp. 13-16, Mar. 2017.

[3] W.C. Athas, L.J. Svesson, J.G. Koller, N. Traztzanis, and E.Y.-C. Chuo, ``Low power digital system based on adiabatic-switching principles," in {\em IEEE Trans. Very Large-Scale Integration Syst.}, vol. 2, no. 4, pp. 398--406, Dec. 1994.

[4] N. A. Nayan, Y. Takahashi, T. Sekine, "LSI Implementation of a Low-Power 4×4-bit Array Two-Phase Clocked Adiabatic Static CMOS Logic Multiplier", Microelectronics Journal, Vol. 43, No. 4, pp. 244-249, April 2012.

[5] K. Kato, Y. Takahashi, T. Sekine, "Two Phase Clocked Subthreshold Adiabatic Logic", IEICE Electronic Express, Vol. 12, No. 20, pp. 1-12, Sep. 2015.

[6] J.S. Denker, “A Review of Adiabatic Computing," in Proc. IEEE Int. Symp. Low Power Electronics}, San Diego, CA, Oct. 10--12, 1994, pp. 94--97.

[7] Y. Moon, and D.K. Jeong, “An efficient charge recovery logic circuit," IEEE J. Solid-State Circuits., vol. 31, no. 4, pp. 514--522, April 1996.

[8] A. Vetuli, S.D. Pascoli, and L.M. Reyneri, “Positive feedback in adiabatic logic,” Electronics Lett., vol. 32, no. 20, pp. 1867-1869, Sept. 1996.

[9] D. Maksimovic, V.G. Oklobdvzija, B. Nikoli'c, and K.W. Current, “Clocked CMOS adiabatic logic with integrated single-phase power-clock supply,” IEEE Trans. VLSI Syst., vol. 8, no. 4 pp. 460 - 463, 1998.

[10] Y. Takahashi, K. Konta, K. Takahashi, M. Yokoyama, K. Shouno, and M. Mizunuma, "Carry propagation free adder/subtractor VLSI using adiabatic dynamic CMOS logic circuit technology," IEICE Trans. Fundamentals, vol. E86-A, no. 6, pp. 1437-1444, June 2003.

[11] Y. Takahashi, T. Sekine, and M. Yokoyama, "VLSI implementation of a 4x4-bit multiplier in a two-phase drive adiabatic dynamic CMOS logic," IEICE Trans. Electron., vol. E90-C, no. 10, pp. 2002 - 2006, Oct. 2007.

[12] Y. Takahashi, T. Sekine, and M. Yokoyama, "Two-phase clocked CMOS adiabatic logic," Far East J. Electronics and Communications, vol. 3, no. 1, pp. 17-34, April 2009.

[13] N.A. Nayan, Y. Takahashi, and T. Sekine, "Two phase clocked adiabatic static CMOS logic and its logic family," IEEK J. Semiconductor Tech. and Sci., vol. 10 no. 1, pp. 1-10, Mar. 2010.

[14] C. Monteiro, A. Maria, and Y. Takahashi, "Low power source biased semi-adiabatic logic circuit for IoT devices," *Proc. IEEE ISPACS 2018*, pp.43-47, Nov. 27-30, Okinawa, Japan.

Timorese Academic Journal of Science and Technology (TAJST)
Volume 2
September 2019

Additional Information (International: Journals and Conferences Proceeding)

The publication list in this page are all the latest articles (published in 2018 and 2019) Authored by the Faculty Staffs of FEST-UNTL in International Journals and Conference Proceedings.

Journal:

1. **Frederico Soares Cabral,** Hidekazu Fukai, Satoshi Tamura, *"Feature Extraction Methods Proposed for Speech Recognition Are Effective on Road Condition Monitoring Using Smartphone Inertial Sensors." Sensors* 19, no. 16:3481, 2019. (DOI:https://doi.org/10.3390/s19163481)
2. Ikuo TANABE, **Valerio de Sousa Gama,** Yoshifumi ISE, Hiromi ISOBE, Satoshi TAKAHASHI, *"Development of a high-speed mirror-like finish polishing technology for minute parts based on a linear motor",* Journal of Machine Engineering. 19. 71-85, 2019. (DOI: 10.5604/01.3001.0013.0454)

Conference Proceedings:

1. **Vosco Pereira,** S. Tamura, S. Hayamizu and H. Fukai, *"A Deep Learning-Based Approach for Road Pothole Detection in Timor Leste",* IEEE International Conference on Service Operations and Logistics, and Informatics (SOLI), pp. 279-284, Singapore, 2018. (DOI: 10.1109/SOLI.2018.8476795)
2. **Vosco Pereira,** S. Tamura, S. Hayamizu and H. Fukai, *"Classification of Paved and Unpaved Road Image Using Convolutional Neural Network for Road Condition Inspection System,"* 2018 5th International Conference on Advanced Informatics: Concept Theory and Applications (ICAICTA), pp.165-169, Krabi, 2018. (DOI: 10.1109/ICAICTA.2018.8541284)
3. **Frederico Soares Cabral,** Mateus Pinto, Fernão A. L. N. Mouzinho, Hidekazu Fukai, Satoshi Tamura, *"An Automatic Survey System for Paved and Unpaved Road Classification and Road Anomaly Detection using Smartphone Sensor"*, pp. 65-70, Singapore, 2018. (DOI: 10.1109/SOLI.2018.8476788)

Timorese Academic Journal of Science and Technology (TAJST)

Volume 2

September 2019

Hera-Dili,Timor-Leste.

Supported by Japan International Cooperation Agency (JICA)

CADEFEST Project Phase-II

Faculdade de Engenharia, Ciência e Tecnologia
Gabinete de Cooperação e Pesquisa
Avenida Hera Cristo Rei-Dili, Timor Leste
E-Mail: ucp.fect@untl.edu.tl
Website: http://fect.untl.edu.tl/CU-tp.html